SYNTHESIS AND CHARACTERIZATION OF METAL-LOADED CLAY-BASED MATERIALS FOR REACTIVE ADSORPTION APPLICATIONS

by

DANH NGUYEN-THANH

A dissertation submitted to the Graduate Faculty in Chemistry in partial fulfillment of the requirements for the degree of Doctor of Philosophy, The City University of New York

2006

ProQuest Information and Learning Company
300 North Zeeb Road
P.O. Box 1346
Ann Arbor, MI 48106-1346

This manuscript has been read and accepted for the

Graduate Faculty in Chemistry in satisfaction of the

dissertation requirement for the degree of Doctor of Philosophy.

Teresa J. Bandosz

Date

Chair of Examining Committee

Gerald W. Koeppl

Date

Executive Officer

Teresa J. Bandosz

David C. Locke

Maria C. Tamargo

Supervision Committee

THE CITY UNIVERSITY OF NEW YORK

Abstract

SYNTHESIS AND CHARACTERIZATION OF METAL-LOADED

CLAY-BASED MATERIALS FOR REACTIVE ADSORPTION APPLICATIONS

by

Danh Nguyen-Thanh

Adviser: Professor Teresa J. Bandosz

Clay-based adsorbents were first synthesized by exchanging a nonporous clay with iron, zinc, or copper cations. In the case of iron, while most hydrated cations were located in the clay gallery, oxocations were present both in the gallery and on the outer clay surface. In both cases, the fraction of iron available for surface reaction was limited, as the hydrated cations were unreachable in the gallery and oxocations formed large clusters.

The initial clay was then intercalated with alumina pillars which resulted in the presence of micropores in the gallery. The pillared clay was subsequently loaded with iron, zinc, or copper that entered the material's pores. Iron clogged the micropores, which

reduced its availability, while copper was the most widely spread metal in the material's pores.

Using organic surfactants, the clay was also intercalated with silica and the resulting porous clay heterostructures had a higher porosity and wider micropores than the pillared clays. Metal loading created some new mesoporosity, due to the deposition of silica on the clay surface as a consequence of cation-exchange. Carbon deposits resulting from the thermal degradation of the surfactants during the materials' preparation seem to hinder the metals' accessibility in these materials.

These clay materials then served as templates for the synthesis of carbons via carbonization of sucrose within the pore space followed by the template removal by acid treatment. The carbons were partial replicas of their inorganic matrices, with micropores of identical sizes. The carbons appeared ordered on a short-scale, as graphene layers were stacked in parallel and formed micropores. These stacks adopt a house-of-cards structure, resulting in mesoporous voids. Due to acid treatment, the metal content of these carbons was low, except in the case of iron present under acid-resistant forms.

Cation-exchanged clays were finally used as binders of a porous activated carbon, improving the mechanical properties of the carbon. While a slight decrease in porosity was observed due to mass dilution effect, migration of metal from the clay to the carbon's micropores took place. That combined effect of metal and porosity gives potentially efficient adsorbents and catalysts.

Acknowledments

I would particularly like to express my deep gratitude to the following persons who made this work possible:

Prof. Gerald W. Koeppl who accepted me in the Chemistry Ph.D. program of the Graduate Center of the City University of New York.

Prof. Henri L. Rosano, Dr. François Gandolfo, and Dr. Mouhcine Kanouni from the City College of New York who helped me coming to New York and settling there.

Prof. Teresa J. Bandosz from the City College of New York for accepting me in her research lab, giving me the opportunity to study fascinating materials, improving my lab skills, sharpening my writing, strengthening my thinking, and overall making a better scientist of out me.

Prof. Maria C. Tamargo from the City College of New York who agreed to be a member of my Thesis Committee, allowed me to use her XRD device, and originally accepted me in her research group.

Prof. David C. Locke from Queens College for accepting to be a member of my Thesis Committee and for being supportive of my work since the beginning.

Dr. Jorge Morales from the City College of New York who patiently helped me with TEM analysis.

Prof. Bonnie L. Gersten and Dr. Baohe Chang from Queens College for some SEM analysis.

Dr. Karin Block from the City College of New York who helped me in some XRD measurements and analysis, and has since then become a close friend of mine, giving me precious pieces of advice for the writing of this dissertation.

Dr. Andrey Bagreev of my lab for showing me how to perform XRF analysis and for occasional fruitful scientific discussions.

Dr. Svetlana Bashkova of my lab who helped a lot in the lab when I got started there and who has always been kind to me despite my swinging moods.

Dr. Yehya El-Sayed of my lab who taught me how to use the FT-IR instrument and who kept encouraging me to finish my dissertation.

Dr. Conchi O. Ania of my lab who did some SEM analysis for me and who showed me how to carbonize materials.

Ms. Anna Kleyman of my lab who taught how to use most of the instruments in the lab and who has always been here whenever I needed technical assistance.

Ms. Hong Lu from the City College of New York to whom I owe most of my XRD measurements and who happens to be one of my best friends.

The Department of Chemistry at the City College of New York, and more particularly Prof. Stanley Radel and Prof. Simon A. Simms, for its financial support throughout the completion of my degree.

Table of Contents

List of Tables

List of Figures

1. INTRODUCTION

1.1. Adsorption

1.1.1. Fundamentals of Adsorption

Adsorption is a phenomenon in which molecules of a fluid called adsorbate accumulate on the surface of a substrate called adsorbent. It then differs from absorption, which is instead a volume and bulk process.

Adsorption can happen through two distinct mechanisms. The nature of the attraction between a surface and an adsorbate can be due to van der Waals forces that are intermolecular. These forces, usually found in liquids, include electrostatic interactions between the dipoles (permanent or instantaneous) of the molecules and hydrogen bonding [1]. In that case the attraction is purely physical as no chemical change occurs in the involved molecules: this is the process of physical adsorption or physisorption [2, 3]. But adsorption can also be the result of the formation and cleavage of chemical bonds as the adsorbate molecules interact with the free valencies present from the surface atoms of the adsorbent. Such a process is called chemical adsorption or chemisorption [2, 3]. Adsorption is generally an exothermic process. While the heat of adsorption ($-\Delta H$) for physisorption is in the 10-40 kJ mol^{-1} range, it is situated between 40 and 800 kJ mol^{-1} for chemisorption. Another major difference between the two processes lies in the number of adsorbate layers: if only one layer can form with chemisorption, several ones are possible with physisorption. Chemisorption is actually a chemical reaction between adsorbate

molecules and the surface atoms of an adsorbent. This process is then highly dependent on the nature of the adsorbent surface. On the other hand, at an advanced stage when surface coverage is more important, physisorption is considered as a condensation or liquefaction phenomenon, which explains why there is no activation energy for physisorption; by contrast, chemisorption does require some activation energy, even though small. Thus, in physisorption, surface specificities play a lesser role than adsorbate properties. Physisorption usually takes place at the boiling point of the adsorbate at the considered pressure.

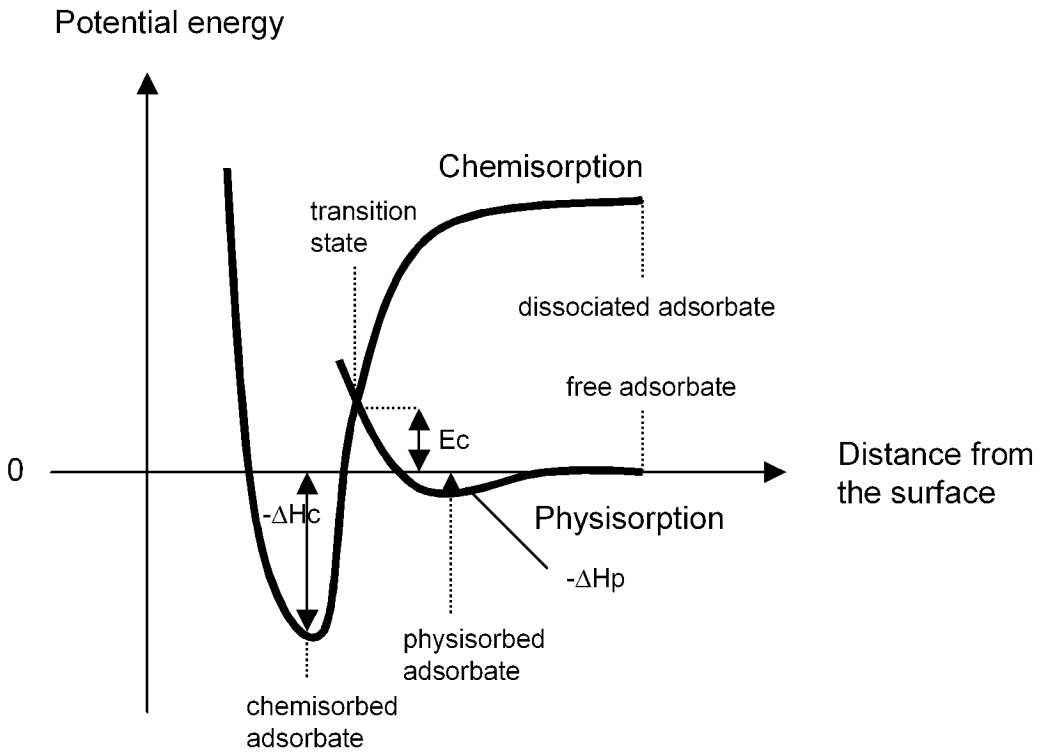

Figure 1: Potential energy curves for adsorption

Figure 1 illustrates the evolution of the potential energy of the adsorbate with the distance from the adsorbent's surface for physisorption and chemisorption. The zero of potential energy corresponds to the situation when the adsorbate is far from the surface. In chemisorption, the adsorbate gets closer to the adsorbent's surface than in physisorption. The transition state of chemisorption is the point where the physisorption and chemisorption curves intersect, and Ec is the activation energy for chemisorption. Chemisorption then starts as physisorption, so that the adsorbate can approach the surface with minimum energy. Once the transition state is reached, the process becomes chemisorption.

1.1.2. Quantitative Aspects of Adsorption: Isotherms

When adsorption reaches equilibrium, the quantity of adsorbed gas is a function of the adsorbate pressure and nature, the temperature, and the adsorbent nature and surface area. An adsorption isotherm is a plot of the quantity adsorbed (in for instance $cm^3\ g^{-1}$) vs. the relative pressure (P/Po) at a certain temperature. Gas adsorption is frequently used to assess the porosity of a material. Pores in a material have been divided into three size categories by the IUPAC [4]: the micropores (less than 20 Å), the mesopores (between 20 and 500 Å) and the macropores (more than 500 Å). Because of its small size (3.6 Å), which allows it to penetrate inside even the smallest pores and its lack of chemical reactivity, N_2 is the most used gas for the characterization of a material's porosity. Experimentally, six types of adsorption isotherms have been determined to exist, and they have been classified by the IUPAC [4], each one being characteristic of a

certain type of porosity. But adsorption isotherms can give more information than just porosity types based on their shapes. Indeed, equations modeling adsorption isotherms have been empirically and theoretically derived. From these models, structural properties such as surface areas, pore volumes, or pore size distributions, can be deduced.

The method that is the most widely used to assess surface areas is the BET (Brunauer-Emmett-Teller) model [2, 3]. That model considers a dynamic equilibrium between the adsorbing molecule and a surface site on the one hand, and the adsorption complex on the other hand, with several layers of adsorbate formed. Equating the rate of adsorption to the rate of desorption, the BET adsorption isotherm is derived [2, 3]:

$$P/V_a(P_o-P)=1/V_mC+(C-1/V_mC)(P/Po) \quad \textbf{(1)}$$

where V_a is the volume of N_2 adsorbed ($cm^3\ g^{-1}$), V_m is the volume equivalent to an adsorbed monolayer of N_2, and C is a constant. The expression of C is [2, 3]:

$$C=exp(H_1-H_L/RT) \quad \textbf{(2)}$$

where H_1 is the heat of adsorption of N_2 on the surface in the first layer (kJ mol^{-1}), H_L is the heat of adsorption of the second and subsequent N_2 layers and is equal to the heat of liquefaction of N_2 (kJ mol^{-1}), R is the universal gas constant (8.314 J K^{-1} mol^{-1}), and T is the absolute temperature (K). When P/P_o is comprised between 0.05 and 0.35, the plot of equation (1) is usually linear, and the slope and the intercept of that plot give V_m and C. From V_m, the number of molecules of N_2 in the monolayer is determined. The area of a

single N_2 molecule being of 16.2 * 10^{-20} m^2 [3], the surface area S_{BET} can then be calculated.

The total pore volume V_t of a material usually corresponds to the quantity adsorbed V_a when P/Po ~ 0.99.

Several methods for the determination of micropore volumes exist, such as the t-plot [5] and the α-plot [6]. These models postulate that adsorption in micropores happens by a layer-by-layer film formation on the micropore walls. Another and probably more realistic approach is the one by Dubinin-Polanyi termed micropore volume filling theory. It is from this theory that the Dubinin-Radushkevich formalism for micropore volume determination [8, 9] was developed. It defined the relative adsorption as:

$$\theta = V/Vo = exp[-(A/E)^2] \quad \textbf{(3)}$$

where V is the amount adsorbed in the micropores (cm^3 g^{-1}), Vo is the maximum micropore adsorption capacity (cm^3 g^{-1}), A is the adsorption potential (kJ mol^{-1}), and E is the characteristic energy for the adsorbate-adsorbent system (kJ mol^{-1}). A is related to the free energy of adsorption G through:

$$A = RTln(Po/P) = -\Delta G \quad \textbf{(4)}$$

Combining equations (3) and (4), the Dubinin-Radushkevich equation is obtained:

$$\theta = V/Vo = exp[-B(T/\beta)^2 log^2(Po/P)] \quad \textbf{(5)}$$

where B is a structural parameter that increases with pore size and β is a similarity coefficient with β = 1 for benzene. The Dubinin-Radushkevich equation is actually a particular case of the more general Dubinin-Astakhov equation with n = 2:

$$\theta = V/Vo = exp[-(A/E)^n] \quad \textbf{(6)}$$

n expresses the degree of heterogeneity of the microporous system. By applying log on both sides of equation (5), one has:

$$logV = logVo - (2.303R^2T^2/E^2)log^2(Po/P) \quad \textbf{(7)}$$

A linear plot of log V vs. $\log^2(P_o/P)$ thus allows the determination of Vo and E from the intercept and the slope. The Dubinin-Radushkevich equation is normally applied to materials whose pore size distribution in the micropore region is homogeneous or nearly homogeneous.

The determination of pore size distributions (PSDs) is subject to even more theories and controversies. When pores larger than 20 Å are considered, models based on the Kelvin equation are used [8], such as the Barrett-Joyner-Halenda (BJH) method [9], which is particularly popular. The Kelvin equation correlates the size of a pore to the pressure at which condensation in that pore takes place [10]:

$$ln(P/Po) = (\gamma V_L/RT)(r_1^{-1} + r_2^{-1}) \quad \textbf{(8)}$$

where γ is the surface tension of liquid N_2 (N m^{-1}), V_L is the molar volume of liquid N_2 (m^3 mol^{-1}) , R is the perfect gas constant, T is the temperature (K), and r_1 and r_2 are the liquid interface radii of curvature (m). To correct for the thickness t of the adsorbed layer at the point of condensation, a model thickness curve is also employed, such as the one from Halsey [11]:

$$t=-0.35[5/\ln(P/Po)]^{1/3} \quad \textbf{(9)}$$

But methods based on the Kelvin equation are inappropriate when dealing with microporous systems [12] and may even underestimate the sizes of smaller mesopores [13]. In that case, many models exist with the Horvath-Kawazoe [10] one being particularly used with pillared clays [12, 14, 15]. During the 1990s, the density functional theory (DFT), a method that originates from statistical thermodynamics, has proven to be a powerful method for the investigation of inhomogeneous fluids. Indeed, so far, adsorption isotherms considered the adsorbate as a homogeneous phase, whereas it is heterogeneous due to the higher density of adsorbate near the surface of the adsorbent [10]. The system being considered in the DFT is a single pore with two parallel walls separated by a distance H (slit-shaped) immersed in a single component adsorptive fluid. The grand potential functional Ω of that system is a function of the average singlet density profile ρ [10, 16]:

$$\Omega[\rho(r)]=F[\rho(r)]+\int dr\rho(r)[V_{ext}(r)-\mu_b] \quad \textbf{(10)}$$

where is r is the generalized coordinate vector, F is the intrinsic Helmholtz free energy functional, V_{ext} is the external potential, and μ_b is the bulk chemical potential imposed on the system. The equilibrium density profile corresponds to the value of ρ at which Ω is a minimum, that is, when the derivative of Ω with respect to ρ equals zero. F consists of (as an approximation) two contributions, one being the short-range hard-sphere repulsive forces and the other being the long-range attractive forces modeled by the Lennard-Jones potential [10, 16]. V_{ext} is composed of a particle-wall potential and an interparticle potential, both being modeled by the Lennard-Jones potential, with graphite carbon as the adsorbent for modeling the former.

The minimization principle leads to an equation that can be numerically solved for ρ. If two solutions exist for ρ, the stable state corresponds to ρ giving the lower grand potential. An equilibrium density profile can thus be determined for any equilibrium pressure. Integration of an equilibrium density profile from wall to wall and substraction of the quantity of adsorptive that would be present in the absence of wall forces give the quantity adsorbed at the considered pressure, a value that is normalized to one m^2 of wall area and expressed as cm^3 STP (Standard Temperature and Pressure) for comparison with experimental data. Assuming that each pore acts independently, each pore size contributes to the total adsorption isotherm in proportion to the fraction of the total area of the sample, which is expressed as [10, 16]:

$$Q(P)=\int f(H)q(P, H)dH \qquad \textbf{(11)}$$

where P is the pressure, Q is the experimental quantity adsorbed, f is the pore surface area distribution, and q is the quantity adsorbed in an ideal pore of size H. q is thus the kernel

function describing the adsorption isotherm. That equation is solved for f(H) with the help of a computer in a discrete form by replacing the integral by a summation. Once f(H) is found, the PSD in terms of incremental pore volume vs. pore width can be determined.

In the case of alumina or silica materials, DFT cannot be applied as it is, since its reference substrate is graphite carbon. If the material is rather microporous, a modified DFT can be applied following the method suggested by Tarazona [17, 18]. The pore geometry would then be cylindrical and a wall potential typical of alumina or silica surfaces would be used [16]. For mesoporous materials, a hybrid DFT would be chosen [16] with a kernel function q deduced from experimental adsorption isotherms of well-characterized materials such as MCM-41, silicas, and zeolites [10, 16, 19, 20].

1.2. Adsorbents

1.2.1. Roles and Uses of Adsorbents

With a greater awareness of problems related to pollution and always-stricter environmental regulations, new means to improve the quality of the environment need to be developed. Pollution affects the air, water, and soil, and can be of natural (like erupting volcanoes or decomposing organic matter from plants and animals) or man-made origin (such as industrial and domestic waste, use of fertilizers, or combustion of fossil fuels). Besides degrading the environment, pollution causes a human health problem and it is an economic issue with the damaging (corrosion, erosion) of

infrastructures. Pollution usually involves chemical species and it is then up to the chemist to find solutions to this problem.

An efficient way to remedy chemical pollution, in gas or liquid phase, is to use adsorbents, whether the pollutant is organic or inorganic. Adsorbents are generally porous materials, so that pollutants can be adsorbed inside their porous system.

1.2.2. Carbonaceous Adsorbents

Adsorbents can be of diverse origin, but activated carbons are the most widely used materials [21, 22], due to their efficiency in adsorption processes, their low cost, and their ease of regeneration. Activated carbons are applied in purification and filtration technology, both in the gas and liquid phase. They are manufactured from organic materials such as wood, peat, coconut shells, or bitumous coal. Pyrolysis of those materials under an inert atmosphere (like N_2) gives a raw carbonaceous residue that, after activation, yields a highly porous carbon [23]. Activation is accomplished either by treatment of the carbonaceous material with an oxidizing gas (like steam, air, or CO_2) or by mixing the carbon precursor with a chemical agent (like $ZnCl_2$ or H_3PO_4) prior to pyrolysis [24].

Activated carbons are amorphous materials that consist of graphene layers. These layers are flat and polyaromatic, with carbon and hydrogen as the main atoms and oxygen and nitrogen as the most common heteroatoms [25]. The graphene layers are generally terminated on the edges by hydrogen atoms, but some functional groups (like carboxylic, lactonic, or phenolic [26]) can occasionally be present. Graphenes are arranged by the

parallel stacking of a few layers separated by distances that are of nanoscale dimensions. These gaps between layers, that are thus slit-shaped, are responsible for the high porosity of activated carbons and are mostly micropores. The graphene layers do not exhibit any long-range order [27], and larger pores, mesopores and macropores, can thus exist between stacks of graphene.

In solution, activated carbons are often used for adsorption of metal cations, especially the heavy ones like Hg^{2+} and Pb^{2+} [28]. Activated carbons are thus particularly attractive materials for the treatment of wastewaters. For carbons with acidic oxygen functional groups, adsorption appears to occur through an ion-exchange mechanism between cations from solution and protons from acidic groups [28, 29]. Basic functional groups, particularly the ones containing nitrogen, have also been recognized to have an affinity towards metal cations [29, 30]. It is then believed that functional groups like the pyridinic structure adsorb metal cations by acting as coordination sites [30]. In another study [31], the amine group exhibited a strong affinity for Cu^{2+}, with a saturation loading capacity of 0.86 mmol/g, the equilibrium adsorption being reached in less than a minute.

Activated carbons can also be used as adsorbents in the gas phase, thus representing a way to obtain cleaner air, as for example around water-treatment plants. The Bandosz group has shown the capacity of some wood-based carbons [32, 33] to retain H_2S from moist air at room temperature. Adsorption of H_2S on those carbons actually happens by chemisorption, and not just physisorption: H_2S first dissociates in a water film on the carbon surface into HS^- which then becomes oxidized to sulfur radicals. The presence of pores smaller than 10 Å on these carbons turned out to be a determining factor, as such small pores allow the formation of a water film even at a relatively low

humidity. The authors pointed out though that for the adsorption of H_2S, pores should be larger than 5 Å so that they can contain functional groups that can favor the deposition of water on the pore walls. In these studies, products from the oxidation of H_2S gradually filled the carbon pores. Those deposits, especially in micropores, can limit the regenerative properties of the carbon adsorbent, as a study from the same group has demonstrated [34].

Like functional groups, metal oxide phases, preferably well dispersed, can play a crucial role in the adsorption of H_2S on carbons. This is illustrated by the work of the Bandosz group on carbonaceous adsorbents derived from sewage sludge [35, 36], where oxides of iron, copper, and zinc were believed to allow H_2S fixation. When $ZnCl_2$ was used to activate the sludge materials [35], H_2S is adsorbed in the form of sulfides, sulfates, or sulfuric acid, depending on the adsorbent's pretreatment conditions.

During the 1990s [37, 38], highly porous carbons have also been obtained through template synthesis. In that method, the pores of a mesoporous inorganic template are filled with a carbon precursor (such as sucrose, furfuryl alcohol, or phenolic resin [39]), and the obtained material is then carbonized under an inert atmosphere between 600 and 1,200 ^{o}C [25, 39, 40]. During carbonization, carbon forms inside the pores of the inorganic material. The inorganic phase is then removed, and a carbon material, whose porous structure is the negative replica of the inorganic template, remains. Unlike conventional activated carbons, carbon materials synthesized in this way are not microporous, but mesoporous like their inorganic templates. Those larger pores render templated carbons particularly attractive for the adsorption of large organic pollutants, such as phenol derivatives [41].

A variety of inorganic templates have so far been used for the synthesis of such carbon materials. Ryoo *et al.* [39] were the first group to synthesize a highly ordered carbon through this technique, using the mesoporous silica MCM-48 (that is like MCM-41 part of the M41S family and will be described in more details in the next section) as template. Sucrose was their carbon precursor and they removed the silica template with an aqueous solution of NaOH and ethanol. Their mesoporous carbon exhibited a uniform pore size distribution with a peak at 30 Å. But while that carbon seemingly retained the crystal morphology of its template, it did not turn out to be the exact negative replica of its model, as the two materials differed in pore sizes, the carbon pores being larger. This structural mismatch was attributed to the strain exerted by the silica template on the carbon phase that was relieved after the template removal. Overall, their carbon, despite some atomic disorder, proved to be highly porous with a mesopore volume of 1.1 $cm^3 g^{-1}$ and a surface area of 1380 $m^2 g^{-1}$. It also apparently possessed micropores that formed during pyrolysis along with oxygen and hydrogen atoms that render the grafting of oxygenated functional groups within the carbon pores possible.

In another study [25], a sodium-rich natural montmorillonite served as the template, with sucrose as the source of carbon. A mixture of HF and HCl dissolved the inorganic substrate. The carbon had a surface area of 1290 $m^2 g^{-1}$ and a pore volume of 1.48 $cm^3 g^{-1}$. Its pore size distribution showed a single peak at 26 Å. On a short scale, the material consists of graphene sheets of various sizes and shapes stacked in a parallel fashion. Nevertheless, that carbon material showed no long-range order, with stacks of graphene layers assembled in a house-of-cards structure. Actually, it seems that this material contains two carbon phases, one that is amorphous and dense, and another that

adopts a layer structure: while the former would form on the outer clay surface, the latter would be the result of the clay template effect.

Trying out different zeolites (as templates) and carbon precursors [40], Meyers *et al.* obtained carbons with surface areas as high as 947 m^2 g^{-1}. Several wash cycles with pure and diluted HF and HCl were carried out for demineralization. The carbons contained oxygen as the most common impurity, which resulted in the presence of alcohol surface groups. But similarly as in the previous examples, these carbons proved to be disordered.

1.2.3. Inorganic Adsorbents

Adsorbents can also be of inorganic origin. For example, a very common adsorbent for the removal of arsenic from drinking water is activated alumina. Indeed, for such kind of processes, adsorption is considered as less expensive and safer to handle than precipitation, ion exchange, or membrane filtration. Actually, a study [42] showed that a synthesized mesoporous alumina gave better adsorption capacities and kinetics of adsorption for arsenic than regular activated aluminas. The better overall performance of the mesoporous alumina was attributed to its large surface area, its uniform pore size, and its interlinked pore system. Furthermore, the mesoporous alumina proved to be easily regenerated by diluted NaOH.

Zeolite adsorbents have been shown to be rather effective in the desulfurization of liquid fuels [43, 44]. Zeolites [45] were among the first synthesized so-called molecular sieves. They are microporous aluminosilicate materials with a uniform channeled

structure. They consist mainly of silicon, with some substitutions of Si^{4+} by Al^{3+}. These substitutions entail the presence of negative charges that are compensated by cations such as H^+ or Na^+. For the desulfurization of liquid fuels, it seems that the identity of the cation loaded in the zeolite and its degree of dispersion determine the degree of sulfur compound removal, with Ni^{2+} and Cu^+ demonstrating superior performances. In the industry, zeolites are mainly used in air separation processes [46], which are actually kinetic separations based on the difference in diffusion rates between gases into the adsorbent [47].

Adsorption of a molecule on an adsorbent's surface can happen through different kinds of intermolecular interactions. In that regard, Guan *et al.* [48] studied the adsorption of dibenzodioxin on silicas, metal oxides, and zeolites. Results from thermal analysis and FT-IR tended to indicate that the strength of the bond adsorbate-adsorbent surface increases in the order silicas, metal oxides, and zeolites. They finally proposed that dibenzodioxin adsorbs on the silicas, metal oxides, and zeolites through respectively hydrogen bonding, complexation with Lewis acid surface sites, and attraction from pore walls.

To obtain better adsorptive properties, catalytic species are sometimes added to inorganic materials. Iretskaya and Mitchell's work [49] is an example of that approach: they loaded an alumina with copper oxide to adsorb SO_2 from a He/O_2 gas stream. That adsorbent was treated with various halides and alkali metals and it turned out that chloride has a promoting effect in the adsorption process, giving improved capacities and rates of adsorption. The authors suggested that chloride favors the wetting of the alumina surface by the copper species present on it.

During the 1990s, a new class of mesoporous inorganic materials, named M41S, has been discovered [50]. These materials possess an ordered structure with pores consisting of uniform channels. The pore sizes are tunable and usually fall between 15 and 25 Å, the so-called supermicropore-small mesopore range [51]. Modifying MCM-41, a member of the M41S family consisting of hexagonal arrays of channeled mesopores, with an amine, Sayari *et al.* [52] employed two materials, one with amine in its pores for the adsorption of metal cations, and another one made only of silica for the adsorption of organic pollutants, both processes happening in solution. Inorganic adsorbents for heavy metal cations have been developed partly as an alternative to activated carbons, as the latter materials usually exhibit limited loading capacities [52] and relatively weak interactions with metal cations [53, 54].

In the industry, pillared clays, which are microporous aluminosilicate materials, have been proposed as alternatives to activated carbons and zeolites in air separation processes that proceed though kinetic separation [46, 47]. Cheng and Yang loaded alumina and zirconia pillared clays with different alkali metal cations [46] to assess the influence of the pillaring species and of the identity of the alkali on the air separation of O_2 and N_2. They found that zirconia pillared clays exhibited higher adsorption capacities as they had pore sizes smaller and thus closer to the adsorbate molecular dimensions. Among the alkali metals, lithium demonstrated a clear superiority, which was attributed to its small ionic radius, as that property grants lithium with greater polarizing effect toward the quadrupolar N_2 and avoids pore blocking. Nevertheless, that study is one of the few examples in which pillared clays are used as adsorbents. Indeed, pillared clays

usually play the role of solid acid catalysts in cracking or other organic reactions [15, 55], just like M41S materials [56].

1.3. Clay-based Porous Materials

1.3.1. Clay Minerals

Clay minerals are hydrous aluminosilicates that form crystallites the size of colloidal particles, usually under 2 μm. They are naturally occurring and are major components of soils and sedimentary rocks.

Clays are layer-structured materials with platelets consisting of tetrahedral and octahedral sheets. In tetrahedral sheets, Si^{4+} is the dominant cation, while in the octahedral ones, it can be Al^{3+}, Mg^{2+}, Fe^{2+}, or Fe^{3+}. The ratio of number tetrahedral sheets:number of octahedral sheets is either 1:1 or 2:1, and determines the layer type of the clay. Substitution of some cations in a sheet by other cations with a smaller charge is responsible for the presence of a negative charge in clay layers. The magnitude of this charge allows separating clays with the same layer type into groups.

One of the most interesting and thus studied groups of clay is the smectite one that has a 2:1 layer type and a charge of 0.2-0.6. Montmorillonite is a clay species that belongs to the smectite group, and it has been the starting material of many studies by chemists for different purposes. In montmorillonites, Al^{3+} is the major cation in octahedral sheets. The most frequent substitutions in montmorillonite layers are Mg^{2+} for Al^{3+} in octahedral sheets and to a much lesser extent Al^{3+} for Si^{4+} in tetrahedral sheets.

This results into negatively charged layers of around 0.33, the charge deficit being mainly located in the octahedral sheets [46]. The electroneutrality of montmorillonite is insured by the presence of charge-compensating cations, such as Na^+, K^+, Ca^{2+}, or Mg^{2+}, present in the interlayer space. These cations can be exchanged with other ones if montmorillonite is dispersed in a cation-containing solution. Montmorillonite clays are then characterized by a chemical formula and a cation-exchange capacity (CEC), usually expressed in meq or mmol of cations per g of clay. The CEC is usually around 1.00 mmol/g [57]. The thickness of a montmorillonite layer is of 9.6 Å [58, 59].

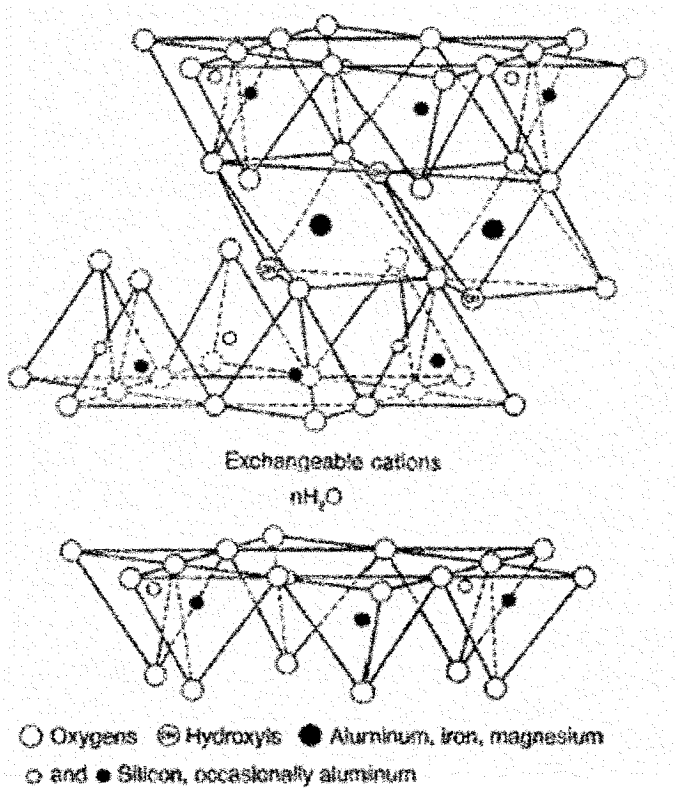

Figure 2: Structure of smectite clay [60]

The charge-compensating cations also give montmorillonite, and smectite clays in general, the ability to swell when in contact with water: water can penetrate into the

interlayer space and bring the layers apart with the crystallographic structure of the latter ones being preserved; water molecules form a coordination sphere around the cations in the interlayer space [58]. Smectite clays are thus hydrophilic. Montmorillonite contains between zero and three layers of water molecule, each one being 2.8 Å thick [58].

Beside obvious applications in the ceramic industry or in construction practices, clays have many chemical applications, for example in the removal of toxic and radioactive wastes [61] or as catalysts and molecular sieves [62]. Nevertheless, except in the very beginning, clays are rarely used as-they-are, and they generally need to be modified before being applied for a specific purpose. Many ways of clay modification exist, and they all involve intercalation of chemical species between the layers.

1.3.2. Pillared Interlayered Clays (PILCs)

Pillaring is the most common way of clay modification. This method grants clays with acidity (of Brönsted and Lewis types) and porosity. These properties explain why pillared interlayered clays (PILCs) are mostly used in heterogeneous catalysis [15, 55], even though a few studies of PILCs as gas adsorbents have been carried out [46, 47].

Originally, clays possess a very low porosity and their pores are mainly large mesopores and macropores. Montmorillonite typically has a surface area of 20-30 m^2/g [55, 57, 63], a pore volume of 0.040 cm^3/g [8, 55, 57], and a microporous volume of 0.000-0.010 cm^3/g [8, 55, 57].

Clay pillaring is based on exchanging the interlayer cations consisting of a single atom with large cations containing several atoms. This results in an increase in the

distance between clay layers and in the generation of micropores in the clay gallery, between the newly intercalated cations. Originally, clays were intercalated with organic cations [64], but such materials were not thermally stable [15]. That is why chemists have been working with inorganic pillars since the late 1970s [65-67].

Inorganic pillaring occurs in two steps. At first, large metal polyoxocations are intercalated through cation-exchange in the interlayer space; metal polyoxocations are generally obtained by the base hydrolysis of a metal salt [12], for example $AlCl_3$ with NaOH [15]. The clay is then calcined to at least 400 ^{0}C [57,63]. As a consequence, chemically stable metal oxide pillars separate the clay layers. But if in some smectites (such as saponite) a chemical reaction binding the clay layers to the pillars occurs, it is not the case with montmorillonite [12, 68]. The most frequently encountered pillars in the literature are oxides of aluminum [69, 70], zirconium [47, 70], chromium [70], titanium [70, 71], and iron [70, 72]. The micropores in the clay gallery space are thus delimited vertically by the layers (interlayer distance) and horizontally by the pillars (interpillar distance) [12, 70]. It is quite controversial as to what exactly the pore size represents in PILCs, either the interlayer distance or the interpillar spacing; but it seems though that it is the latter that is indeed the pore size [73, 74]. That size is comprised between 4 and 20 Å, depending on the type of the pillars [13].

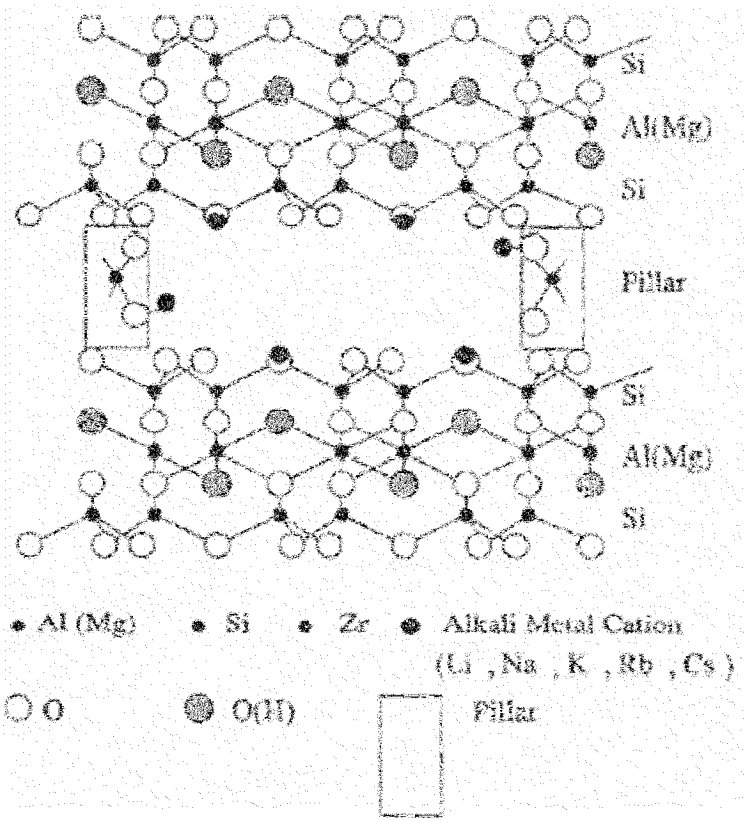

Figure 3: Structure of PILC with alkali charge-compensating cations [46]

Due to their microporosity, PILCs are considered as shape-selective materials or molecular sieves just like zeolites [58, 64], but with wider pores [75] accessible to larger molecules. PILCs furthermore offer the advantage of having tunable pore sizes that depend on the identity of the intercalated cation and on the synthesis conditions [47]. It is generally accepted that the pores of a PILC have a slit-like geometry [76], even though spherical [77] and cylindrical [78] geometries are sometimes considered. Alumina is the most frequently encountered kind of pillar. Al-PILCs usually have an interlayer spacing of 7.5-9.0 Å [8, 14, 55, 59, 70], a surface area of 300-350 m^2/g [14, 46, 55, 57, 59], a pore volume of 0.180-0.230 cm^3/g [8, 55, 57, 69], and a microporous volume of 0.120-0.160 cm^3/g [14, 55, 57, 59, 69]. For comparison purposes, an activated carbon, that is highly

porous and especially microporous with pores of slit-like geometry, would exhibit a surface area of 1000 m^2/g [32], a pore volume of 0.600 cm^3/g [69], and a microporous volume of 0.450 cm^3/g [69]. The porosity of PILCs is comparable to that of zeolites and thus that kind of clay was proposed as an alternative to the HY zeolite (that has a surface area of 500 $m^2\ g^{-1}$ and a pore volume of 0.320 $cm^3\ g^{-1}$) in fluidized catalytic cracking (FCC) processes [73].

When pillared with metal oxides, a clay, originally hydrophilic, becomes hydrophobic [59] or at least moderately hydrophilic. PILCs have many potential applications due to their tunable acidity, their shape selectivity, their regular and high porosity, and their relatively high thermal stability (up to 600 ^oC [73, 74]). It is thus for those reasons that PILCs have primarily been applied as solid catalysts, especially in organic reactions [15, 79, 80] and gas oil cracking processes [73, 81].

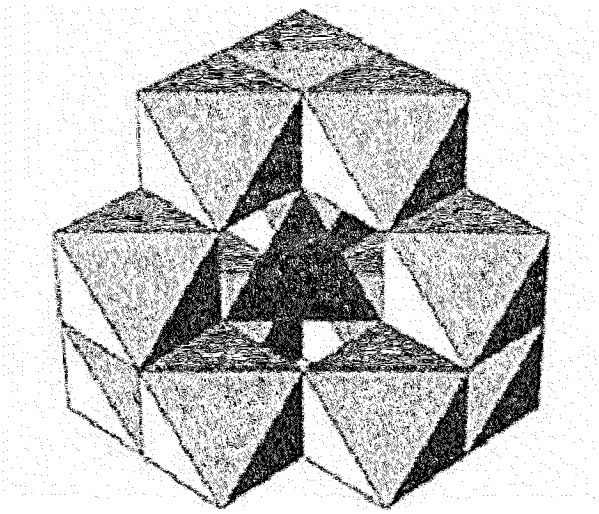

Figure 4: Atomic model of the Keggin ion [82]

In an Al-PILC, the intercalated metal polyoxocation is the Keggin ion whose formula is $[Al_{13}O_4(OH)_{24}(H_2O)_{12}]^{7+}$ [12, 68]. The Keggin ion is a cluster with one

aluminum tetrahedron surrounded by twelve aluminum octahedrons [79], and its diameter is of approximately 8.5 Å [12, 68, 80]. It is estimated that a stable Al-PILC contains at least 0.122 mmol of Keggin ion/g of clay [79]. During calcination, the Keggin ion yields Al_2O_3 pillars through the following reaction [15, 77]:

$$2\,[Al_{13}O_4(OH)_{24}(H_2O)_{12}]^{7+} \rightarrow 13\,Al_2O_3 + 17\,H_2O + 14\,H^+ \qquad \textbf{(12)}$$

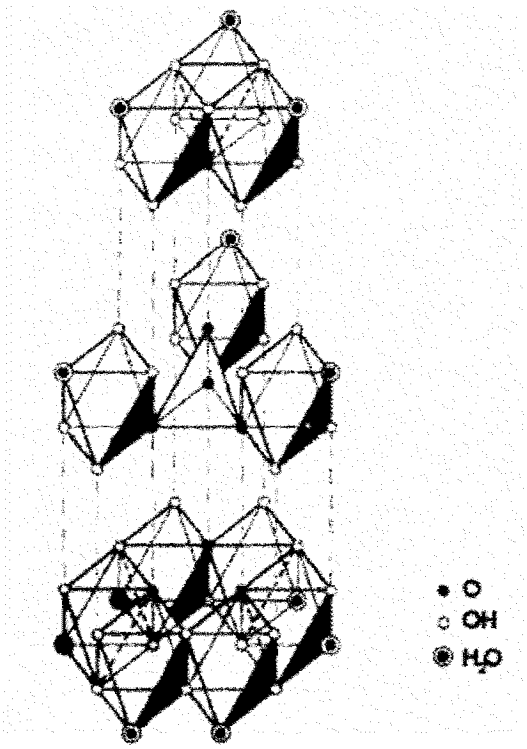

Figure 5: Blown-up atomic model of the Keggin ion [68]

Protons are then present in Al-PILCs, and in PILCs in general. These protons, due to their small size, migrate through the hexagonal holes of the silica layers to the alumina layers where they are in close proximity to the charge deficits [70, 77]. PILCs consequently possess strong Brönsted acid sites. They are thus classified as solid acids,

just like zeolites, and their acidity can exceed that of concentrated sulfuric acid [83]. Other proton sites exist in the clay layers. For montmorillonite, they are located at the Al-O-Mg linkage in the alumina layer, where Mg^{2+} substitutes for a Al^{3+} [63, 84]. But PILCs are acids predominantly of the Lewis type [78, 79, 85], which plays a role in applications like cracking [78]. Unlike Brönsted acid sites, Lewis acid sites do not stem from the layers but from the pillars [12, 70, 86]. Both Brönsted and Lewis acidities have been reported to decrease with the temperature of calcination [84].

Despite all their seemingly interesting properties, PILCs are sometimes further modified to increase their acidic or redox properties. Some groups have thus been loading PILCs with alkali [14, 46], alkaline earth [14], or transition metal cations [59, 79]. It is hoped by this way to obtain catalysts with superior properties, just as in the case of zeolites [59]. Furthermore, metal cation doping renders a PILC more hydrophilic [59]. PILCs that are cation-doped retain their pillared layered structures [59]. Cation-doping can be carried out by dispersing a PILC into a cation-containing solution [14, 59]. In that case, cations are loaded by cation-exchange with the remaining interlayer cations of the PILC, those that were not exchanged with the metal polyoxocations during the intercalation step leading to pillaring. These interlayer cations are the only ones from the PILC that can participate in this process. Indeed, the protons coming from the formation of oxide pillars are strongly bound to the octahedral alumina layers [14, 46, 59]. So doping a PILC by such a direct exchange results in a very low loading of cations [87]. In order to get a larger amount of doping cations, it is preferable to first pretreat the PILC before doping it. That pretreatment step involves adding slowly a dilute solution of NaOH to a PILC suspension containing Na^{+}, a common cation present in clays.

Neutralization of H^+ from the layers by the added OH^- then occurs. Electroneutrality of the PILC is then maintained by the loading of Na^+ from the suspension. These Na^+ migrate into the interlayer space and are thus available for cation-exchange. Using this method, the amount of loaded Na^+ can be controlled: the higher the pH during the Na^+ loading step, the larger the loading [59]. Nevertheless, the pH should not be too high, as a pH above 10 can damage pillars [59]. Location of doping cations in PILCs depends on the cations sizes and charges: they can be in the alumina sheet like protons, in the hexagonal Si-O cavities within the interlayer space where they are tightly held, or in accessible interlayer sites [14]. The smaller the cation, the closer it is from the charge deficits in the octahedral sheets [14]. When present in the clay gallery, doping cations seem to be located in the micropores [14, 59], which may be blocked by them [46]. If the conditions of their loading are slightly acidic, the doping cations are present in a highly dispersed phase as hydrate cations and do not form bulk precipitates of oxide or hydroxide [59].

Recently, pillaring has been carried out with sol particles of some oxides, particularly silica [88, 89]. These nanoparticles are larger than the metal polyoxocations used in traditional pillaring, and several layers of them can be stacked in the clay gallery. Clays pillared with such particles thus exhibit larger interlayer spacings and larger porosity: spacings as high as 50 Å have been reported, with surface areas of 700-850 m^2/g and pore volumes of 0.500 cm^3/g [88, 89]. Such materials have not really found practical applications yet, and they appear to have a weak acidity [89].

1.3.3. Porous Clay Heterostructures (PCHs)

Lately [90, 91], template synthesis has been applied to clay, giving so-called porous clay heterostructures (PCHs). PCHs have a larger porosity and wider pores than regular PILCs. To synthesize a PCH, a clay is intercalated with an organic surfactant that is concentrated enough to form micelles. The clay is then put in contact with a metal hydroxide solution. Metal oligomers condense on the surfactant micelles, mimicking the shape and size of the latter ones. Upon calcination at around 500 °C [13], the surfactant is removed and the clay layers are separated by an open-framework of metal oxide. This method yields solids with a uniform mesoporous structure and a large pore volume [13]. The surfactant only plays the role of a templating or structure directing agent and the resulting clay has a mean pore size that increases with the size of the surfactant [13]. The mesopores dimensions are directly linked to the size of the micelles and they can be controlled by the choice of surfactants. Besides larger interlayer spacing and larger pore volume than with pillaring, template synthesis gives clay materials higher thermal stability [13]. A PCH synthesized from montmorillonite would then exhibit an interlayer spacing of 24 Å, a surface area of 600-700 m^2/g, a pore volume of 0.700-1.000 cm^3/g, and micropores 15-20 Å wide [13, 75].

So far, silica is the most widely used oxide in the formation of PCHs, with quaternary ammonium ions and amines as templating surfactants [51]. Some PCHs though have been synthesized with alumina as the oxide and alkyl polyether as the surfactant [92]. For the synthesis of a silica PCH, a clay is first exchanged with quaternary ammonium cations. After being washed to remove excess surfactants and anions, the then-obtained material is preswelled with an amine cosurfactant. Afterward, a

solution of tetraethyl orthosilicate (TEOS) $Si(OC_2H_5)_4$ is added to the suspension, with a TEOS:amine ratio of at least 7.5 [15].

The whole mechanism of PCH formation is actually not known with certainty, and it is not quite clear what are the respective roles ionic and non-ionic surfactants and how they interact with the silica precursor. It is believed that during the synthesis, TEOS hydrolyzes, condenses, and polymerizes into silicate around mixed micelles of neutral and ionic surfactants [90]. Besides preswelling the clay to allow TEOS to penetrate the clay gallery, it is thought that the amine base catalyses the hydrolysis of TEOS inside the clay gallery with water originally present there, which would explain why silica practically only forms inside the clay and not outside of it [90, 93]. The relationship between pore sizes and surfactant lengths is not well established either. Despite an amine:ammonium ratio of usually 10:1 [93], the amine is nevertheless considered as the co-surfactant, and the question regarding which surfactant determines the PCH pore sizes remains unanswered. Similarly, the nature of the interaction between the surfactant micelles and the silicate is in question. By analogy with what takes place during the surfactant-directed synthesis of the mesoporous M41S silicas, the surfactants and the silicate interact either through electrostatic forces or hydrogen bonding. Indeed, while in the formation of MCM-41 neutral amine surfactants pair with neutral silicate [94, 95], positively charged ammonium cations assemble with silicate anions through electrostatic charge matching during the synthesis of HMS [96].

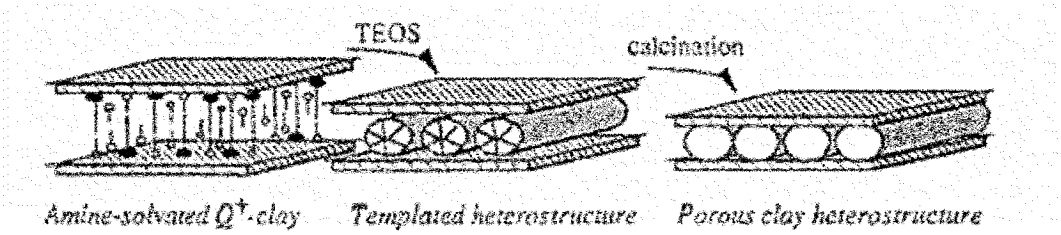

Figure 6: Principles of template-synthesis with a quaternary ammonium cation-exchanged clay dispersed in an amine cosurfactant solution [51]

For specific applications, a few groups have used mixed oxides as intercalates, with silica as the main component [13, 75]. The amount of the other oxides is usually one order of magnitude smaller than that of silica. The resulting PCHs contain a framework of silica with metal oxide deposited on it as thin layers or in a highly disperse state. Pure particles of the metal oxide do not form. Different methods have been employed to synthesize such materials. Zhu *et al.* [13] first formed mixed silica/titanium oxide sols that were intercalated between clay layers. Quaternary ammonium was then added. According to the authors, such a PCH could be used in the catalytic oxidation of alkanes into alcohols and ketones. In another study [75], Choy *et al.* prepared a PCH by mixing a solution of TEOS, $CoCl_2$, and dodecylamine to a clay that had previously been exchanged with quaternary ammonium. Their material was used for the catalytic conversion of NO_x. But despite these examples, only a few applications have been found for PCHs.

2. OBJECTIVES

The purpose of this study was to synthesize and characterize materials, starting from a natural clay mineral, that could serve as adsorbents and catalysts. To be an efficient adsorbent, a material should contain pores of molecular sizes and active species that can potentially bind to adsorbate molecules or favor chemical reaction. Throughout the study, cations of iron, zinc, and copper played the role of active species for potential adsorption, catalysis, or oxidation applications.

In a first step, the clay was modified with various chemicals in order to create porosity and introduce metal species. Porosity in the clay was generated by the intercalation of stable metal oxide species between the clay layers, under the form of either pillars or open frameworks. These porous clays were then loaded with metal through cation-exchange process. The clay was also used to prepare porous carbonaceous materials. Thus, modified porous clay materials served as templates in the preparation of carbons, while in another procedure, the nonporous clay acted as a binder for an already porous powdered carbon. Metal was be loaded in the resulting carbonaceous materials through the use of metal-containing clay materials.

The overall porosity and structure of the newly obtained materials were characterized by analytical techniques such as N_2 adsorption, XRD, SEM and TEM. The identity and the amount of the different metal species was determined by ICP, XRF, XRD, SEM, and TEM. To evaluate the location, accessibility, state of aggregation, and

degree of dispersion of the metals, a test reaction of hydrogen sulfide adsorption from air was carried out on all samples, since hydrogen sulfide has been proven to be reactive toward the selected metals and its molecule is small enough to penetrate into even the smallest pores.

3. EXPERIMENTAL

3.1. Materials

Sodium montmorillonite: Na-M. Clay modifications were all carried out starting from the same material, namely Swy-2, a natural Wyoming montmorillonite. It was purchased from the Source Clay Minerals Repository, Purdue University (West Lafayette, IN). It is a Na-rich montmorillonite whose theoretical formula is $(Ca_{0.12}\ Na_{0.32}\ K_{0.05})\ [Al_{3.01}\ Fe(III)_{0.41}\ Mn_{0.01}\ Mg_{0.54}\ Ti_{0.02}][Si_{7.98}\ Al_{0.02}]O_{20}(OH)_4$. The layer charge is of – 0.55 and the CEC is of 0.764 meq g^{-1}.

Ferric chloride, zinc nitrate, and copper chloride: $FeCl_3$, $Zn(NO_3)_2$, and $CuCl_2$. $FeCl_3.6H_2O$ from Mallinckrodt, and $Zn(NO_3)_2.6H_2O$ and $CuCl_2.2H_2O$ from Fischer Scientific were the metal salts used in all cation-loading steps.

Chlorhydrol®. Al-pillaring was carried out with Chlorhydrol®. It is a solution of aluminum chlorohydrate manufactured by Reheis, Inc. The product that we used originally contained 50% (mass) of $Al_2Cl(OH)_5.(2.5\ H_2O)$.

Bentonite: BEN. Bentonite is an impure montmorillonite clay, with usually more than 90% of montmorillonite. The main impurity is quartz [80]. The characteristics of BEN as a clay (CEC, exchangeable cations, layer thickness, etc.) are thus similar to the ones for Na-M. The bentonite was obtained from WYO-BEN, Inc, and it was used in its as-received form as a binder in the preparation of carbon/clay composites.

WV-B carbon: WV. WV-B is a wood-based carbon manufactured by Westvaco. Its chemical activation is obtained through phosphoric acid [97], which results in 5% (mass) of phosphorus in the material. The binding of that carbon with clay was aimed at improving its mechanical and adsorbing properties.

Octylamine (Oc) and dodecyltrimethylammonium bromide (DoB) surfactants. Octylamine $CH_3(CH_2)_7NH_2$ (99%) and dodecyltrimethylammonium bromide $CH_3(CH_2)_{11}N(CH_3)_3^+Br^-$ were the surfactants that served in the synthesis of porous clay heterostructures. They were obtained from Sigma-Aldrich and had a purity of 99%.

Tetraethyl orthosilicate: TEOS. Tetraethyl orthosilicate $Si(OC_2H_5)_4$ was the silica source in the preparation of porous clay heterostructures. It was a 98% pure product from Sigma-Aldrich.

Sucrose. Sucrose from Sigma-Aldrich was the source of carbon in the synthesis of templated carbons.

Fe^{3+}-exchanged montmorillonite: Fe-M. 10 g of Na-M was dispersed in 500 mL of water. After stirring overnight, a 0.1 M solution of $FeCl_3$ was added dropwise to the clay suspension, until the Fe/clay ratio reached 10 mmol of Fe^{3+} per g of clay [98]. The resulting suspension was stirred overnight at room temperature. All the clay material initially used was modified as was indicated by the uniformity of the suspension. The suspension was then diluted to a total volume of 4 L and washed until the conductivity of the filtrate was less than 30 μS. The exchanged clay was then filtered using a Büchner-type funnel with a filter paper retaining particles larger than 11 μm. It was then dried at room temperature and calcined at 400 ^{o}C for 4 h.

Montmorillonite modified with iron oxocations: FeOx-M. 250 mL of 0.5 M NaOH was added dropwise to 250 mL of 0.2 M $FeCl_3$ (Fe/OH = 2.5) to generate an iron oxocation solution [99] that was then added dropwise to a 500 mL suspension with 10 g of Na-M. After aging overnight, the new suspension proved uniform, which indicated clay modification, with large aggregates resulting from the coagulation action of iron species. The resulting material was washed, recovered, dried, and calcined the same as with Fe-M. The sample before calcinations will be referred as FeOx-IM.

Al-pillared montmorillonite: Al-M. The Al-pillaring solution was obtained by diluting the Chlorhydrol® solution to a concentration of 0.1 M. It was added dropwise to a 500 mL suspension containing 10 g of Na-M so that the final Al/clay ratio was of 10 mmol g^{-1}. The obtained suspension was stirred overnight. When stirring was stopped, two phases turned out to be present in the suspension: a bottom phase with white

agglomerates that was identified as Al-intercalated montmorillonite and an upper phase with fine dispersed particles that was attributed to unmodified Na-M. The latter phase was removed by subsequent pipetting out, while the remaining intercalated material was washed, recovered, dried, and calcined at 400 ^{o}C for 4 h. The material before and after calcination will be referred to respectively as Al-IM and Al-M, the former being intercalated with the Keggin ion and the latter being pillared with alumina.

Metal cation-doped Al-pillared montmorillonite: MeAl-M, Me=Fe, Zn, or Cu. 10 g of Al-M was dispersed in 1 L of a NaCl 0.2 M solution, the Na/clay ratio being thus of 20 mmol g^{-1}. The pH of the suspension being originally of about 4.6, it was brought to a value of 9 by adding dropwise a 0.05 M NaOH solution. It is important that the NaOH solution is diluted enough to avoid any local pH value that would be to high and thus damage the Al-pillars [59]. A pH of 9 was maintained by periodic additions of NaOH overnight. 10 g of powder clay obtained by this pretreatment was then dispersed into 500 mL of water. A 0.2 M solution of $FeCl_3$, $Zn(NO_3)_2$, or $CuCl_2$ was added dropwise to that clay suspension until the Me/clay ratio was of 20 mmol g^{-1}. The resulting suspension was stirred overnight. Agglomeration of the clay was observed. The clay was then washed, recovered, dried, and calcined the same way as with Fe-M.

Porous Clay Heterostructures (PCHs): Si-AlM and Me-SiAlM, Me=Fe, Zn, or Cu. Na-M was dispersed in water to make a suspension of 20g L^{-1}. A 0.2 M solution of dodecyltrimethylammonium bromide (DoB) was added dropwise to that suspension until a cation/clay ratio of 2 mmol g^{-1} was reached. The resulting material was retrieved by centrifugation and washed with water to eliminate excess of cation. It was then dried at

room temperature. The powder was afterwards swelled with octylamine (Oc), with an amine/clay ratio of 20 mmol g^{-1}. TEOS was then added, with a TEOS/clay ratio of 150 mmol g^{-1}. The solid was separated by centrifugation and dried at room temperature. Finally, it was calcined at 450 °C for 4 h. That PCH will be referred as Si-AlM, while its counterpart before calcination will be Si-AlMH. An additional sample of Si-AlMH calcined at 500 °C was prepared and will be referred as Si-AlM500.

Metal-containing PCHs were obtained by adding 0.2 M solutions of $FeCl_3$, $Zn(NO_3)_2$, or $CuCl_2$to a 20g L^{-1} suspension of a PCH before its final calcination step. The solids were then recovered, dried, and calcined the same way as for Si-AlM. They will be referred as Fe-SiAlM, Zn-SiAlM, and Cu-SiAlM.

To determine the role and the influence on porosity of the surfactants Oc and DoB and of the silica precursor TEOS, additional materials were synthesized. Thus, Na-M solely modified with Oc, DoB, and TEOS (in the same ratios as for the synthesis of Si-AlM) were prepared and respectively referred to as Oc-M, DoB-M, and Si-AlM0. Samples obtained with only one of the two surfactants, Oc or DoB, and TEOS were also prepared and were respectively named Si-OcAlM or Si-DoBAlM. Finally, samples were obtained by using only the two surfactants and no TEOS, and they were named OD-MH and OD-M, the latter being calcined at 450 °C for 4 h.

Metal cation-exchanged bentonite: MeB, Me=Fe, Zn, or Cu. 10 g of BEN was dispersed in 500 mL of water and the suspension was stirred overnight. 500 mL of $FeCl_3$, $Zn(NO_3)_2$, or $CuCl_2$ 0.2 M was added dropwise to the clay suspension, the Me/clay ratio being 10 mmol g^{-1}. After stirring overnight, the suspension was filtered and the solid was dried at room temperature.

WV-B carbon mixed with 10 % of bentonite: BW and Me-BW, Me=Fe, Zn, or Cu. 6 g of BEN was dispersed in 300 mL of water, and the suspension was stirred at 60 °C overnight. 54 g of WV-B carbon was then added. After stirring overnight, the water was evaporated until only a dry solid remained. The solid was ground to fine powder. Water was slowly added to the powder until a compact paste formed. The paste was extruded to granules that could be sliced to smaller granules of 1-2 mm.

Metal-containing carbon/clay composites were obtained by replacing BEN with MeB.

Templated carbons: C-M and Me-CM, Me=Fe, Zn, or Cu. Each gram of PCH used was mixed with 1.3 g of sucrose, 0.1 mL of H_2SO_4, and 6 mL of water for 1 h. In the presence of H_2SO_4, sucrose dehydrates, condenses, and polymerizes into a carbon precursor [24, 100]. The role of H_2SO_4 was also to accelerate the carbonization of sucrose, so that it starts at a lower temperature [24]. The suspension was then dried at 100 °C before being calcined at 160 °C for 4 h. The material was not washed with water prior to its calcination to avoid displacement of the intercalated sucrose by water [25]. Each gram of the resulting powder was mixed with 0.8 g of sucrose, 0.1 mL of H_2SO_4, and 6 mL of water. After drying at 100 °C and calcination at 160 °C, the solid was carbonized for 1 h at 900 °C under a N_2 atmosphere so that the sucrose transforms into carbon [101].

The carbon/clay composite thus obtained at that point, without any metal loaded into it, will be referred to as C-SiAlM.

All the carbon/clay composites afterward were treated with concentrated HF overnight. They were then washed with water until the pH of the filtrate was constant. The materials at that point will be referred to as C-AlM, Fe-CalM, Zn-CAlM, and Cu-CAlM. Finally the materials were treated with concentrated HCl, following the same procedure as with HF. The purpose of the HF and HCl treatment was to remove the inorganic phase so that only carbon material would be left, with its structure preserved [37, 102].

3.2. Methods

X-Ray Diffraction (XRD). In order to determine the basal spacing d_{001} of the samples, XRD was carried out on them. d_{001} was calculated from the diffraction peaks by applying the Bragg's law:

$$n\lambda = 2d_{001}\sin\theta \qquad \textbf{(13)}$$

where n is an integer, λ is the wavelength of the X-rays (nm or Å), and θ is the angle of incidence of the X-ray beam to the lattice plane (rad). The interlayer distance in clay samples was found by substracting the thickness of a montmorillonite layer (9.6 Å) from d_{001} [46].

XRD (40 kV, 30 mA) was performed on a Rigaku X-ray diffractometer that uses Cu K_α (1.54184 Å) as the source of radiation. The analyzed samples were spread as thin

layers on a glass slide. Diffractions were obtained by variation of 2θ (θ being the Bragg angle) from 2.000 ° to 10.000 °, with increments of 0.008 °, or from 5.00 ° to 70.00 °, with increments of 0.02 °.

N_2 Adsorption. To characterize the porosity of the samples, N_2 adsorption at its boiling temperature of –196 °C was performed. Adsorption isotherms of adsorbed volume of N_2 V_a (cm^3 of N_2 per g of sample STP) vs. P/Po were thus determined by using the ASAP 2010 from Micromeritics®. Prior to adsorption, all samples (weighing around 0.1 g) were outgassed at 120 °C and at 4 μm Hg for 24h in order to desorb impurities from the samples pores, especially water. Adsorption of N_2 started at a P/Po value of around 10^{-6} from which it was gradually raised with successive N_2 volume increments of 5 cm^3 g^{-1} until P/Po = 0.1. Afterwards the instrument followed a preprogrammed pressure table.

The BET model being the one most frequently used in surface area determinations, it is the formalism that was chosen for all the studied materials to give S_{BET}. It is nevertheless noteworthy to mention that for microporous materials, and especially pillared clays (PILCs), the Langmuir model [9, 103] may be more adapted [14]: the BET equation may give an underestimate of the actual surface area from such materials [46]. The Langmuir model assumes a dynamic equilibrium similar to the one in the BET model, but with only one layer of adsorption.

The micropore volume V_{DR} was determined through the Dubinin-Radushkevich equation [7, 8] while the total pore volume V_t corresponds to the quantity adsorbed when P/Po ~ 0.99.

The pore size distributions (PSDs) were determined through the DFT Plus software that came with the instrument. For all the samples containing at least 90% (in

mass) of carbon, the original DFT model was applied. For the clay samples obtained through modification with different iron species or pillared through the Keggin ion (and sometimes additionally doped with metal cations), as they were anticipated to be microporous, the modified DFT model was used, with the pores considered as cylindrical. As it is generally accepted that the pores of a PILC are slit-shaped, a rectangular geometry would be beforehand more adapted to explain the area/volume ratio increase that happens during clay pillaring [10, 19]. But as the DFT Plus software can only manage one spatial dimension, the cylindrical geometry was chosen as an approximation. As porous clay heterostructures (PCHs) are usually mesoporous, the hybrid DFT was chosen for these materials.

Thermal Analysis. Thermal analyses (TAs) were done on a SDT 2960 from TA Instruments. A minimum of 20 mg of sample was heated from room temperature (20-30 ^{o}C) to 1,000 ^{o}C with a ramp of 10 ^{o}C min^{-1}, under a N_2 or air flow of 100 mL min^{-1}. From the changes in sample mass with temperature, TG (ThermoGravimetric) and DTG (Derivative ThermoGravimetric) data were determined.

H_2S Breakthrough Tests. To assess the adsorptive properties and to determine the location of the active species, the prepared samples were tested for the adsorption of H_2S from moist air at room temperature.

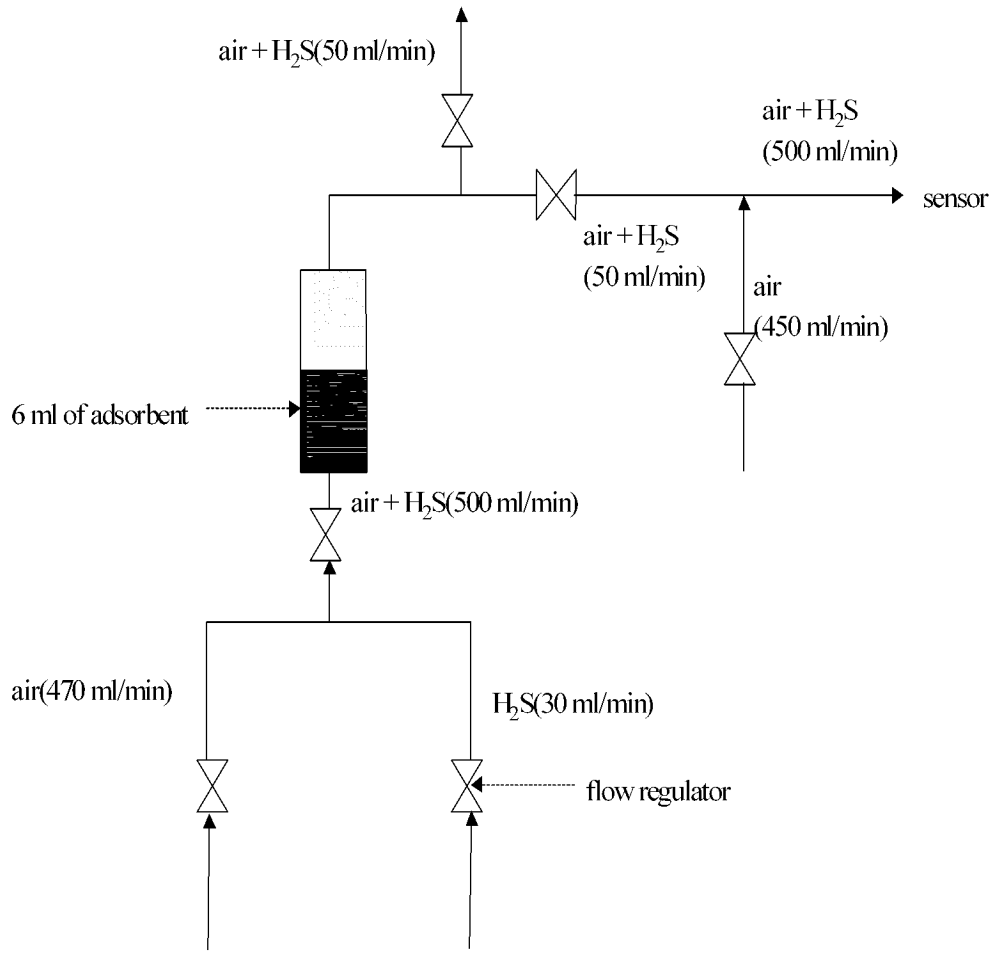

Figure 7: Experimental setup for the determination of the H_2S breakthrough capacities

Approximately 6 mL of sample, with particles 2-3 mm wide, was loaded into a column 60 mm long, with a diameter of 9 mm. Before H_2S was flowed in, the adsorbents were at first prehumidified with wet air (80% of approximate relative humidity at 25 ^{o}C) flowing at 470 mL min^{-1} for 90 min (60 min for the carbon-containing samples). The quantity of water adsorbed was estimated by measuring the sample weight increase. After weighing, the sample was placed back into the column. This time, in addition to the previous wet air stream, a H_2S stream at 30 mL min^{-1} was passed through the sample: the

combination of these two streams resulted in a gas stream flowing at 500 mL min^{-1}, with a H_2S content of 3,000 ppm (0.3%). The column-exiting stream was diluted 10 times with the same wet air. The diluted stream was then directed to an Interscan LD-17 sensor that can measure H_2S concentrations from 0.1 to 100 ppm. The sample was considered exhausted when a H_2S concentration of 100 ppm was reached. A breakthrough curve [H_2S] vs. time could then be plotted and the cumulative quantity of H_2S adsorbed on the sample was found by integrating the area above the breakthrough curve and by using the H_2S concentration in the inlet gas, the flow rate, the breakthrough time, and the mass of adsorbent.

pH. For understanding which forms of H_2S could have adsorbed on the samples, the pH of a suspension containing the samples before and after H_2S exposure was measured. The suspensions were prepared by dispersing 0.4 g of the sample into 20 mL of water. They were stirred overnight then filtered, and the pH of the filtrate was measured. Comparison of the pHs before and after adsorption of H_2S allowed to assess whether the products of adsorption were acidic, basic, or neutral.

Elemental Analysis. The metal contents were determined through inductively coupled plasma emission spectroscopy by Huffman Laboratories (Golden, CO) and Shiva Labs (Syracuse, NY).

Scanning Electron Microscopy (SEM). SEM images were obtained on a LEO 1455 VP SEM with tungsten source at Lamont- Doherty Earth Observatory of Columbia

University (Palisades, NY) and on a Hitachi SEM at the School of Earth and Environmental Sciences at the Queens College of the City University of New York (New York, NY).

Transmission Electron Microscopy (TEM). TEM analysis was performed on a Zeiss EM 902 at the Science Division at the City College of the City University of New York.

X-Ray Fluorescence (XRF). XRF analyses were carried out on a Spectro 300 T from ASOMA Instruments, Inc. The instrument consists of a Ti-target X-Ray tube. Determination of the metal contents of the carbon-containing samples was achieved by measuring the concentration of the filtrates obtained from the filtration of carbon or clay after they had been exchanged with metal cations (Fe^{3+}, Zn^{2+}, and Cu^{2+}) in 0.2 M solutions. The concentrations of these solutions were estimated by making a calibration curve. Five data points were used to set up this curve, which was a straight line passing through the origin, and the correlation coefficient was above 0.99. The data points corresponded to standard solutions whose metal ion concentrations were 0.04, 0.08, 0.10, 0.14, 0.16, and 0.20 M. The tube voltages chosen for Fe, Zn, and Cu solutions were respectively 16, 20, and 18 kV, while the tube currents were respectively 560, 150, and 300 μA. The ROIs (Region of Interests) of the spectra were respectively at 5.902-6.896, 8.052-9.208, and 7.482-8.598 keV, using K_α lines. A background correction was done in the 12-20 keV region and the count rate of the most concentrated standard (0.20 M) was around 20,000 cps (counts per second). Each determination took 100 s.

XRF was also used to qualitatively determine the evolution of metal contents through successive modifications in the PCHs and in the templated carbons. In that case, the tube voltage was set at 24 kV with a current of 8 μA. The count and warm-up times were respectively 40 s and 4 s. The region of interest (ROI) was between 7 and 11 keV, while a background correction was done between 12 and 17 keV.

Fourier-Transform InfraRed spectroscopy (FT-IR). Transmittance spectra were obtained with a Nicolet Impact 410 FT-IR equipped with a DTGS KBr detector. The wavelength region of interest was in the 400-4,000 cm^{-1} range. The resolution was set at 4 cm^{-1}. Each spectrum was the result of 32 scans, with a mirror velocity of 0.3165 cm s^{-1}. The background was recorded every 30 min and was subtracted from the spectra. A correction for H_2O and CO_2 was made.

4. RESULTS AND DISCUSSION

4.1. Clays Exchanged with Metal Cations

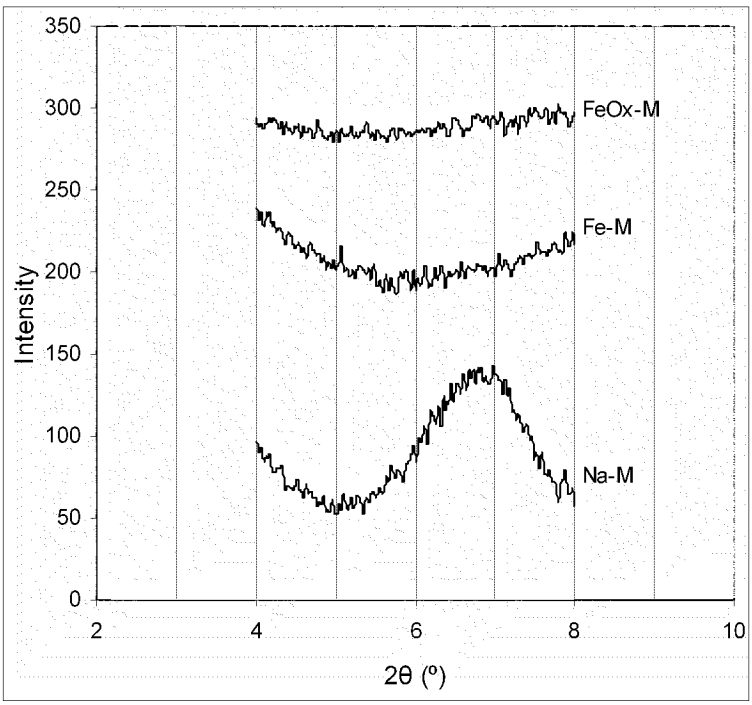

Figure 8: XRD of Na-M, Fe-M, and FeOx-M

The starting clay Na-M was exchanged with Fe^{3+}, Zn^{2+}, and Cu^{2+}. The structural and chemical properties of the Fe^{3+}-exchanged clay, Fe-M, were compared to the ones for an iron oxide pillared material, FeOx-M, using also Na-M as the starting clay. The iron pillaring solution was obtained by adding a solution of NaOH to a solution of $FeCl_3$. Evolution of the XRD pattern upon modification can be seen in Figure 8.

Na-M has a diffraction peak at $2\theta = 6.98^{o}$ due to d_{001}. This corresponds to a basal spacing d_{001} of 12.7 Å according to the Bragg's law. By subtracting 9.6 Å, the thickness of a montmorillonite layer, to the basal spacing [46], an interlayer spacing of 3.1 Å is obtained: Na-M has thus one layer of hydration in its interlayer space [58]. The peak due to d_{001} is not present in the cases of Fe-M and FeOx-M. For Fe-M, it might be due to some interaction of Fe^{3+} with the clay layers, especially the alumina ones. That kind of interaction, such as the replacement of some Al^{3+} by Fe^{3+}, could weaken the clay layers that would then lose part of their well-ordered structure once Fe-M is heated to 400 ^{o}C. Nevertheless, it is expected that the interlayer spacing with Fe-M is even smaller than that with Na-M, as Fe has a smaller atomic radius than Na [104].

On the other hand, the absence of any diffraction peak with FeOx-M can be explained by the fact that attempts to pillar a clay with iron oxocations often lead to delaminated, instead of pillared, materials [24, 63], especially for the long reaction times in our synthesis. Despite showing no 001 reflection, delaminated clays still possess some localized short-range order with stacks of pillared layers arranged in a "house-of-cards structure" (see Figure 9). Delaminated clays do possess micropores, but fewer than PILCs [63]. Nevertheless, little is known about the process of the clay structure breakdown leading to delaminated clays.

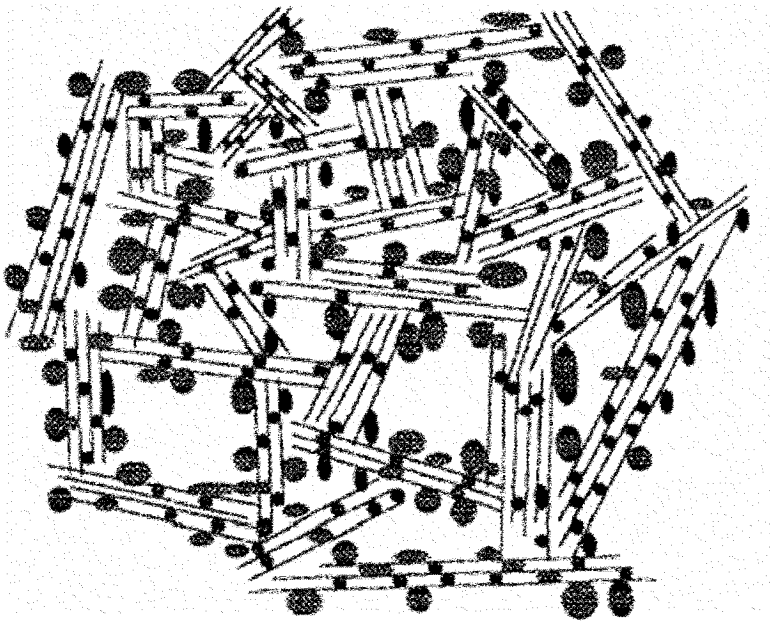

Figure 9: Schematic representation of an iron oxide delaminated clay [63]

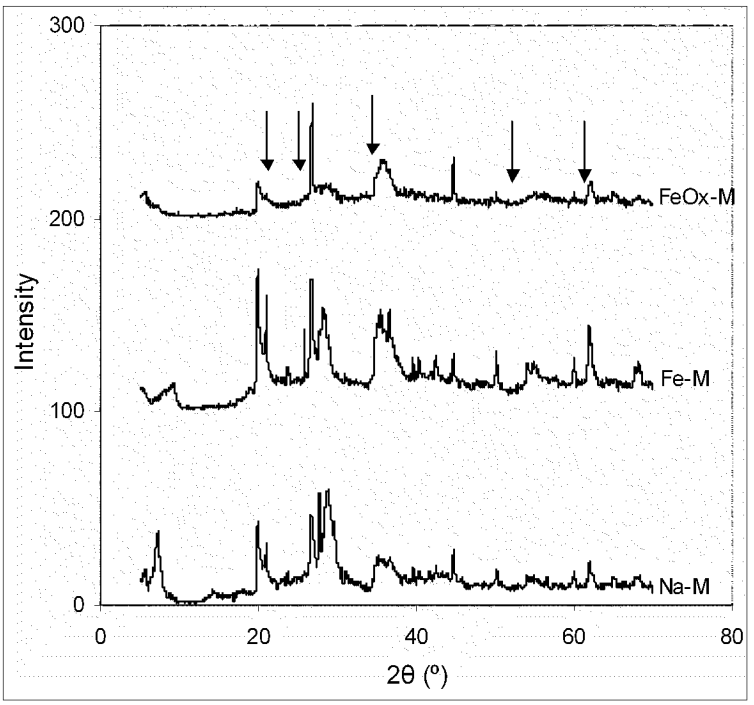

Figure 10: Extensive XRD of Na-M, Fe-M, and FeOx-M

A more extensive scan of the samples between 5 ° and 70 ° (Figure 10) allowed identification of the iron present on the outer clay surface of FeOx-M as a mixture of iron oxides and hydroxides, namely FeO(OH) goethite (21.2 ° and 53.2 °), FeO(OH) lepidocrocite (27.1 °), and Fe_2O_3 hematite (35.6 ° and 62.4 °), that is known as limonite [58].

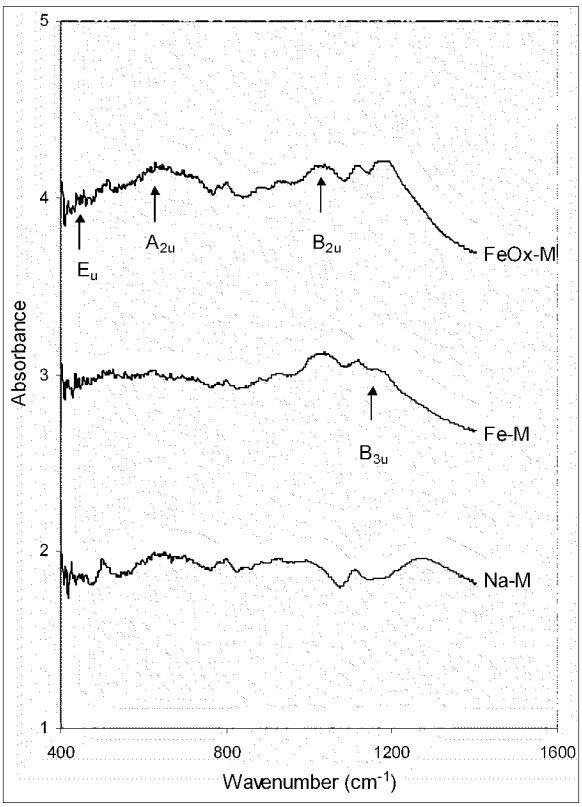

Figure 11: FT-IR of Na-M, Fe-M, and FeOx-M

FT-IR spectroscopy gives further details about the iron phases present in Fe-M and FeOx-M (Figure 11). Bands at 450 cm^{-1} and 630 cm^{-1} for FeOx-M respectively account for the E_u and A_{2u} vibration modes in α-Fe_2O_3 [105], while absorptions at 1040

cm^{-1} and 1170 cm^{-1} in FeOx-M and Fe-M for respectively the B_{2u} and B_{3u} in-plane bending modes of -OH are characteristic of γ-FeO(OH) lepidocrocite [106].

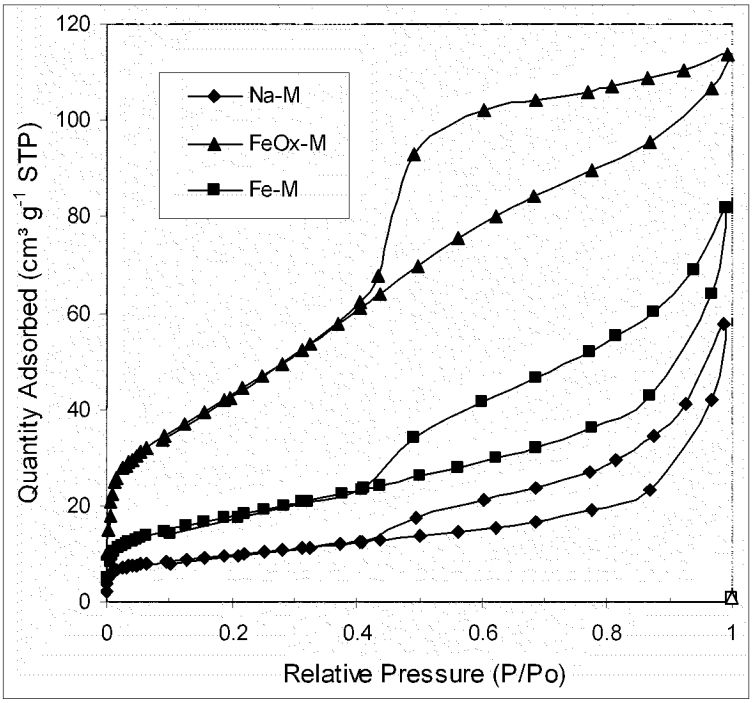

Figure 12: N_2 adsorption-desorption isotherms of Na-M, Fe-M, and FeOx-M

The porosity for Na-M, Fe-M, and FeOx-M was characterized using N_2 adsorption. The adsorption isotherm for Na-M (Figure 12) is of type II according to the IUPAC classification [5], which indicates, as expected, a nonporous or macroporous material whose surface sees more than one monolayer of N_2 forming. Fe-M has the same kind of porosity as Na-M as it exhibits a similar isotherm. It can be seen though that, the isotherm for Fe-M being situated above the one for Na-M, Fe-M is slightly more porous than Na-M. With a higher N_2 uptake at low pressure, it even appears that Fe-M is a little more microporous than Na-M. That finding is a bit surprising, since the interlayer

spacing in Fe-M is smaller than the one with Na-M. As a consequence, new micropores created with Fe-M cannot be the result of intercalated species between the clay layers. Since the diameter of a N_2 molecule is of 3.6 Å, porosity generated between the layers can only be detected by N_2 adsorption when the interlayer spacing is larger than that diameter. For Na-M and Fe-M, the spacing is no larger than 3.1 Å as seen from XRD. Consequently, the new micropores in Fe-M must be the result of the presence of small adsorbed iron oxide particles on the clay surface between which the pores are [99]. FeOx-M also has a type II isotherm, but that sample appears quite significantly more microporous than Na-M and Fe-M. It is then likely that a few iron species have been intercalated in the case of FeOx-M.

All these three samples exhibit a hysteresis loop, which indicates the presence of mesopores [14]. For Na-M and Fe-M, the hysteresis loop is of type H_4 according to the IUPAC classification [107], which is the result of open slit-shaped capillaries [2, 3]. On the other hand, FeOx-M has mesopores that are open capillaries of ink-bottle shapes [2, 3] as its H_2-type hysteresis loop suggests. The overall porosity in FeOx-M is much larger than that for Na-M and Fe-M, as can be seen from the quantity adsorbed at P/Po ~ 0.99, and that is due mainly to newly generated mesopores. These mesopores probably come from the deposition of large iron oxide clusters on the clay surface [63].

Pore size distributions (PSDs) give a more precise idea of the porosity evolution upon modifications (Figure 13). Na-M thus possesses some degree of microporosity, with peaks on its PSD at 6.3 Å and at 10-12 Å. These peaks are relatively very small, so microporosity in Na-M only represents a negligible fraction of the total porosity. These micropores must stem from impurities (the clay was used as-received) present on the clay surface.

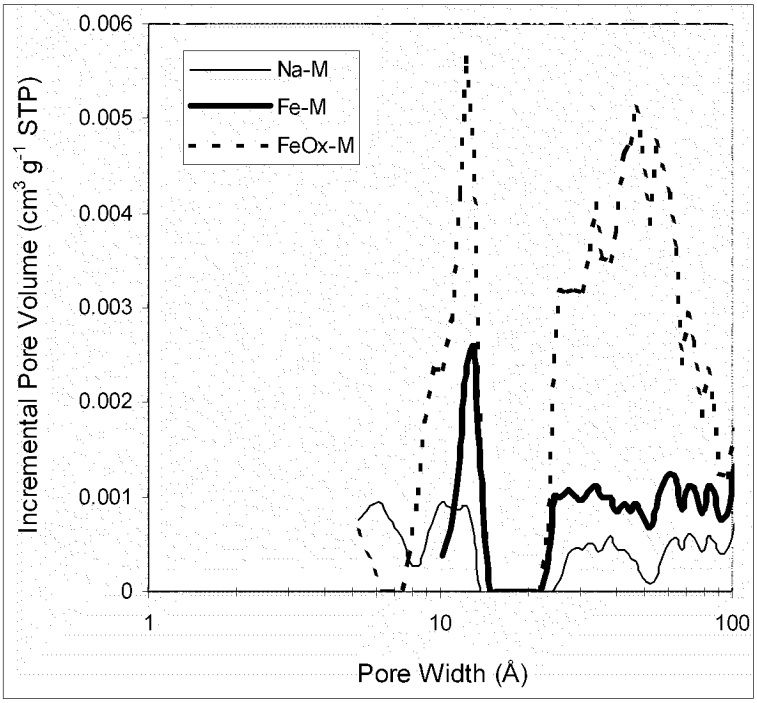

Figure 13: Pore size distributions of Na-M, Fe-M, and FeOx-M

With Fe-M, porosity is generated, both in the micropore (1-20 Å) and mesopore (20-100 Å) regions. The micropore peak at 6.3 Å has disappeared, which would be consistent with the removal of the impurities that were responsible for that peak in Na-M during Fe-M washing. Aside from that, exchanging Na-M with iron notably generates micropores that are 13 Å wide along with mesopores of various widths. As mentioned previously, all these newly formed pores are most probably the result of the adsorption of iron oxide species on the clay surface. It is unlikely that the new micropores are present between the layers. If it were the case, the peak at 13 Å should be much higher, since any intercalation should entail a much larger microporosity increase. In contrast, the peak at 12.4 Å with FeOx-M could very well be the result of micropores in the interlayer space. Nevertheless, the mesopore gain in FeOx-M is significant as well. Thus, iron-pillaring solution that has been used to prepare FeOx-M must have contained both small iron oxide

species that were intercalated and large iron clusters, whose diameters ranged between 30 and 100 Å [109], that were too big to be intercalated and instead formed deposits on the clay surface.

	S_{BET} ($m^2 g^{-1}$)	V_{DR} ($cm^3 g^{-1}$)	V_t ($cm^3 g^{-1}$)
Na-M	33	0.014	0.088
Fe-M	63	0.025	0.124
FeOx-M	160	0.062	0.174

Table 1: Structural parameters of the iron-modified clay samples

Structural parameters determined from the isotherms (Table 1) confirm the previous findings. In addition, it can be seen that the micropore and total pore volumes both increase significantly from Na-M to FeOx-M, which confirms the size heterogeneity of the species present in the iron-pillaring solution. Furthermore, the surface area found for FeOx-M is very close to the one for a delaminated iron-pillared clay from another study [63], which is another indication that FeOx-M is indeed delaminated.

The DTG curve for Na-M under a N_2 atmosphere (Figure 14) shows two peaks, at 70 ^{o}C and at 680 ^{o}C. They respectively correspond to the removal of physically adsorbed water and to the dehydroxylation of the tetrahedral silicate clay layers [75]. DTG peaks situated before 100 ^{o}C are usually attributed to desorption of water weakly adsorbed on the surface of the samples.

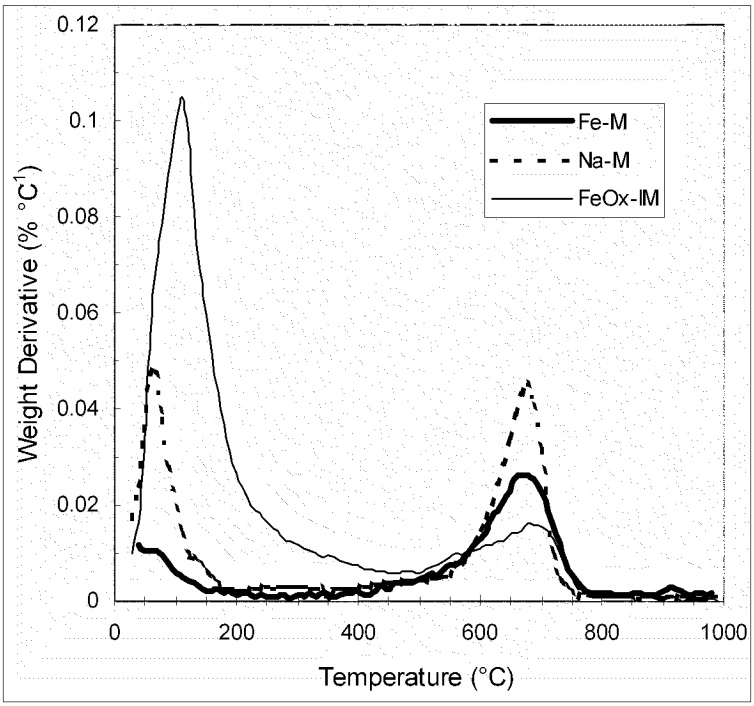

Figure 14: DTG curves of Na-M, Fe-M, and FeOx-IM

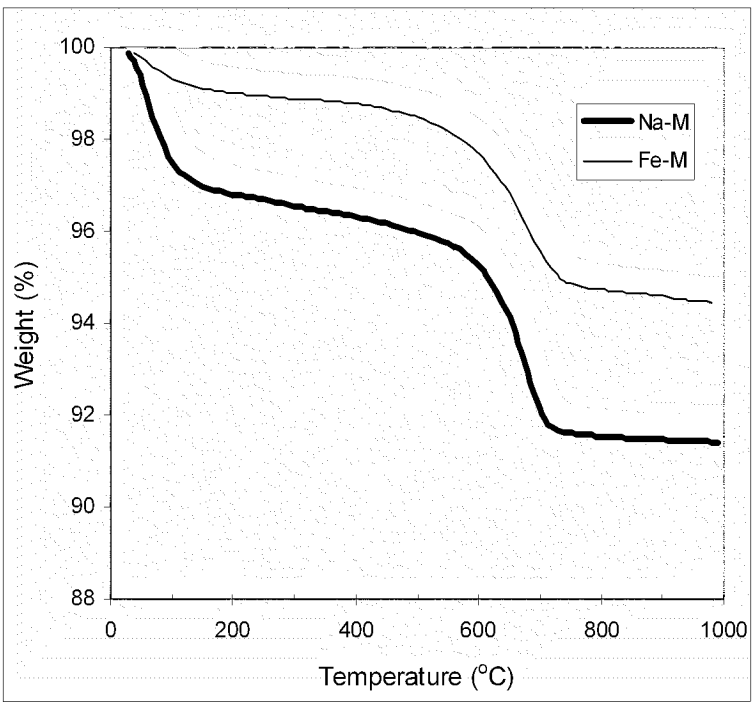

Figure 15: TG curves of Na-M and Fe-M

From its TG curve (Figure 15), the weight loss associated with the dehydroxylation of Na-M starts at around 600 °C and represents 4% of weight loss. As expected, Na-M and Fe-M have comparable thermal characteristics, as they exhibit DTG and TGA curves with similar patterns and peaks (Figures 14 and 15).

The DTG curve for FeOx-IM (Figure 14) has peaks located at the same positions as for Na-M and Fe-M. But its TG curve (Figure 16) shows some marked differences. Indeed, after initial desorption of water at 110 °C, FeOx-M undergoes more drastic weight decreases than Na-M and Fe-M until about 500 °C.

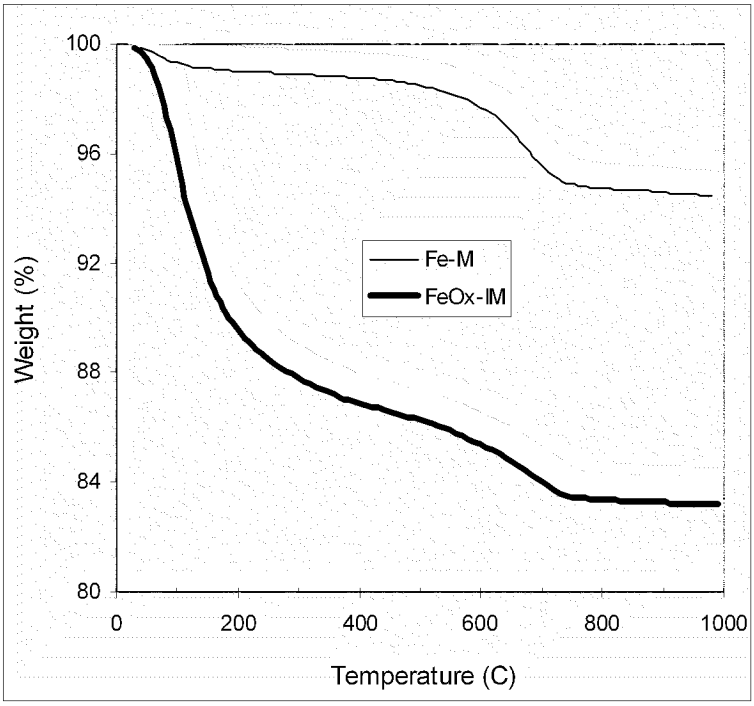

Figure 16: TG curves of Fe-M and FeOx-IM

Afterwards, the weight loss for FeOx-M becomes less pronounced and finally the structure seems to stabilize around 700 °C. The weight loss observed for FeOx-M in the 100-500 °C range is likely the result of the decomposition of iron (hydroxy)oxides which is supposed to start around 200 °C [89, 99]. That decomposition is apparently gradual up to at least 400 °C, as the DTG curve for FeOx-M shows no peak between 200 and 400 °C.

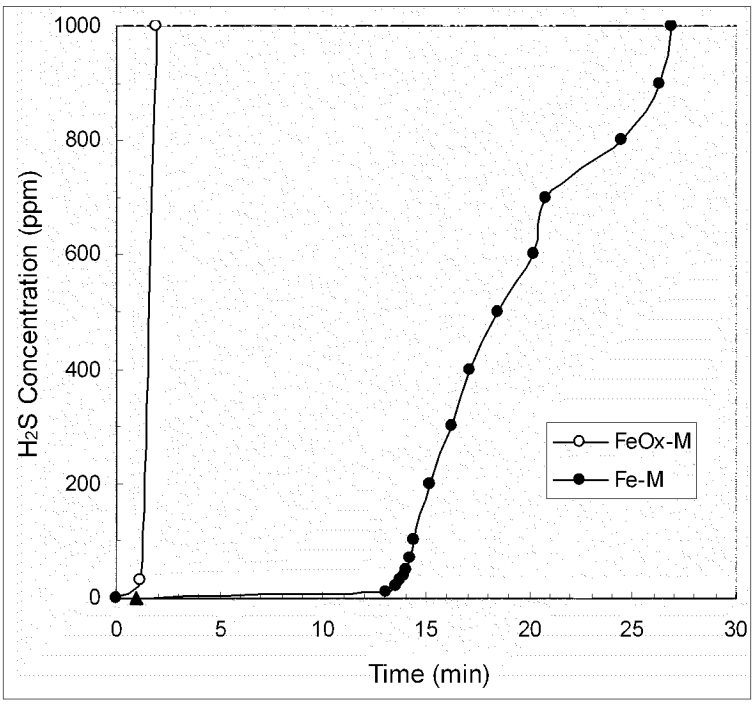

Figure 17: H_2S breakthrough curves for FeOx-M and Fe-M

Table 2: H_2S breakthrough capacities of FeOx-M and Fe-M

	Mass (g)	Breakthrough Time (min)	Breakthrough Capacity (mg g^{-1})
Fe-M	5.268	27.0	9.7
FeOx-M	5.875	2.0	0.6

Despite some significant porosity, FeOx-M turns out to be a poor adsorbent for H_2S, as the breakthrough occurs after a few minutes (Figure 17) and the calculated capacity (Table 2) is of only 0.63 mg of H_2S per g of material. On the other hand, Fe-M, even though less porous and particularly less microporous than FeOx-M, experiences a breakthrough after more than 25 min for a capacity of 9.65 mg/g, which is one order of magnitude higher than that for FeOx-M.

Elemental analysis results obtained by Inductively-Coupled Plasma (ICP) spectroscopy indicate that Fe-M and FeOx-M respectively contain 6.4 and 20.8% of iron. It can then be deduced that the determining factors for the adsorption of hydrogen sulfide in these materials are the chemical state of the iron, its location, and its degree of dispersion.

The SEM micrographs of Na-M, Fe-M, and FeOx-M (Figure 18) give some indication about the chemical state and the location of the iron. Na-M and Fe-M seem to exhibit similar surfaces, with smooth clay flakes devoid of small deposits. Thus, Fe^{3+}-exchange hardly affects the starting clay surface. Yet, based on its PSD, Fe-M should have iron deposits on its surface. It can then be deduced that the iron deposited on the surface of Fe-M is present under the form of small clusters, containing not more than a few iron atoms, which are in a highly dispersed state. In contrast, with FeOx-M, another phase is present on the surface of the clay flakes. That deposited phase, amorphous and dense, seems to be the result of the agglomeration of smaller particles. These particles could be the large iron clusters already mentioned during the PSD analysis of FeOx-M that would be at the origin of most of the mesoporosity in that material. These iron deposits in FeOx-M, that have previously been identified as limonite from XRD and FT-

IR analysis, are thus not as effective for the adsorption of hydrogen sulfide as Fe_2O_3 present in Fe-M.

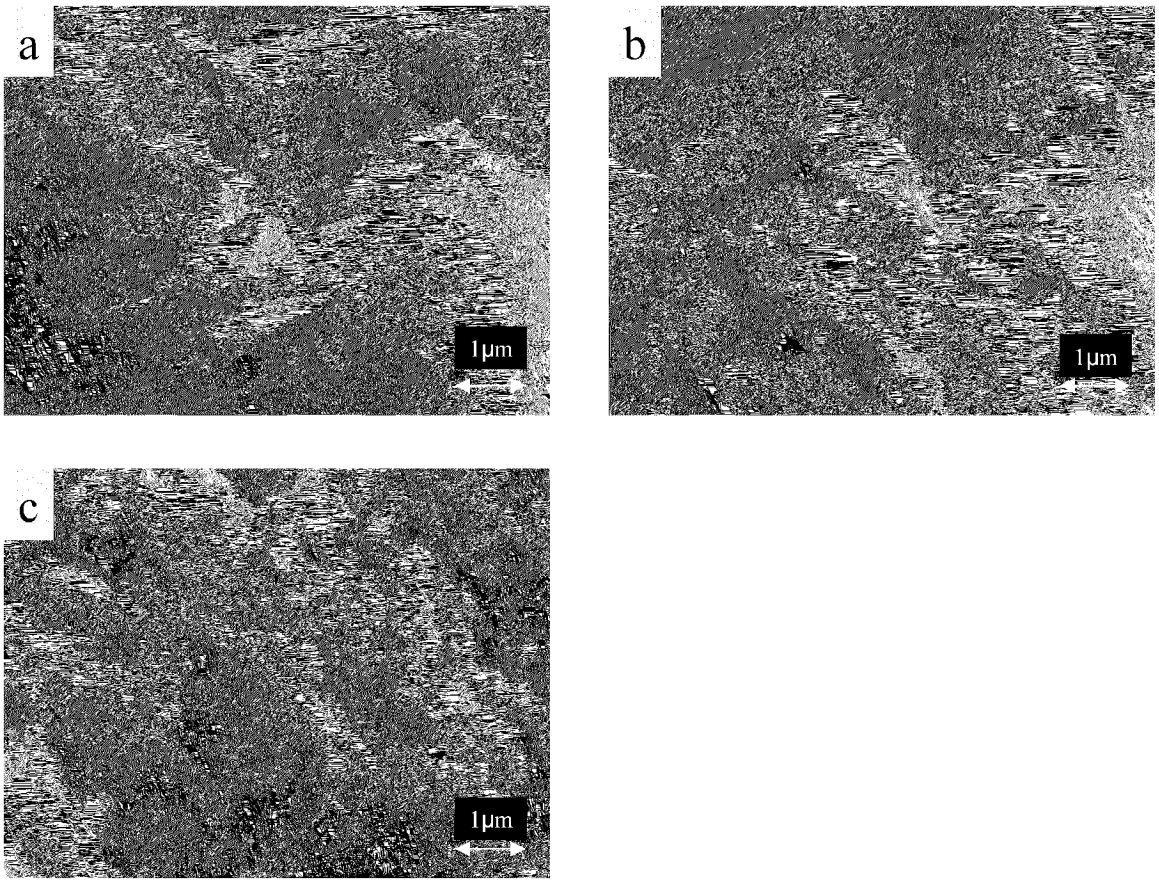

Figure 18: SEM pictures of Na-M (a), Fe-M (b), and FeOx-M (c)

It is thus proposed that in the case of Fe-M, Fe^{3+} reacts with H_2S to form sulfides. After some time in contact with air, the sulfides may eventually get oxidized into sulfates, as sulfides are unstable [109].

The mechanism of hydrogen sulfide adsorption on Fe-M could then be as follows:

$$Fe_2O_3 + 3\ H_2S \rightarrow Fe_2S_3 + 3\ H_2O \quad \textbf{(14)}$$

$$Fe_2S_3 + 6\ O_2 \rightarrow Fe_2(SO_4)_3 \quad \textbf{(15)}$$

With Fe-M, most of the iron present does not actually participate in the hydrogen sulfide immobilization process as it is located in the clay gallery where H_2S cannot penetrate due to a too small gallery opening. Thus, the only iron oxide that is active in Fe-M is the one located on the outer clay surface. As seen previously, FeOx-M should contain some accessible iron species between its layers, as this material exhibits some microporosity. But since the capacity of FeOx-M for hydrogen sulfide is so low, it is very likely that these smaller iron species are of the same nature as the iron deposits on the outer clay surface, only smaller.

Table 3: Structural parameters of the iron-modified clay samples before and after (/E) H_2S adsorption

	S_{BET} ($m^2\ g^{-1}$)	V_{DR} ($cm^3\ g^{-1}$)	V_t ($cm^3\ g^{-1}$)
Fe-M	63	0.025	0.124
Fe-M/E	65	0.026	0.124
FeOx-M	160	0.062	0.174
FeOx-M/E	161	0.057	0.175

N_2 adsorption carried out on the exhausted iron samples after H_2S breakthrough tests indicates that the porosity of these samples has practically not changed despite some hydrogen sulfide fixation on them (Table 3). That may be the result of even adsorption of hydrogen sulfide and of even formation of adsorption products on the materials surface. Indeed, for both materials, adsorption mainly occurs on the outer clay surface. That surface is relatively large and its sites are very large compared to the species either

adsorbed or formed there (H_2S has a diameter of 3.2 Å), so it is unlikely that so small amounts of hydrogen sulfide adsorbed could significantly alter the porosities of those materials. FeOx-M does exhibit a slight micropore volume decrease though. As already seen, only that sample can potentially adsorb hydrogen sulfide in its micropores, and since those micropores are so small and have such a small volume, even minute amounts of adsorbate in them can cause a decrease in their volume.

4.2. Pillared Interlayered Clays Loaded with Metal

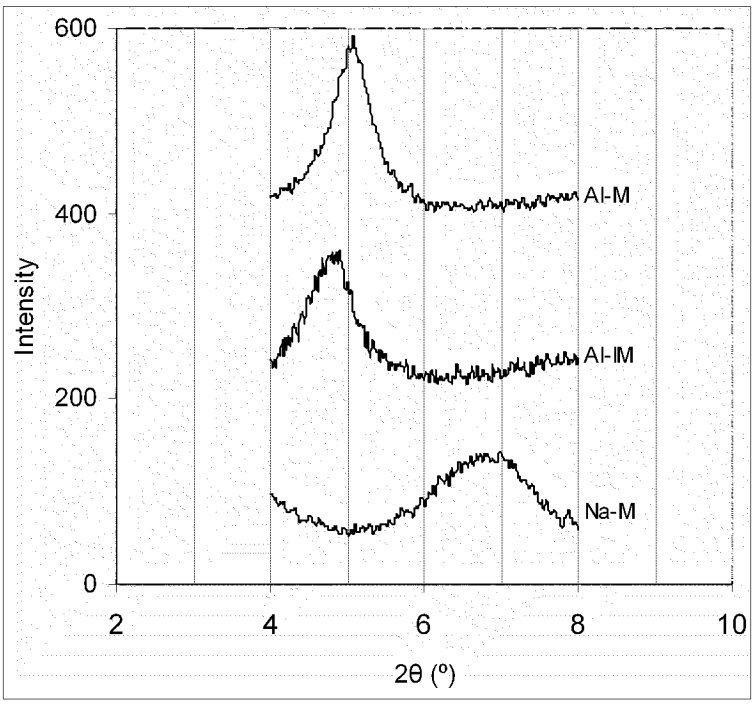

Figure 19: XRD of Na-M, Al-IM, and Al-M

Na-M montmorillonite was pillared using the Keggin ion $[Al_{13}O_4(OH)_{24}(H_2O)_{12}]^{7+}$ as the intercalating species, which gave after calcination an

Al_2O_3-pillared clay, Al-M. Na-M intercalated with the Keggin ion but not yet calcined is referred as Al-IM. Al-M was further loaded with the metal cations Fe^{3+}, Zn^{2+}, and Cu^{2+}, yielding respectively FeAl-M, ZnAl-M, and CuAl-M. Intercalation of the Keggin ion results into changes in the interlayer spacing, as the XRD patterns suggest (Figure 19). Thus, Al-IM has a diffraction peak at $2\theta = 4.90^{\circ}$, which corresponds to an interlayer spacing of 8.4 Å, a 5.3 Å increase from the original spacing with Na-M. The interlayer spacing for Al-IM actually exactly matches the diameter of the Keggin ion [10, 12]. Through calcination at 400 °C, the spacing decreases to 7.8 Å with $2\theta = 5.08^{\circ}$ for Al-M. Such a decrease in interlayer distance can be explained by the dehydration and dehydroxylation of the Keggin ion upon calcination, a process that leads to Al_2O_3 pillars. It is worth to mention that the distances found for Na-M and Al-M agree with those from Hutson *et al.* [14]. Al-pillaring thus increased the interlayer distance in the original clay by a factor of 2.5. This should result in some significant porosity, especially microporosity.

Dramatic changes to the pillared structure seem to occur when Al-M is loaded with iron (Figure 20). Indeed, the peak at $2\theta = 5.08^{\circ}$ is no longer present with FeAl-M, and XRD diffraction for that sample does not reveal any other peak. As with Fe-M, that absence of order in FeAl-M could be due to some interaction of iron with the clay layers that would weaken them and make the clay structure lose its order upon calcination. That phenomenon could be coupled with reaction of iron with the hydrated alumina pillars, as iron has been shown to interact with the Keggin ion [79]. That would decrease the thermal stability of the pillars, and FeAl-M structure would consequently degrade at the calcination temperature of 400 °C.

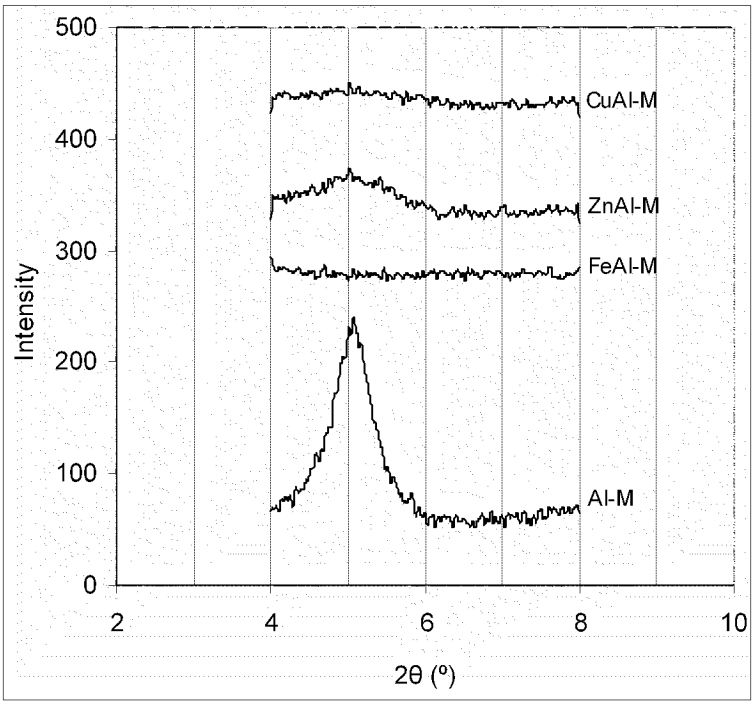

Figure 20: XRD of Al-M, FeAl-M, ZnAl-M, and CuAl-M

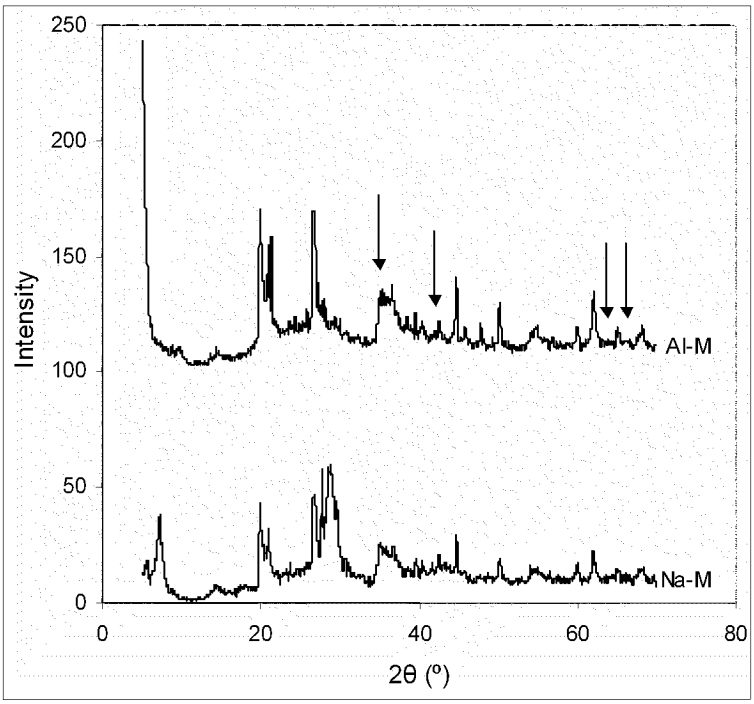

Figure 21: Extensive XRD of Na-M and Al-M

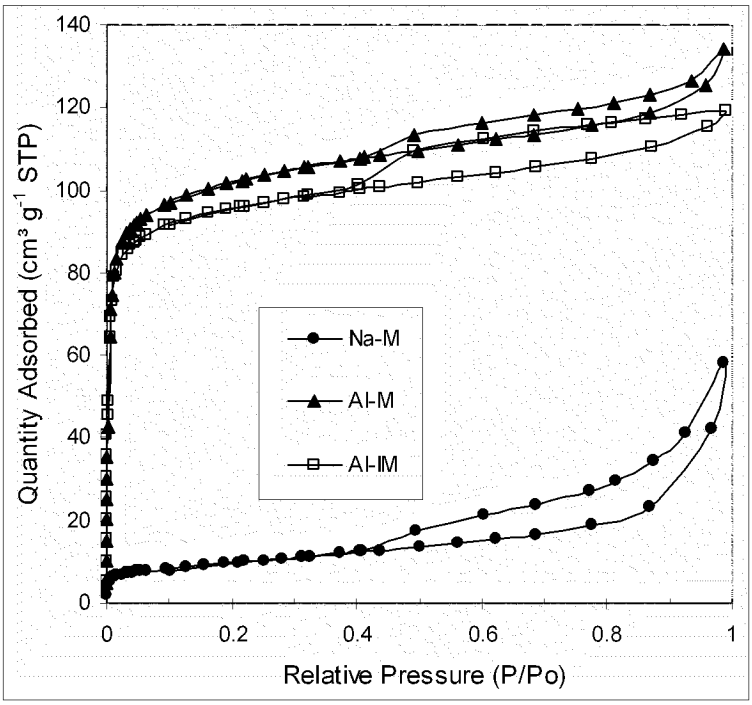

Figure 22: N_2 adsorption-desorption isotherms of Na-M, Al-IM, and Al-M

Such a collapse, even partial, of the pillared structure should reflect a loss of porosity in the material. Unlike FeAl-M, ZnAl-M and CuAl-M exhibit the same peak as Al-M at $2\theta = 5.08^{\circ}$, even though the intensity is smaller than that for Al-M. As a consequence, despite loading with zinc and copper, the ordered structure and the interlayer spacing inherited from Al-pillaring has been retained, so ZnAl-M and CuAl-M should still possess some significant microporosity.

The extensive XRD of Al-M and Na-M (Figure 21) confirms the presence of Al_2O_3 as a result of pillaring, with peaks at 35.5°, 42.4°, 64.9°, and 66.7° that are present with Al-M and not with Na-M.

The evolution of porosity upon modification with the Keggin ion is illustrated by the N_2 adsorption-desorption isotherms on the different samples (Figure 22). Al-IM and Al-M both have a type I adsorption isotherm, which is indicative of microporous

materials [8, 59, 110, 111]. They also have a type H_4 hysteresis loop due to mesopores that are open slit-shaped capillaries. Their high N_2 intakes at low pressure show that Al-IM and Al-M do possess some significant microporosity as a result of Keggin ion intercalation.

The total porosity and especially the microporosity of Al-M is slightly superior to the ones for Al-IM, which seems logical since calcination of Al-IM to Al-M should free some space between the intercalated species [6], thus generating additional porosity. That porosity increase is only partially compensated by the porosity decrease linked to the shortening of the interlayer spacing as indicated from XRD.

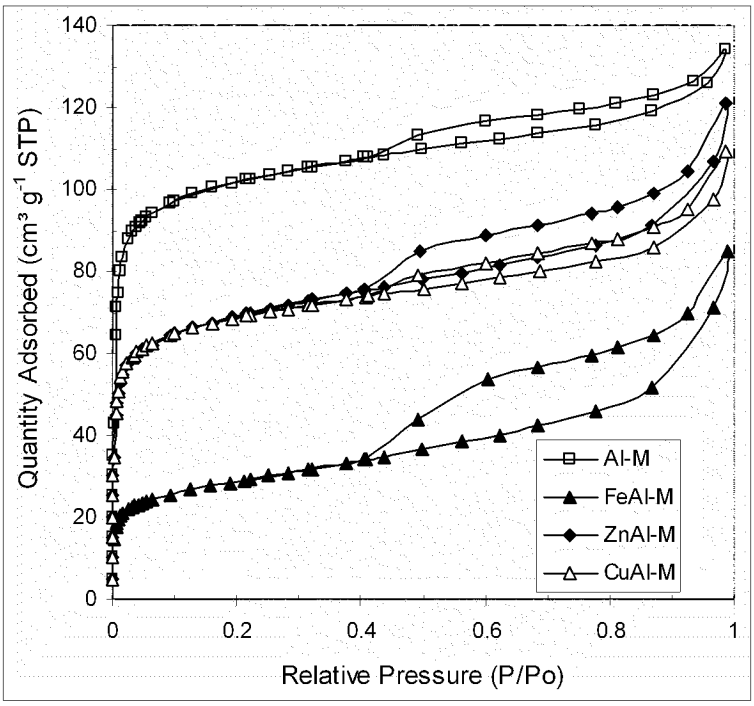

Figure 23: N_2 adsorption-desorption isotherms of Al-M, FeAl-M, ZnAl-M, and CuAl-M

Figure 23 allows assessing the effects of metal cation loading on the porosity of Al-M. Except for the uptakes at lower pressure, the adsorption isotherms for Al-M, FeAl-M, ZnAl-M, and CuAl-M have similar shapes and remain parallel from P/Po ~ 0.1 to 1, which means that they have comparable mesoporosities and macroporosities while their microporosities differ. It can then be said that loading Al-M with metal cations practically only causes a decrease in microporosity. This suggests that the loaded metal cations are mostly located in the micropores of Al-M, between the clay layers. The microporosity loss is not the same for all the samples though: while the microporosity loss with Zn-loading and Cu-loading is rather limited, it is much more dramatic with Fe-loading. ZnAl-M and CuAl-M should still then possess some significant microporosity. Indeed, their N_2 uptakes at low pressure are relatively high. The uptakes also turn out to be equivalent for both materials, so their micropore volumes should be close. On the other hand, the large microporosity loss in FeAl-M further confirms the previous hypothesis according to which the presence of large quantities of iron damaged the layered structure of the clay and some of the alumina pillars, thus considerably reducing the porosity. But the microporosity change from Al-M to FeAl-M is too drastic to be solely explained by this phenomenon. Then, it is also possible that the quantity of loaded iron is so high that a large fraction of it mainly fills the micropores remaining after structural collapse.

The PSD of Al-IM (Figure 24) indicates that mainly microporosity is generated upon exchanging Na-M with the Keggin ion, thus confirming that this pillaring species mostly migrate between the clay layers without significantly depositing on the outer clay surface [112]. Al-IM has two peaks present in the micropore region, one at 6.6 Å, the other one at 13.1 Å. Following calcination, Al-M has peaks at the same positions as for

Al-M, but their intensities differ: with Al-M, while the one at 6.6 Å is lower than that for Al-IM, the other one at 13.1 Å is higher.

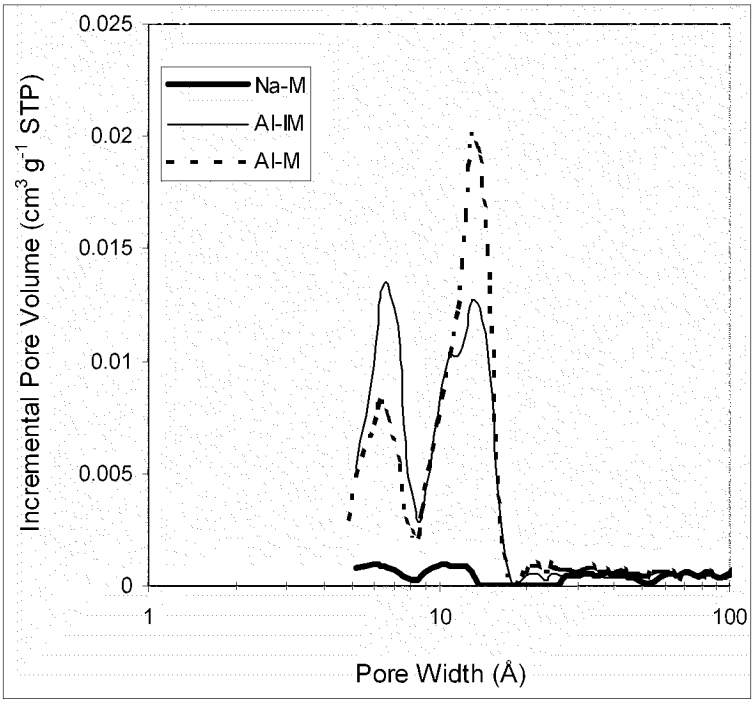

Figure 24: Pore Size Distributions of Na-M, Al-IM, and Al-M

Calcination of Al-IM into Al-M should result in a larger pore volume in the clay gallery, as the dehydration and dehydroxylation of the Keggin ion into alumina generates additional space between the pillars, so it can be deduced that the peak at 13.1 Å is a direct result of the Keggin ion intercalation. The peak at 6.6 Å then represents micropores that are not directly related to the Keggin ion intercalation. The origin of these small micropores probably comes from the formation of voids between clay crystallites, as the clay platelets aggregate during the drying of Al-IM [10]. It is worth mentioning that the modified DFT model that we used for PSDs seems to lack accuracy for the analysis of

PILC materials. Indeed, while XRD gave an interlayer spacing of 7.8 Å for Al-M, the PSD suggested a micropore width of 13.1 Å. As a consequence, the data provided by the use of that DFT model on PILCs cannot be considered as absolute, unlike XRD data. Nevertheless, PSDs determined by that DFT model should reveal patterns and trends in porosity changes.

From the PSD of FeAl-M (Figure 25), it can be seen that FeAl-M does possess some microporosity, with a peak at 12.4 Å. That microporosity seems to be inherited from the intercalation of the Keggin ion that gave the peak at 13.1 Å for Al-M. The peak at 12.4 Å for FeAl-M is very low in intensity, which further confirms that Fe^{3+} has considerably damaged the micropores present in Al-M and almost completely filled the remaining ones.

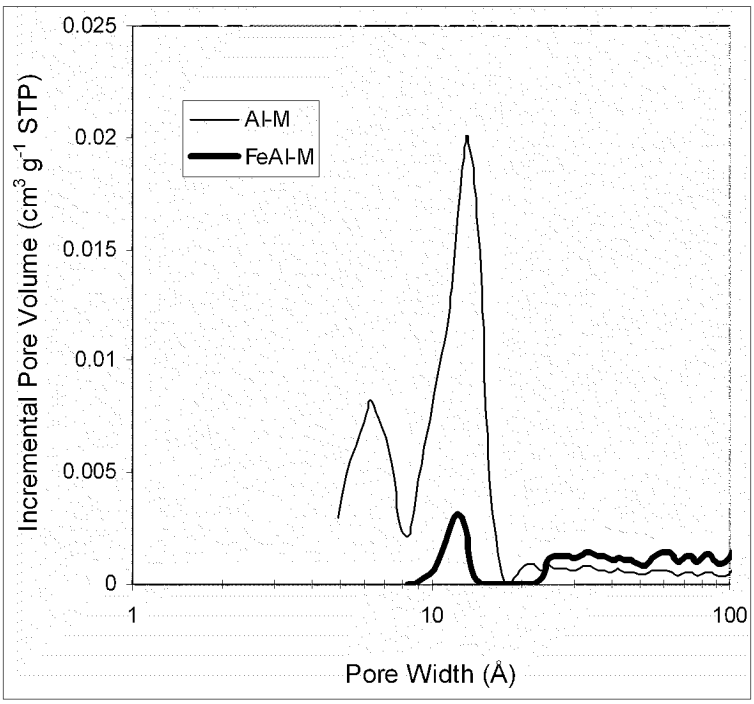

Figure 25: Pore Size Distributions of Al-M and FeAl-M

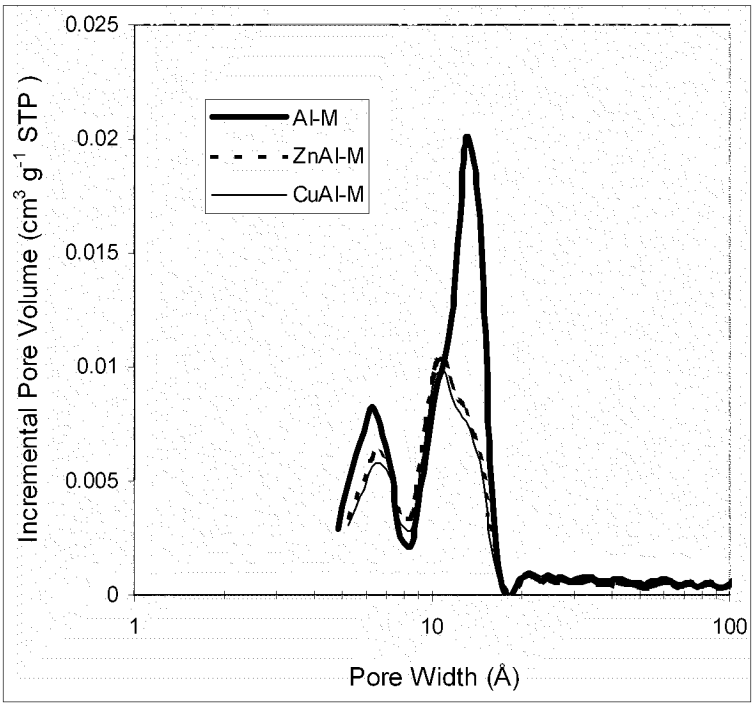

Figure 26: Pore Size Distributions of Al-M, ZnAl-M, and CuAl-M

The effect of iron on the smaller micropores at 6.6 Å from Al-M was even more dramatic as those pores totally disappeared. No such changes occur with ZnAl-M and CuAl-M (Figure 26). Those two PILCs have micropore peaks at approximately the same positions as with Al-M. These peaks are slightly smaller than those for Al-M. This indicates that zinc and copper are for the most part located inside the micropores generated in Al-M and do not alter the structural integrity of the PILC.

The calculated structural parameters (Table 4) confirm that Al-M is mainly a microporous material: micropores represent more than 80% of the total pore volume. These parameters also give a measure of the effects of iron loading: iron causes a decrease in the micropore volume of more than 80% as a result of destruction or filling. On the other hand, ZnAl-M and CuAl-M, with equivalent structural parameters, have micropore volumes that are only 30% smaller than those for Al-M.

Table 4: Structural parameters of the Al-pillared clay samples

	S_{BET} ($m^2 g^{-1}$)	V_{DR} ($cm^3 g^{-1}$)	V_t ($cm^3 g^{-1}$)
Al-M	323	0.167	0.206
FeAl-M	75	0.030	0.127
ZnAl-M	227	0.122	0.160
CuAl-M	219	0.115	0.168

Table 5: Metal Contents of the Loaded PILCs

	Fraction of Metal (%)	Quantity of Metal (mmol g^{-1})
FeAl-M	9.83	1.70
ZnAl-M	4.03	0.61
CuAl-M	7.72	1.10

The calculated structural parameters (Table 4) confirm that Al-M is mainly a microporous material: micropores represent more than 80% of the total pore volume. These parameters also give a measure of the effects of iron loading: iron causes a decrease in the micropore volume of more than 80% as a result of destruction or filling. On the other hand, ZnAl-M and CuAl-M, with equivalent structural parameters, have micropore volumes that are only 30% smaller than those for Al-M.

Metal contents of the loaded PILCs determined by ICP are reported in Table 5. It can be seen that the metal content of ZnAl-M is almost half the one for CuAl-M. Since as previously suggested ZnAl-M and CuAl-M have similar amounts of metal cations in their micropores, then about half of the loaded copper in CuAl-M is located in the mesopores and macropores. That copper present in larger pores is likely evenly spread into them, which would explain why only the micropore volume decreases upon copper loading.

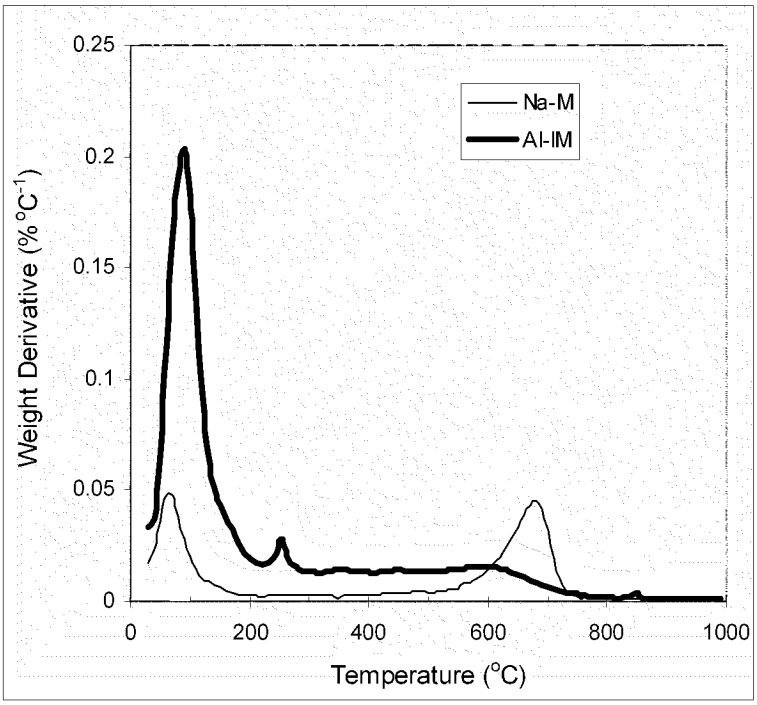

Figure 27: DTG curves of Na-M and Al-IM

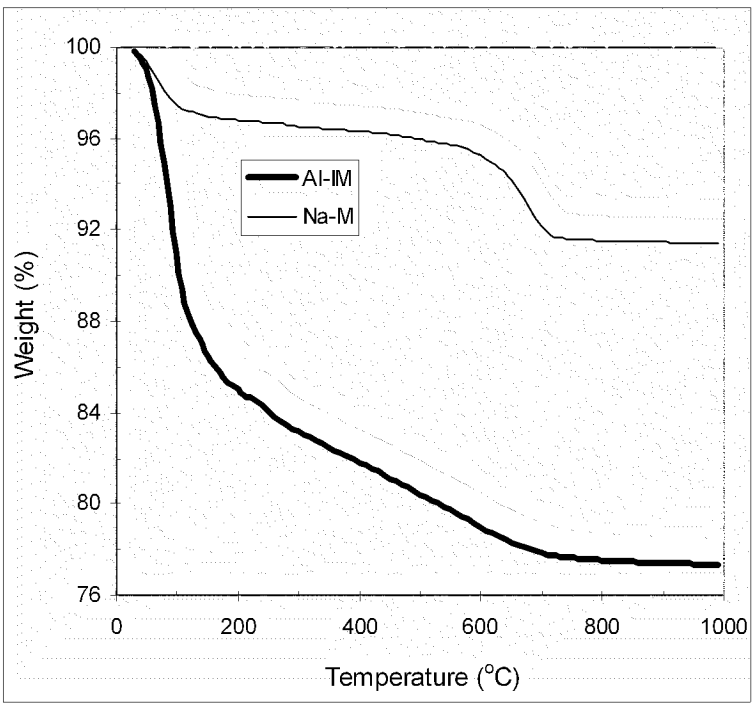

Figure 28: TG curves of Na-M and Al-IM

On the other hand, the iron content in FeAl-M is so high that its micropores are clogged with iron. Furthermore, it is very likely that larger iron clusters are also present as deposits on the outer clay surface as observed previously.

Al-IM, the clay intercalated with Keggin ion, shows a peak at 250 °C on its DTG curve (Figure 27) that is not present with the starting clay, Na-M. This peak is likely due to the removal of structural water from the Keggin ion [89, 110, 111], a phenomenon that is supposed to start at around 200 °C [89, 113]. At higher temperatures, the DTG curve of Al-IM does not show any other peak, which indicates that there is no particular temperature at which destruction of the Al pillars occurs. Instead, their dehydration and dehydroxylation happen gradually and even overlap with the dehydroxylation of the clay layers. Indeed, dehydroxylation of the Keggin ion when intercalated in a montmorillonite clay should happen between 425 and 600 °C, along with the dehydroxylation of the clay layers [79]. The TG curve of Al-IM (Figure 28) indicates that the weight loss due to water removal from between the layers consists of about 15% and that a continuous weight loss is observed with almost a constant slope up to 650 °C when the clay layers lose their hydroxyl groups.

Despite its high microporosity, Al-M has a negligible H_2S adsorption capacity of 0.57 mg/g (Figure 29 and Table 6). This shows that microporosity cannot by itself be responsible for the adsorption of H_2S and that the presence of active species is required for this process. Thus, despite a much lower microporosity than Al-M, FeAl-M fixes about 30 times more H_2S than Al-M. The affinity of iron for H_2S was expected, based on the results obtained with Fe-M.

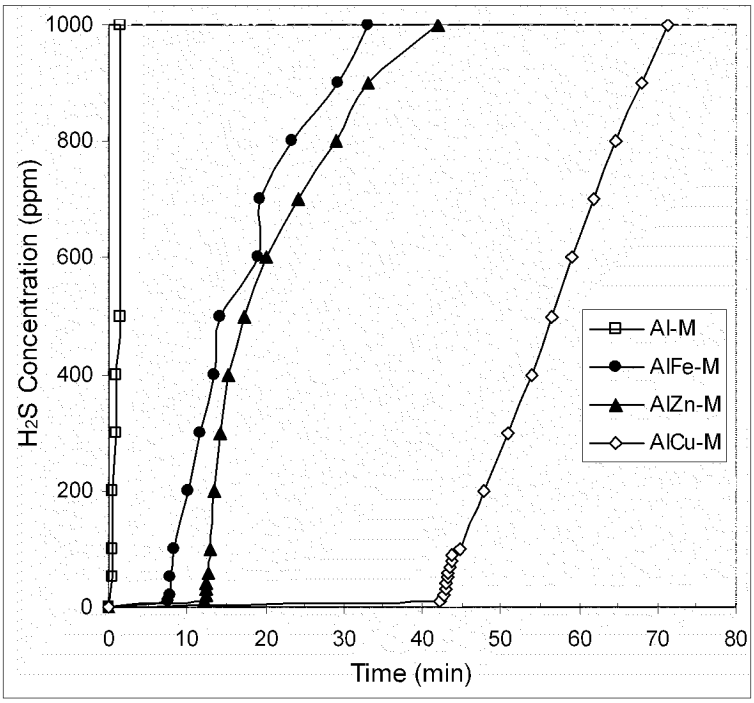

Figure 29: H_2S breakthrough curves of Al-M, FeAl-M, ZnAl-M, and CuAl-M

Table 6: H_2S breakthrough capacities of Al-M, FeAl-M, ZnAl-M, and CuAl-M

	Mass (g)	Breakthrough Time (min)	Breakthrough Capacity (mg g^{-1})	Quantity of H_2S Adsorbed (mmol g^{-1})
Al-M	5.295	1.5	0.6	0.02
FeAl-M	3.286	33.0	17.6	0.52
ZnAl-M	3.480	42.0	20.9	0.61
CuAl-M	2.834	71.5	48.8	1.43

Compared to Fe-M, FeAl-M has a capacity that is almost twice as large as the one for Fe-M. Beforehand, Fe-M and FeAl-M contain the same iron species since they were loaded under similar experimental conditions. These two samples also exhibit similar porosities. The main difference between them mainly lies in their iron contents, with FeAl-M having about 50% more iron than Fe-M (9.83% vs. 6.4%). But that difference in

iron content cannot solely by itself explain the difference in the capacity between these two samples. Containing the same active species, Fe-M and FeAl-M should then differ on the location and the accessibility of these species. Indeed, in Fe-M, most of the iron is situated between the clay layers as a result of cation exchange. Thus, that iron cannot play any role in the adsorption process, as the interlayer spacing is too small to allow H_2S molecules to enter the clay gallery. The only active iron in the case of Fe-M is the one adsorbed on the outer clay surface, which only represents a small fraction of the total iron present. On the other hand, FeAl-M has its iron mainly located in its micropores and its interlayer spacing should be wide enough for interaction of that iron with H_2S. But as these micropores are almost completely filled with iron, only a fraction of them, those located on the surface, are active.

While ZnAl-M has a H_2S removal capacity that is slightly better than the one for FeAl-M, CuAl-M adsorbed more than twice as much H_2S than the other two samples. Analysis of the slope evolution on the breakthrough curves of the metal-loaded PILCs gives some indication about the mechanism through which H_2S adsorption occurs on these materials. For CuAl-M, once breakthrough happens, the slope remains constant, suggesting a unique and consistent process. With FeAl-M and ZnAl-M, after a steep slope following breakthrough, the rate at which the concentration of H_2S increases fluctuates, alternatively increasing and decreasing, thus being indicative of a more complex immobilization mechanism for H_2S. Comparison of the quantity of metal in the samples (Table 5) to the quantity of adsorbed H_2S molecules (Table 6) gives a better understanding on the mechanisms involved. In the case of ZnAl-M, the two quantities are exactly equal, so a direct reaction between zinc and H_2S takes place, with all the loaded

zinc being accessible to the adsorbate. For CuAl-M, the amount of copper is inferior to the amount of H_2S molecules adsorbed, which shows the catalytic effect of copper for H_2S oxidation. The number of moles of iron is more than 3 times the one for H_2S molecules. In the case of FeAl-M, the metal loading level is too high. Most of the iron in FeAl-M does not participate in the H_2S adsorption level and even inhibits that process by damaging the pillared structure and by clogging the remaining microporous adsorption sites. Another reason for the low efficiency of iron in FeAl-M for H_2S fixation could also be the tendency of Fe^{3+} to hydrolyze and to deposit on the outer clay surface as large clusters [63, 114], which further reduces the availability of iron.

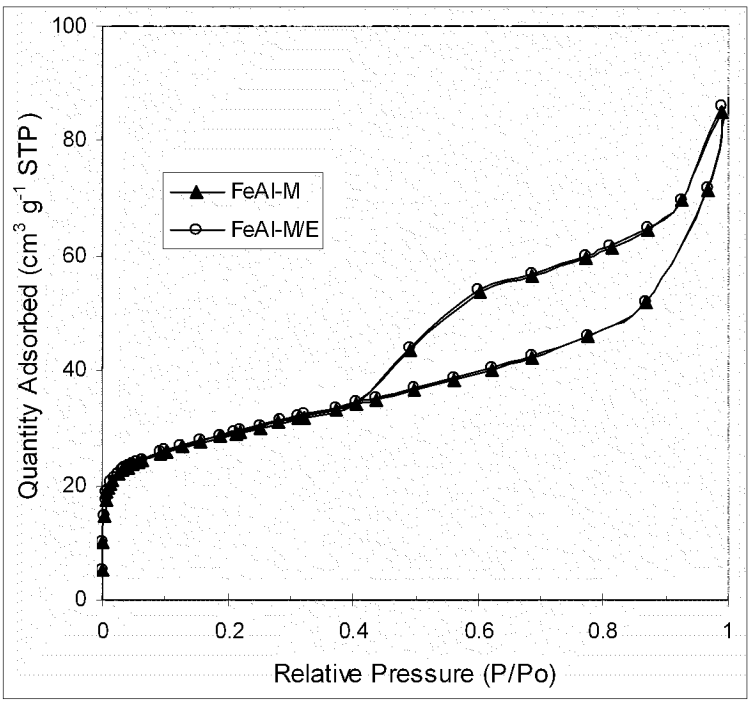

Figure 30: N_2 adsorption-desorption isotherms of FeAl-M before and after (/E) H_2S adsorption

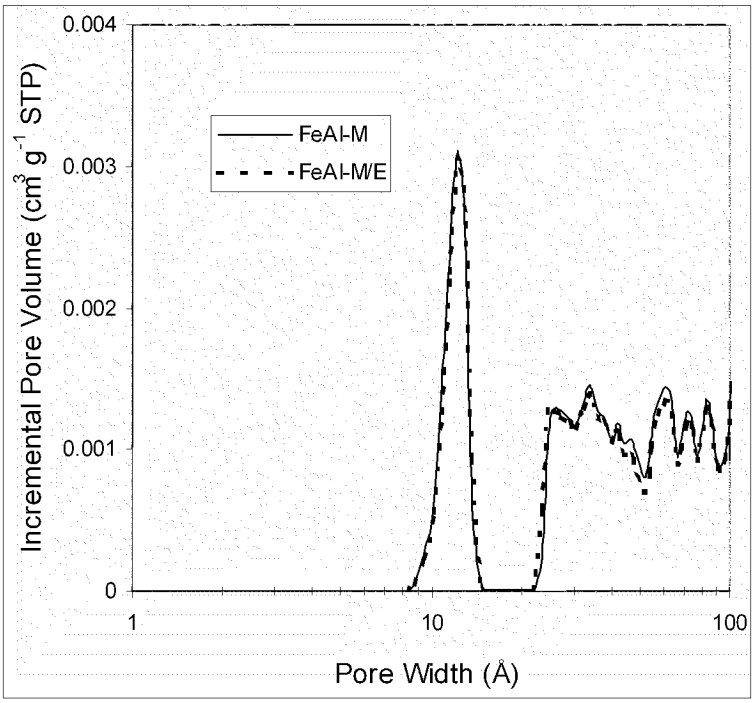

Figure 31: PSD of FeAl-M before and after (/E) H_2S adsorption

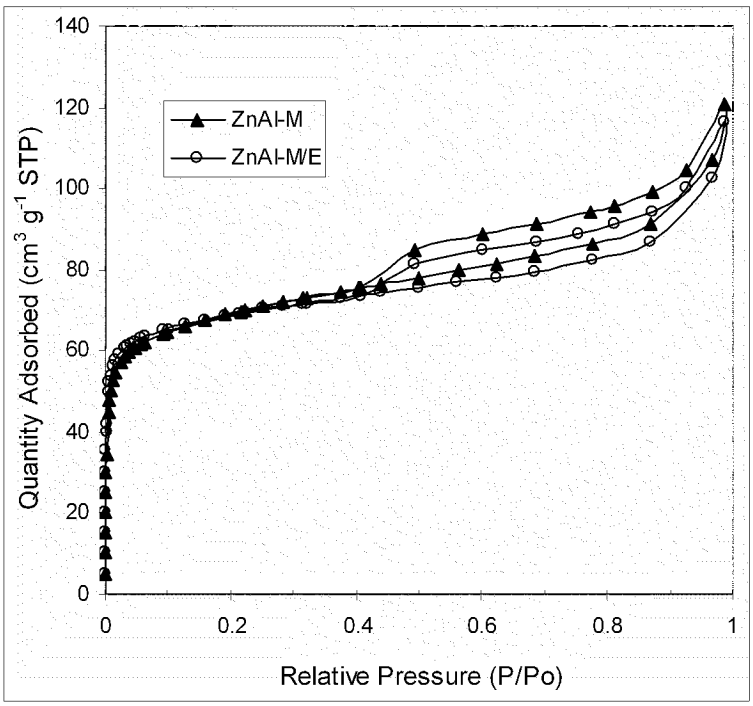

Figure 32: N_2 adsorption-desorption isotherms of ZnAl-M before and after (/E) H_2S adsorption

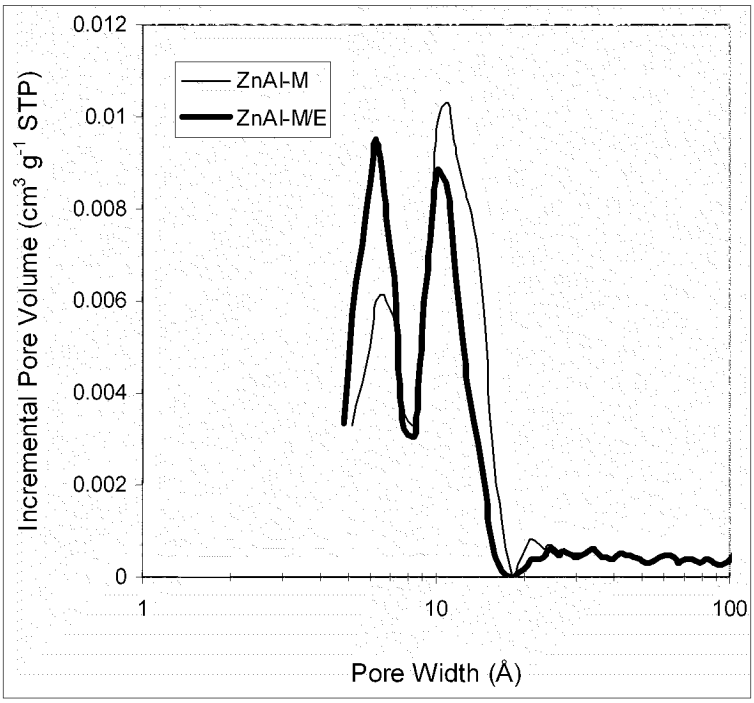

Figure 33: PSD of ZnAl-M before and after (/E) H_2S adsorption

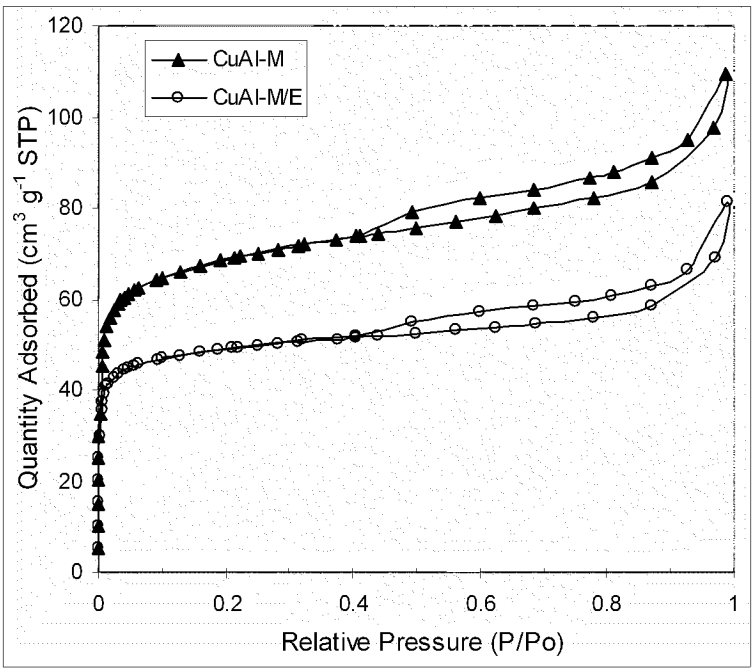

Figure 34: N_2 adsorption-desorption isotherms of CuAl-M before and after (/E) H_2S adsorption

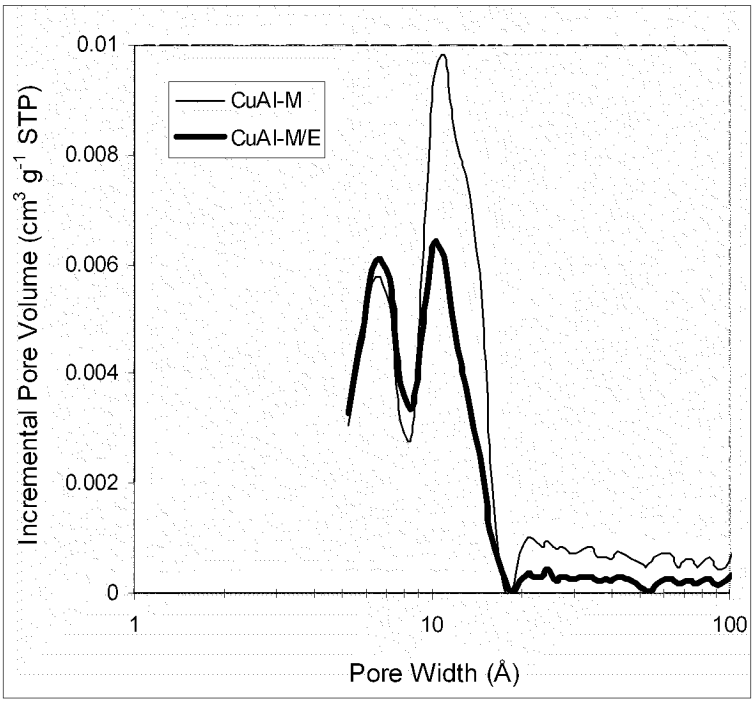

Figure 35: PSD of CuAl-M before and after (/E) H_2S adsorption

Table 7: Structural parameters of the metal-loaded Al-pillared clay samples before and after (/E) H_2S adsorption

	S_{BET} ($m^2\ g^{-1}$)	V_{DR} ($cm^3\ g^{-1}$)	V_t ($cm^3\ g^{-1}$)
FeAl-M	75	0.030	0.127
FeAl-M/E	75	0.032	0.125
ZnAl-M	227	0.122	0.160
ZnAl-M/E	196	0.103	0.145
CuAl-M	219	0.115	0.168
CuAl-M/E	154	0.083	0.124

Despite adsorption of significant amounts of H_2S, the porosity of FeAl-M is not affected: its adsorption isotherm (Figure 30), PSD (Figure 31), and structural parameters (Table 7) remain the same. The absence of porosity change in FeAl-M may be due to the

oxidation (after its adsorption) of H_2S into weakly adsorbed SO_2, which may happen in parallel with the reduction of Fe^{3+} into Fe^{2+}. That SO_2 would then be desorbed at room temperature or during the outgassing preceding N_2 adsorption. Indeed, the evolution of SO_2 during H_2S adsorption was observed as the former gas was detected during the breakthrough tests. For example, for FeAl-M, when [H_2S] in the effluent stream was of 350 ppm, [SO_2] was of 1 ppm.

On the contrary for ZnAl-M, the porosity decreases following H_2S adsorption, as can be seen from its adsorption-desorption isotherm (Figure 32), its PSD (Figure 33), and structural parameters (Table 7). This indicates that H_2S adsorption on ZnAl-M resulted in the deposition of reaction products in its porous system. When comparing the isotherms for ZnAl-M and for ZnAl-M/E, it can be seen that they mainly differ in the P/Po range between 0.3 and 0.4, with the curve for ZnAl-M/E situated below that for ZnAl-M. Both curves remain parallel and follow the same pattern outside this pressure region. This indicates that ZnAl-M and ZnAl-M/E have similar mesoporosities and macroporosities, and that differences in porosity remain limited to the larger micropores-smaller mesopores that are responsible for adsorption when $0.3 \leq P/Po \leq 0.4$. This is confirmed when comparing the PSDs of those two samples: the porosity decrease is restricted to the 10-25 Å region. From the analysis of the structural parameters, the micropore volume and total pore volume decreases are equivalent, thus confirming that adsorption mostly affects the micropores. The porosity changes in CuAl-M are even more dramatic (Figures 34 and 35, Table 7), which was expected based its performance as a H_2S adsorbent. The difference in isotherm is particularly striking in the lower pressure region, which means that H_2S adsorption on CuAl-M mainly affects the micropores. But the PSDs show that

the mesopores are affected as well. The micropore volume decrease in CuAl-M is more pronounced than that for ZnAl-M. When comparing the actual micropore and total pore volume decreases in CuAl-M, it is found that more than 70% of the total porosity loss happens in the micropores. In the case of ZnAl-M, zinc is concentrated in the larger micropores-smaller mesopores where H_2S adsorbs, while for CuAl-M, copper is distributed in pores of all kinds and adsorption takes place in all the pores that are larger than 10 Å. H_2S adsorption in CuAl-M nevertheless appears to be more extensive in the micropores, as this process must be enhanced by the forces exerted by the micropore walls on H_2S molecules.

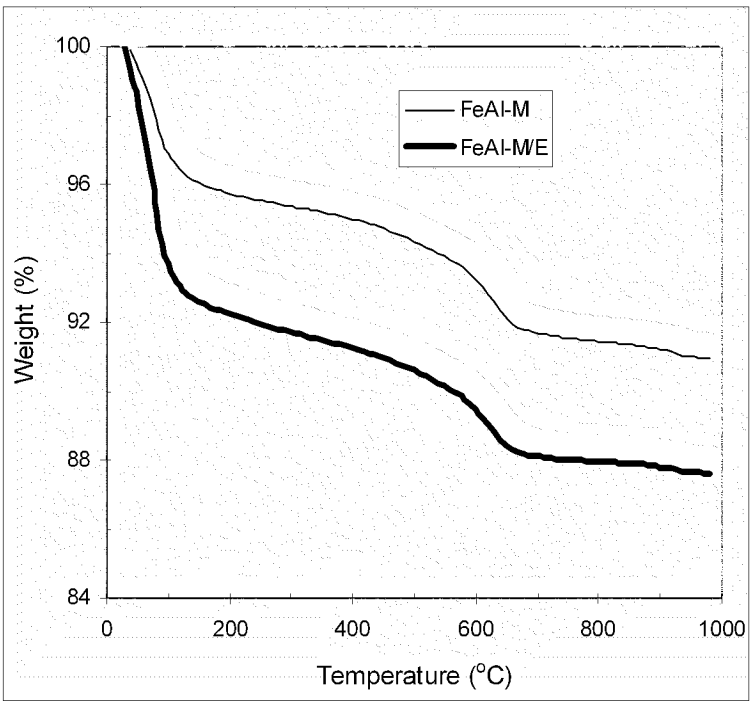

Figure 36: TG curves of FeAl-M(/E)

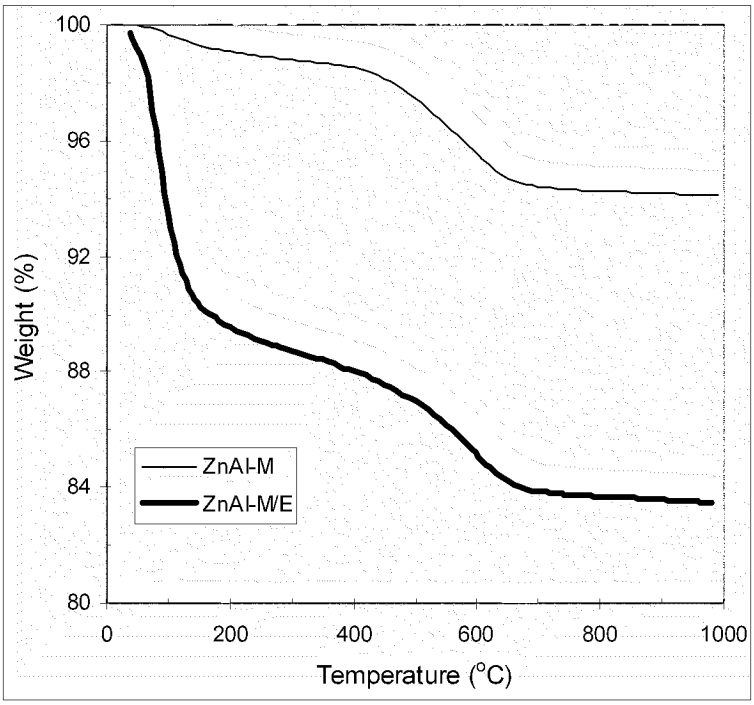

Figure 37: TG curves of ZnAl-M(/E)

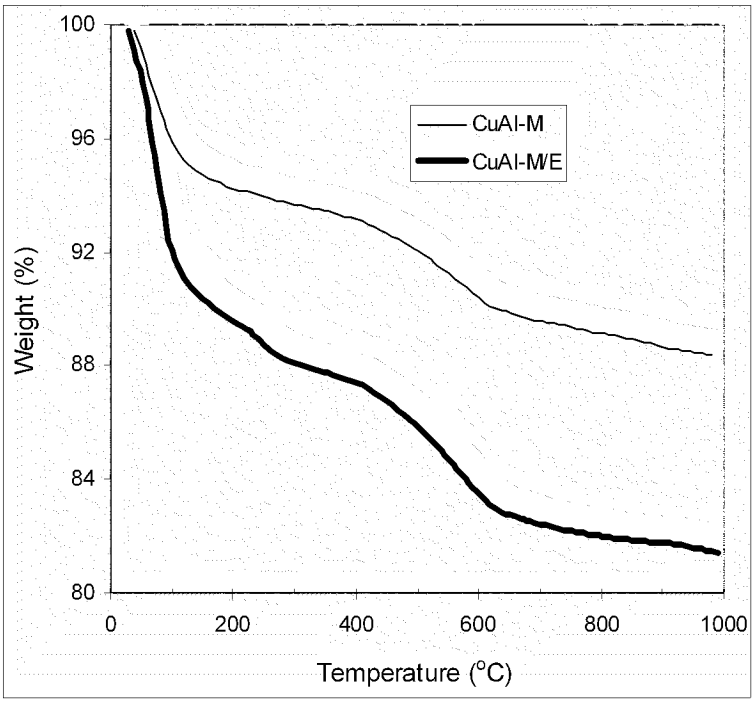

Figure 38: TG curves of CuAl-M(/E)

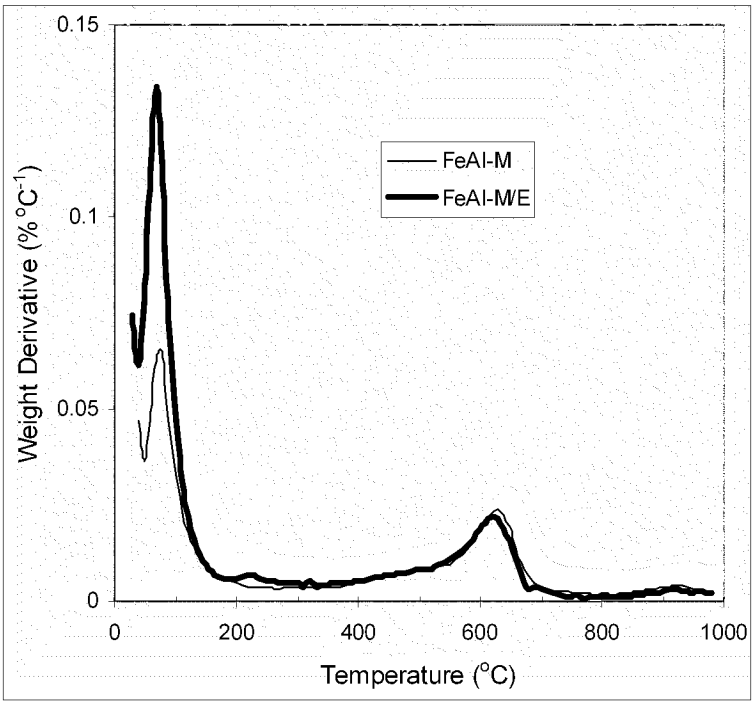

Figure 39: DTG curves of FeAl-M(/E)

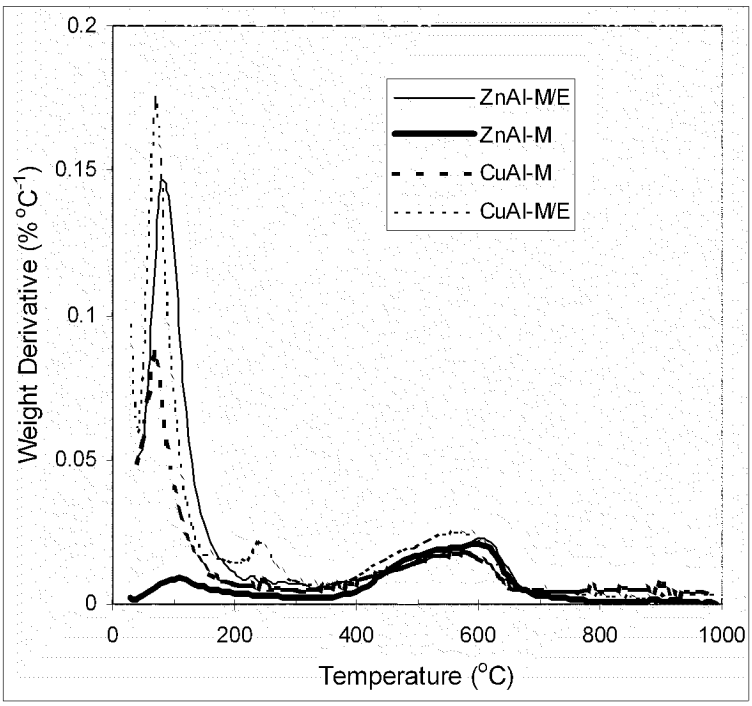

Figure 40: DTG curves of ZnAl-M and CuAl-M(/E)

From TG analysis (Figures 36-38), it can be seen that all the metal loaded PILCs contain reaction products resulting from H_2S adsorption as the weight loss is always greater with the exhausted samples. Besides, the total weight loss at 1,000 ^oC is commensurate with the samples' capacity. Thus, the total weight losses for FeAl-M/E, ZnAl-M/E, and CuAl-M/E are respectively 12.41, 16.52, and 18.57%.

Unlike Al-IM, the metal loaded PILCs exhibit a peak due to the dehydroxylation of the clay layers on their DTG curves (Figures 39 and 40). That peak is located at 580, 590, and 630 ^oC for CuAl-M, ZnAl-M, and FeAl-M, respectively. Those temperatures are lower than those found for Na-M (680 ^oC). It then appears that metal loading entails a loss in thermal stability. That loss of stability may be due to some interaction of the metal cations with the clay layers, which renders them less resistant to high temperatures. This decrease in thermal stability is more pronounced with ZnAl-M and CuAl-M that start to see their layers collapsing at 400 ^oC, instead of 500 ^oC as observed for Na-M. It is possible that this phenomenon is accompanied by the dehydroxylation of the alumina pillars. Indeed, as mentioned previously, metal cations can interact with the pillars, which would disrupt their stability [79].

The DTG curve of FeAl-M/E features a peak at 220 ^oC that had been identified in a previous study as SO_2 [114], which confirms the formation of SO_2 during H_2S adsorption for FeAl-M. Furthermore, the curve for FeAl-M/E is located slightly below the one for FeAl-M in the 250 and 450 ^oC range, which could be indicative of the presence of elemental sulfur on FeAl-M/E. Indeed, elemental sulfur is expected to form during H_2S adsorption on iron oxide [115]. Compared to the original samples, ZnAl-M/E

and CuAl-M/E show on their DTG curves some new features in the 200-700 °C region. But while the DTG curve for ZnAl-M/E does not really have any distinct peak in that temperature range, the one for CuAl-M/E features a peak centered at 240 °C.

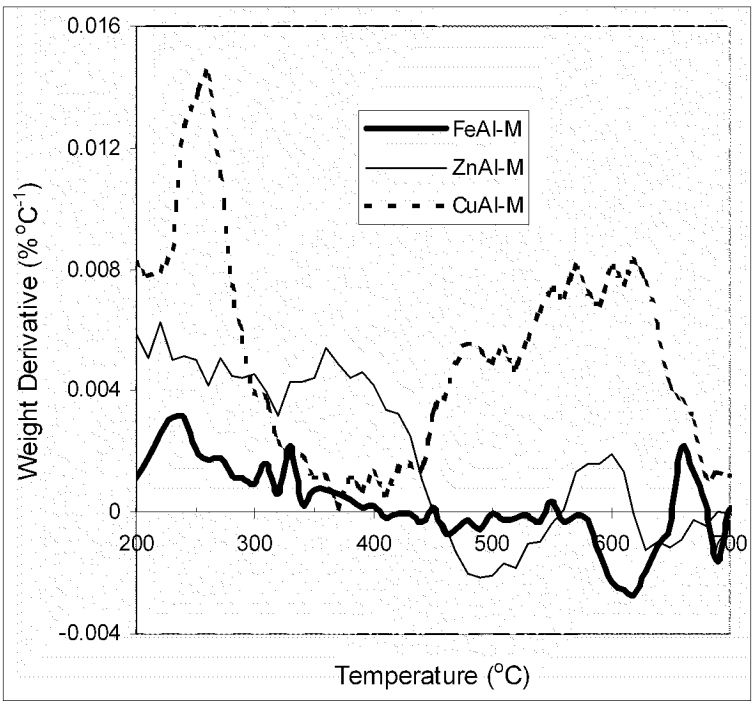

Figure 41: DTG differences of FeAl-M, ZnAl-M, and CuAl-M

Table 8: pH values of the samples before and after H_2S adsorption

	Initial pH	pH after H_2S Adsorption
Na-M	8.59	-
Al-M	7.18	-
FeAl-M	5.59	5.59
ZnAl-M	6.09	6.06
CuAl-M	5.35	5.05

To reduce ambiguity, the DTG differences between the exhausted samples and the original ones have been plotted (Figure 41). While FeAl-M shows a practically flat curve, ZnAl-M and particularly CuAl-M have some well-defined peaks. The latter thus exhibits a sharp peak between 220 and 280 ^{o}C that is attributed to CuS whose boiling point is of 220 ^{o}C [116]. Its second peak, that is broad, is located in the 400-700 ^{o}C range and is assigned to the decomposition of $CuSO_4$, that boils at 650 ^{o}C, into SO_2, CuO, and O_2. $CuSO_4$ is likely the result of the oxidation of CuS when enough oxygen from the air stream was present on the surface.

To determine whether the adsorption products are acidic or basic, pH values of suspensions of the different samples before and after H_2S adsorption were measured (Table 8).

Despite the presence on its surface of Si-OH groups, Na-M gives a slightly basic pH as a result of the presence of more numerous Si-O-Si surface groups. Pillaring Na-M decreases the pH by 1.41 unit, which can be attributed to the calcination of the Keggin ion that releases H^+.

Loading Al-M with metal cations further lowers the pH, which gives acidic suspensions. That can be the result of the calcination of the alumina pillars that have previously been partially hydrated during the loading step. It could also be due to the dehydration and dehydroxylation of the loaded hydrated metal cations during calcination. The latter explanation seems to play a larger role. Indeed, ZnAl-M is the metal-loaded sample with the smallest pH decrease and at the same time it is the material with the lowest metal content. On the other hand, Fe^{3+} and Cu^{2+} are known to form the octahedral complexes $Fe(H_2O)_6^{3+}$ and $Cu(H_2O)^{2+}$, with the latter being more acidic [104]. That

would explain why a lower pH is found with CuAl-M compared with FeAl-M, despite the latter PILC containing more metal.

After H_2S adsorption, no pH change is found for FeAl-M, which further supports the assumption that H_2S adsorption on it results in the formation of weakly adsorbed SO_2 that is easily desorbed at room temperature. The same can be said about ZnAl-M. On the other hand, the pH decreases by 0.30 unit for CuAl-M, so the adsorption H_2S on it generates the formation of acidic reaction products.

It is noteworthy to mention how the samples changed color once they were exhausted: while FeAl-M (brick red) and ZnAl-M (pale gray) hardly changed (they become slightly lighter), CuAl-M went from dark gray to dark green that is the colour of $CuSO_4$. Thus, there is no doubt then that a change in surface chemistry did happen with CuAl-M upon H_2S adsorption.

Consequently, a mechanism of H_2S adsorption on these metal loaded PILCs can be proposed. It is believed that the mechanism of H_2S adsorption on ZnAl-M and CuAl-M proceeds through Lewis acid-base reactions. In a first step, a metathesis reaction takes place where a hydrated Me^{n+} acts as an acid toward the base S^{2-}, while H^+ and H_2O compose the other acid-base pair:

$$Me^{n+}(H_2O)_m + H_2S \rightarrow MeS^{(n-2)+}(H_2O)_{m-2} + 2\,H_3O^+ \qquad \textbf{(16)}$$

While S^{2-} is a soft base, H^+, H_2O and Fe^{3+} are hard acids. On the other hand, Zn^{2+} and Cu^{2+} are borderline (between soft and hard) acids [104]. As Lewis acids and bases preferably bind to species of similar hardness [117, 118], the metathesis reaction occurs

more readily with Zn^{2+} or Cu^{2+} than with Fe^{3+}. In the absence of any loaded metal, the only acids present in the PILC are Si^{4+} and Al^{3+}which are hard. Their binding to O^{2-}, a hard base [118], makes them even harder [104], especially compared to Fe^{3+}, which explains the negligible capacity of Al-M despite its developed microporosity. The H_3O^+ ions released by this reaction would account for the pH decreases observed on CuAl-M after H_2S adsorption. The sulfides formed from that reaction could then be oxidized by oxygen from air into sulfates, a phenomenon that seems to happen with CuAl-M:

$$CuS + 2\ O_2 \rightarrow CuSO_4 \qquad \textbf{(17)}$$

$CuSO_4$ thus formed would dissolve into the water film present on the PILC surface, which would make Cu^{2+} available for adsorption. That would explain why apparently a single Cu^{2+} can participate in the immobilization of more than one H_2S molecule. This process no longer takes place when no more $CuSO_4$ can dissolve into the water film. At this moment, breakthrough of H_2S takes place.

The difference in capacity between ZnAl-M and CuAl-M is probably primarily related to their loading levels: the quantity of copper is more than twice the quantity of zinc. The superior efficiency in H_2S adsorption of copper over zinc could lie in the kinetics of sulfide oxidation. Indeed, having more loaded metal than ZnAl-M, CuAl-M contains more binding sites for sulfur. Thus, reaching a concentration for H_2S of 1000 ppm took longer for CuAl-M than for ZnAl-M. As a consequence, the contact time with air of CuS was more prolonged than that for ZnS, so formation of sulfates in the case of copper was favored. Differences in sulfide dissociation constants may also be a factor:

the K_S of CuS ($1.27*10^{-36}$) is much smaller than the K_S of ZnS ($2.93*10^{-25}$) [116], so formation of CuS is much more favorable. Formation of SO_2 also seems to occur with ZnAl-M and CuAl-M, but to a lesser extent than with FeAl-M: when [H_2S] was equal to 350 ppm in the effluent gas with the former two PILCs, [SO_2] was of only 0.3 ppm.

From the H_2S breakthrough test results, it turns out that microporosity alone is not sufficient to insure good adsorbing properties for H_2S: the presence of active species is required for that matter. Loading a pillared clay with iron, zinc, or copper leads to materials with some capacities for H_2S adsorption. While copper gave the best results with a relatively low degree of loading (and a small loss of microporosity compared to the original PILC), iron yielded the least satisfying results despite a high metal content (and a large microporosity loss compared to the original PILC). This shows that not only is the identity of the loaded metal an important factor in the adsorption of H_2S, but the metal content (as too much metal may clog pores), the location of that metal, and its degree of dispersion seem to play a role in that process. While H_2S adsorption yields weakly adsorbed SO_2 with iron, zinc and copper converted H_2S into sulfides that were further oxidized into sulfates. CuAl-M is the most efficient adsorbent, with the most dramatic changes observed as a result of H_2S adsorption.

4.3. Porous Clay Heterostructures Loaded with Metals

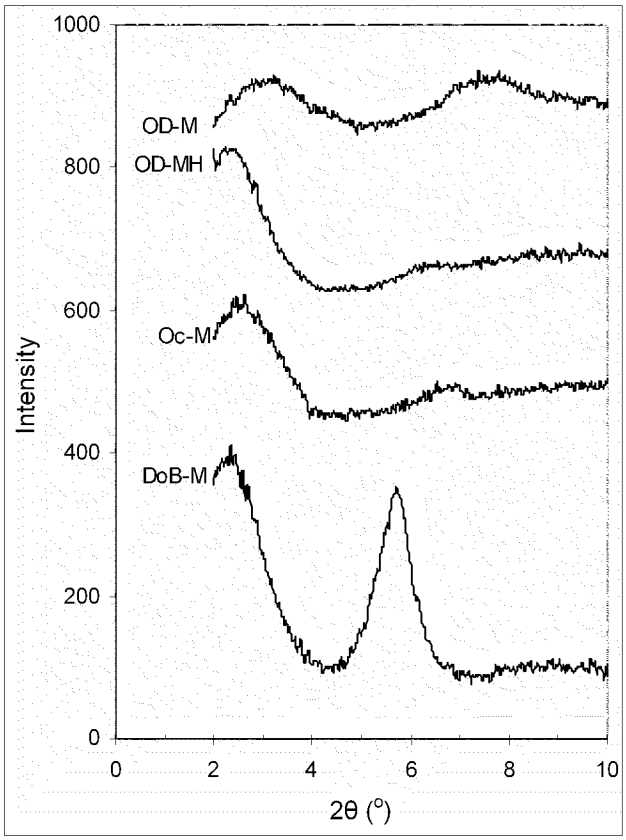

Figure 42: XRD of Oc-M, DoB-M, OD-MH, and OD-M

When Na-M is only exchanged with dodecyltrimethylammonium bromide (DoB) $CH_3(CH_2)_{11}N(CH_3)_3^+Br^-$, the resulting material, DoB-M, shows two peaks on its XRD pattern, at 2.42 and 5.70 ^{o} (Figure 42). As seen previously, Na-M originally has a diffraction peak at 6.98 ^{o} corresponding to an interlayer distance of 3.1 Å.

The fact that DoB-M shows two peaks instead of one can seem surprising, as a unique interlayer distance is expected. This may be due to a non-uniform introduction of the dodecyltrimethylammonium in the clay gallery, which would result in two possible interlayer distances, 26.8 and 5.9 Å (from the Bragg's law). It is likely that the dodecyltrimethylammonium molecules are located in close proximity to the clay charge deficits. Since Na-M is a natural clay, those charge deficits are randomly spread in the material and so are the dodecyltrimethylammonium molecules that would be directly responsible for the 26.8 Å spacing. Furthermore, these molecules, due to their length, could indirectly keep the clay layers farther apart than in Na-M in regions where they are not present, which would explain the second spacing of 5.9 Å.

When Na-M is modified with the neutral surfactant octylamine (Oc) $CH_3(CH_2)_7NH_2$ to give Oc-M, only one peak appears on the XRD pattern at 2.63 ^{o}, corresponding to a spacing of 24.0 Å. That distance is smaller than that for DoB alone, which was expected, since octylamine (eight carbon atoms) is smaller than dodecyltrimethylammonium (twelve carbon atoms). The presence of a single peak with Oc-M proves that Oc is uniformly present between the clay layers. Nevertheless, a small shoulder at 6.93 ^{o} still exists on the XRD pattern of Oc-M, which indicates that a small fraction of Na-M may not have been modified with Oc and remains unchanged. When

DoB and Oc are combined to yield OD-MH, a single peak at 2.43 ^{o} is found. This corresponds to the same spacing determined for DoB-M. Thus, of the two surfactants, it is dodecyltrimethylammonium, the charged molecule, that is responsible for the interlayer distance. Unlike DoB-M, OD-MH exhibits only one interlayer distance, due probably to the uniform intercalation of Oc. When OD-MH is calcined at 450 ^{o}C to give OD-M, two broad peaks appear, one at 3.22 ^{o} corresponding to 17.8 Å and another one at 7.23 ^{o} corresponding to 2.6 Å. The smaller distance is close to the original interlayer spacing for Na-M, while the larger distance is significantly shorter than that for OD-MH. Those two peaks thus show that following calcination, two regions in the clay gallery coexist in the obtained material, with, on the one hand, a region where the two surfactants have been completely removed and, on the other hand, a region where some remnants of the surfactants are present. These remnanats are probably some carbon deposits as the black color of OD-M suggests (Na-M is originally light gray). With a spacing of 17.8 Å, it can be said that those carbon deposits within the silica open framework are rather important, mainly filling the pores generated through the template synthesis. Since the two XRD peaks have similar intensities, it can be assumed that the fraction of PCH with carbon present in its gallery is quite significant.

The absence of any peak on the XRDs of Si-AlM0 and Si-OcAlM (Figure 43) shows that the clay is not intercalated with any species, in particular silica. In contrast, Si-DoBAlM has a peak at 2.50 ^{o} for a spacing of 25.7 Å, so silica is present in the clay gallery. That spacing is close to the one found for DoB-M, thus suggesting the structure-directing role of dodecyltrimethylammonium. The XRD of Si-DoBAlM also features a small shoulder at 7.27 ^{o} for a spacing of 2.6 Å indicative of areas in the material with

absolutely no intercalated species. Since in DoB-M, dodecyltrimethylammonium was only partially introduced, the same phenomenon should have occurred during the synthesis of Si-DoBAlM, resulting in regions where neither dodecyltrimethylammonium molecules nor silica is present in the clay gallery. Si-AlMH exhibits a peak at 2.58 ^{o} and a small shoulder at 6.98 ^{o}. The former corresponds to a spacing of 24.7 Å while the latter indicates the presence of some unmodified Na-M with a spacing of 3.0 Å. Si-AlM only shows a peak at 2.82 ^{o} for a distance of 21.8 Å. The interlayer spacing thus decreases upon calcination, which is compatible with dehydration of the introduced silica.

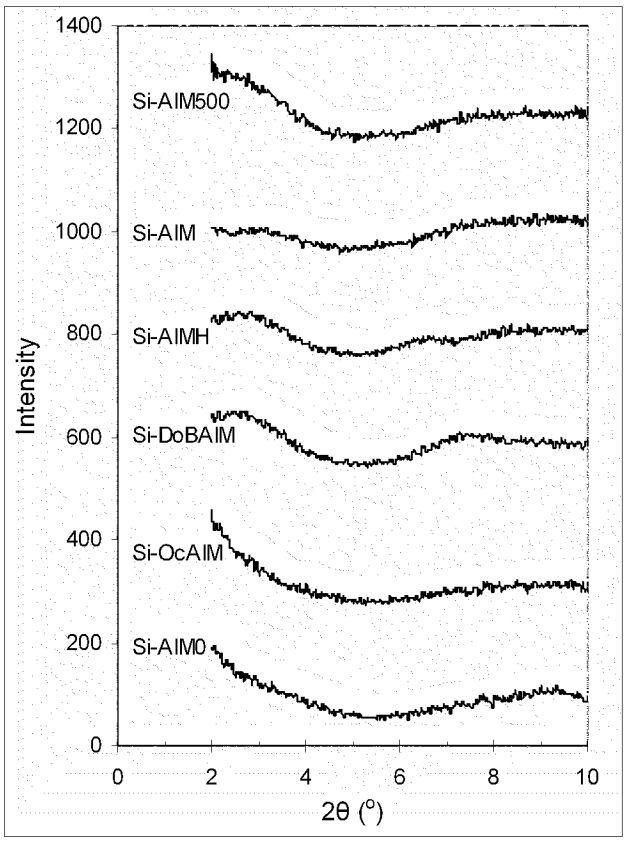

Figure 43: XRD of Si-AlM0, Si-OcAlM, Si-DoBAlM, Si-AlMH, Si-AlM, and Si-AlM500

Si-AlM500, the sample obtained by calcining Si-AlMH at 500 °C, shows no diffraction peak, which indicates that at temperatures between 450 and 500 °C, the clay intercalated with silica starts to lose its well-ordered layered structure, which justifies the choice of a calcination temperature of 450 °C.

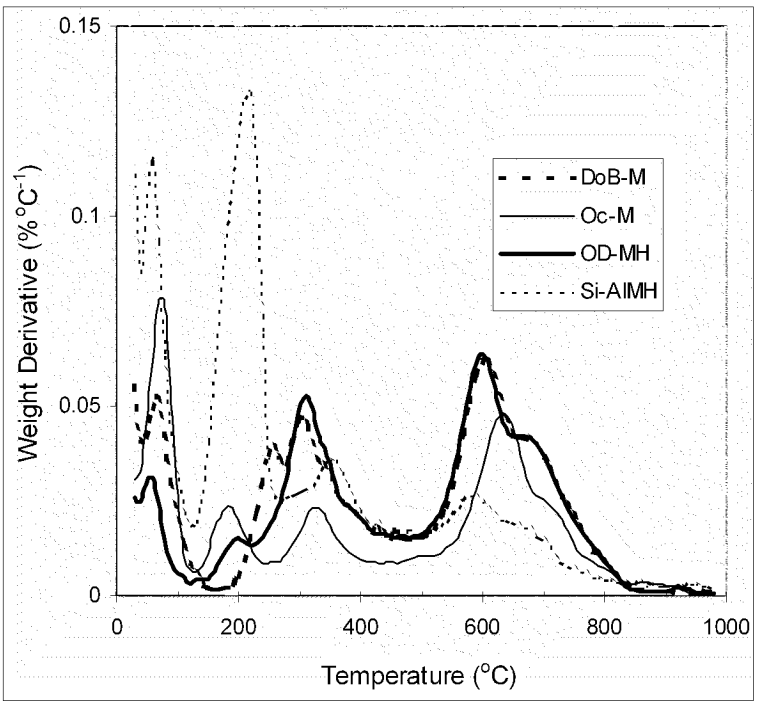

Figure 44: DTG curves in air of Oc-M, DoB-M, OD-MH, and Si-AlMH

The DTG curves in air of Na-M modified solely with Oc and DoB, respectively Oc-M and DoB-M, show two peaks aside from a peak at 600 °C (Figure 44): they are situated at 190 and 330 °C for Oc-M, and at 260 and 300 °C for DoB-M. For both Oc-M and DoB, the lower temperature peak is attributed to the desorption of water bound to the surfactants through their polar head groups, while the higher temperature peak is related to the removal of species as a result of the surfactants' thermal degradation [13]. In both

cases, that removal process is complete between 400 and 450 °C. The higher temperature for water removal with DoB-M compared to Oc-M can be explained by the higher hydrophilicity of the polar headgroup in dodecyltrimethylammonium compared to octylamine due the presence in the cation of a positive charge [52]. When both surfactants are present as it is the case with OD-MH, that water is removed at 200 °C, the same temperature as with Oc-M. This can be explained by the presence in much larger quantities (a 10:1 ratio) of Oc compared to DoB.

More water is desorbed from the gallery of Si-AlMH since the peak present around 200 °C has a much higher intensity than that for Oc-M and DoB-M. That intensity increase is probably due to the formation of aqueous silicate during the synthesis of Si-AlMH that becomes silica upon calcination. The second peak for Si-AlMH is also at a higher temperature (360 °C) compared to the two previous samples. Indeed, this peak not only accounts for the removal of surfactants, but for the dehydration of silicate as well.

Oc-M, DoB-M, and Si-AlMH all exhibit a peak at around 600 °C that is attributed to dehydroxylation of the clay layers, which entails a collapse of the clay layered structure that starts slightly before 500 °C. It can then be concluded from all these DTG curves that the chosen calcination temperature of 450 °C was appropriate for our samples since at that temperature as much surfactant as possible has been removed, silicate has been totally dehydrated, and the layered clay structure has been preserved.

To check for the actual presence of carbon deposits in Si-AlM as a consequence of surfactant thermal degradation, the TG (Figure 45) and DTG (Figure 46) curves of Si-AlM in air and in nitrogen are compared.

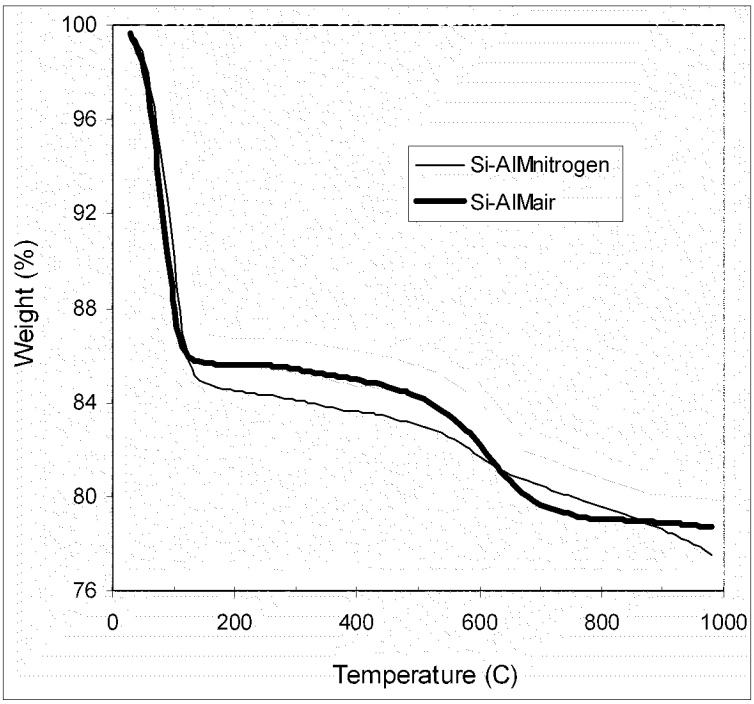

Figure 45: TG curves of Si-AlM in air and in nitrogen

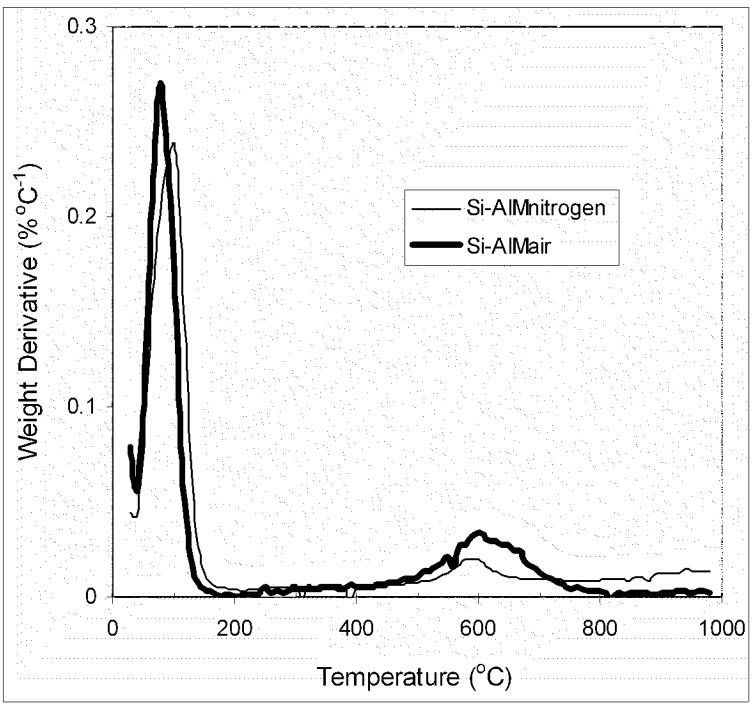

Figure 46: DTG curves of Si-AlM in air and in nitrogen

Before 600 °C, the two TG curves for Si-AlM follow the same pattern. But from 600 to 800 °C, the TG curve for Si-AlM has a steeper slope in air than in nitrogen. The DTG curve for Si-AlM has a higher peak in air than in nitrogen in that same temperature range.

This additional mass loss for Si-AlM in air compared to nitrogen between 600 and 800 °C would be consistent with the combustion of carbon in Si-AlM. This would support the hypothesis about the presence of carbon deposits as a result of surfactants thermal degradation. The amount of carbon in Si-AlM would then correspond to this excess mass loss in air that is estimated to represent 1.01%.

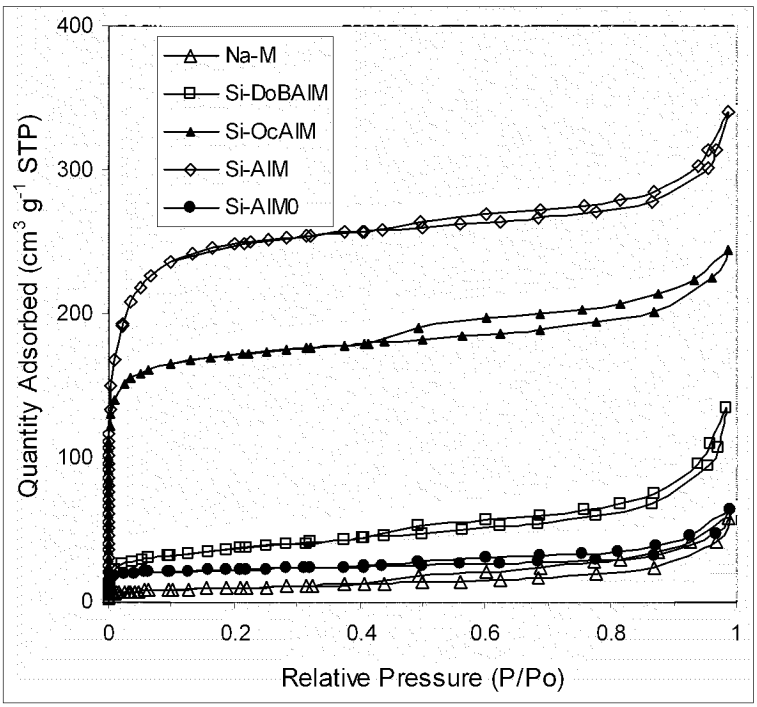

Figure 47: N_2 adsorption-desorption isotherms after different modifications

Table 9: Structural parameters after different modifications

	S_{BET} ($m^2 g^{-1}$)	V_{DR} ($cm^3 g^{-1}$)	V_t ($cm^3 g^{-1}$)
Na-M	33	0.014	0.088
Si-AlM0	71	0.036	0.099
Si-DoBAlM	126	0.051	0.208
Si-OcAlM	542	0.277	0.379
Si-AlM	629	0.301	0.430
Fe-SiAlM	566	0.269	0.390
Zn-SiAlM	436	0.171	0.333
Cu-SiAlM	489	0.200	0.455

The N_2 adsorption-desorption isotherm of Si-AlM0 (Figure 47) shows that reacting TEOS alone with Na-M hardly generates any additional porosity: the microporosity and total porosity increases remain limited (Table 9). It then seems that the experimental conditions used for the synthesis of Si-AlM0 do not allow the hydrolysis and condensation of TEOS into silicate to a significant extent. In the presence of the positively charged surfactant from DoB, a certain degree of porosity is generated: Si-DoBAlM is both more microporous and mesoporous than Na-M. It has been seen earlier that from its XRD pattern, Si-DoBAlM has some silica present between its layers. That silica should be the source of additional microporosity. However the structural parameters of Si-DoBAlM indicate that this material is mainly mesoporous. From the XRD pattern, it was suggested that the cationic surfactant in Si-DoBAlM is only partially present in the gallery. On the other hand, that surfactant was used in excess, since the cation exchange capacity of Na-M is of 0.764 mmol/g while a 2 mmol/g ratio was used. That excess must then be present on the outer clay surface and more surfactant should be present on the clay surface than in the clay gallery. Thus, more silicate should form on

the clay surface than in the clay gallery, which would explain why Si-DoBAlM is more mesoporous than microporous.

In the presence of the neutral surfactant octylamine, a considerable amount of porosity is generated as can be seen for Si-OcAlM. Nevertheless the XRD pattern of Si-OcAlM ruled out the presence of silica between layers. The new porosity, which is essentially microporosity, found with Si-OcAlM should then be located on the outer clay surface, as a result of the deposition of silica particles on it. Actually, it appears that Si-OcAlM is a mixture of two different phases, the unmodified starting clay and silica. When both the neutral and cationic surfactants are present as it is the case with Si-AlM, the porosity gain is the largest. On the other hand, results from N_2 adsorption-desorption show that Si-AlM is mainly a microporous material so its silica should essentially be located in the clay gallery, even though some silica must be present on the outer surface where it forms mesopores.

These results indicate that both surfactants play complementary roles in the synthesis of PCHs. Each surfactant alone is able to induce the formation of silicate from TEOS. By analogy with the phenomena that take place during the synthesis of various silica-based molecular sieves, that silicate in the case of Oc should be neutral and interact through hydrogen bonding (between hydrogens on the silicate and lone electron pairs on the surfactant) with Oc [96], while in the case of DoB, a negatively-charged silicate forms and binds by coulombic forces to the positively-charged surfactant [94]. Different silicates then form depending on whether octylamine or dodecyltrimethylammonium is used as TEOS hydrolyzes under different conditions, respectively basic or acidic. When only octylamine is present, the base-catalyzed hydrolysis of TEOS rather happens on the outer clay surface. This may be due to the presence of larger quantities of water and

faster kinetics of hydrolysis reaction there than in the gallery. However when dodecyltrimethylammonium is the only surfactant, silica preferentially forms in the clay gallery. That may have to do with the fact that dodecyltrimethylammonium, with its charged head group, is more hydrophilic than octylamine, so using a cationic surfactant entails the presence of larger quantities of water in the gallery than on the outer surface. As a consequence, hydrolysis of TEOS with dodecyltrimethylammonium is essentially confined to the clay gallery. But as it is charged, only a limited amount of dodecyltrimethylammonium, and thus of silica, can be introduced in the gallery. No such restrictions exist with Oc. It can then be concluded that while dodecyltrimethylammonium entices the formation of silica between the layers, the role of octylamine is to have silica present in a significant amount in the gallery.

To understand the role of each surfactant on the pore sizes, the PSDs of Si-DoBAlM, Si-OcAlM, and Si-AlM are compared (Figure 48). The microporosity generated in Si-DoBAlM is low and its PSD features two peaks, one at 14.2 Å and another one at about 17 Å consisting of a sharp peak at 17.0 Å and a small shoulder at 22.4 Å. Compared to Si-DoBM, the microporosity in Si-OcAlM is more significant, with peaks at 9.5 Å and 15.6 Å. Si-AlM has two peaks, one at 10.6 Å and another at about 18 Å that actually consists of two sharp peaks at 15.2 and 18.8 Å. Unlike Si-DoBAlM and Si-OcAlM that were synthesized with a single surfactant, Si-AlM does not feature any pore that is larger than 20 Å, which was in fact expected. As seen previously, the simultaneous presence during synthesis of octylamine and dodecyltrimethylammonium insures that silica forms almost exclusively in the clay gallery [93].

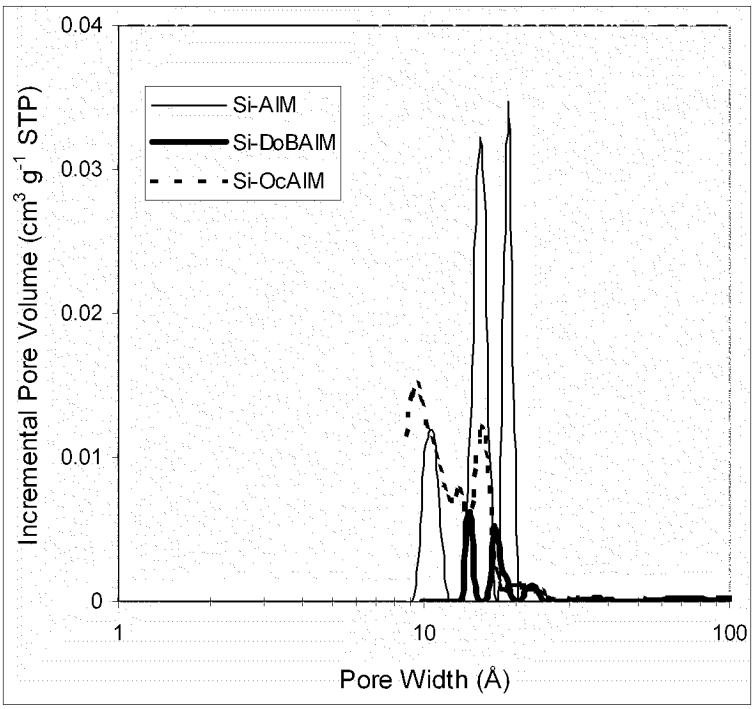

Figure 48: Pore size distributions of Si-DoBAlM, Si-OcAlM, and Si-AlM

From these PSDs, it seems that regardless of the material considered, two kinds of micropore are present. PCHs are believed to form through the condensation and polymerization of silicate around mixed micelles of amine and ammonium [90]. Such a mechanism could result in two sorts of micropores: on the one hand, micropores would be generated by the removal of surfactants through calcination, which would create open silica tubes [90]. On the other hand, voids located between those tubes would result in a second category of micropores. Considering their dimensions and the relative imperfection of the model used for the determination of the PSDs (hybrid DFT), the larger micropore size may correspond to the diameter of the silica tubes that should be

close to the value of the interlayer spacing. As expected, that diameter is larger with Si-DoBAlM (17.0 Å) than with Si-OcAlM (15.6 Å), as dodecyltrimethylammonium is larger than octylamine. The smaller micropore dimension would then be the inter-tube distance. That distance should be larger for Si-DoBAlM than for Si-OcAlM because of electrostatic repulsions between dodecyltrimethylammonium cations, and that is the case (14.2 Å vs. 9.5 Å) on the PSDs of these materials. Si-AlM, resulting from the combination of the two surfactants, has micropore dimensions that are characteristic of both surfactants, with the smaller one (10.6 Å) and the larger one (18.8 Å) apparently determined respectively by Oc and DoB. These findings are consistent with a mechanism where surfactant molecules self-assemble to give micelles around which silica forms. When octylamine and dodecyltrimethylammonium are simultaneously used, mixed micelles containing both surfactants would form, with the head groups of the dodecyltrimethylammonium molecules pointing vertically toward the negatively charged clay layers and the octylamine molecules (present in much larger quantities) forming the remainder of the micelles. Such an arrangement would account for the dodecyltrimethylammonium and the octylamine being responsible for respectively the vertical (and larger) and horizontal (and smaller) dimensions.

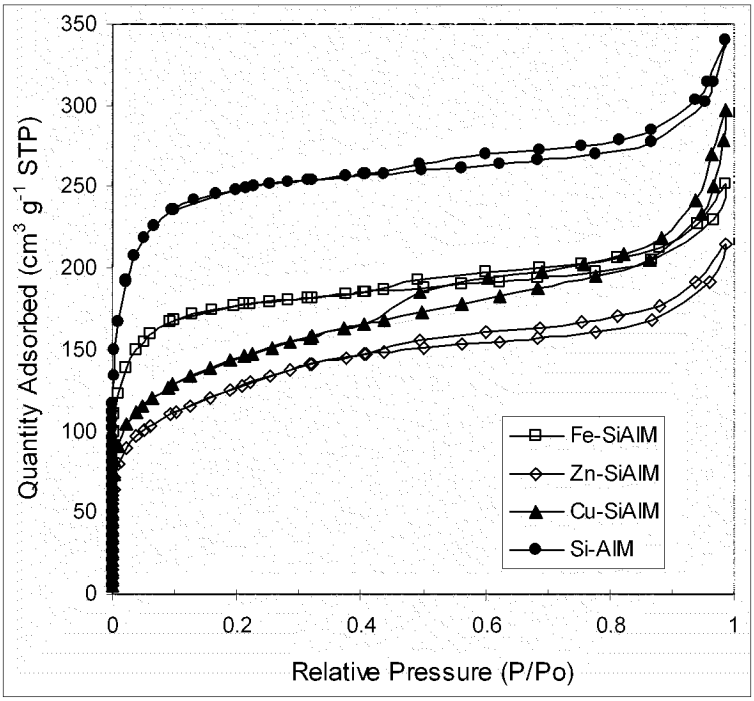

Figure 49: N_2 adsorption-desorption isotherms of Si-AlM, Fe-SiAlM, Zn-SiAlM, and Cu-SiAlM

Results from N_2 adsorption-desorption (Table 9 and Figure 49) show that carrying out a cation-exchange reaction between metal cations (Fe^{3+}, Zn^{2+}, or Cu^{2+}) and dodecyltrimethylammonium prior to the final calcination step entails a porosity loss. For relative pressures larger 0.3, the isotherms for Si-AlM, Fe-SiAlM, and Zn-SiAlM adopt similar shapes and patterns. These three samples thus have equivalent mesoporosities: differences between those materials lie mostly in the micropore region, with the two metal-containing materials having smaller micropore volumes as indicated by lower N_2 intakes at low relative pressures.

Copper exchange generates the most porosity changes, with not only a lower micropore volume, but also some significant mesoporosity created: indeed, the isotherm for Cu-SiAlM is considerably different from the other three, especially in the P/Po range between 0.4 and 1.0. In that range, the slope of the isotherm for Cu-SiAlM steeply increases. As a result, the total porosity for Cu-SiAlM is even larger than that for Si-AlM.

The PSDs of Si-AlM, Fe-SiAlM, Zn-SiAlM, and Cu-SiAlM (Figures 50 and 51) show in more details how cation-exchange with metals affects microporosity. In fact, exchange with Fe^{3+}, Zn^{2+}, or Cu^{2+} does not entail any micropore size shift: with these metals, the distribution peaks in the micropore region only decrease in intensity, with iron having the least dramatic effects. These observations are consistent with the incorporation of the metal cations inside the silica tubes, a process that would be enhanced by the affinity of the amine head groups toward such species [52].

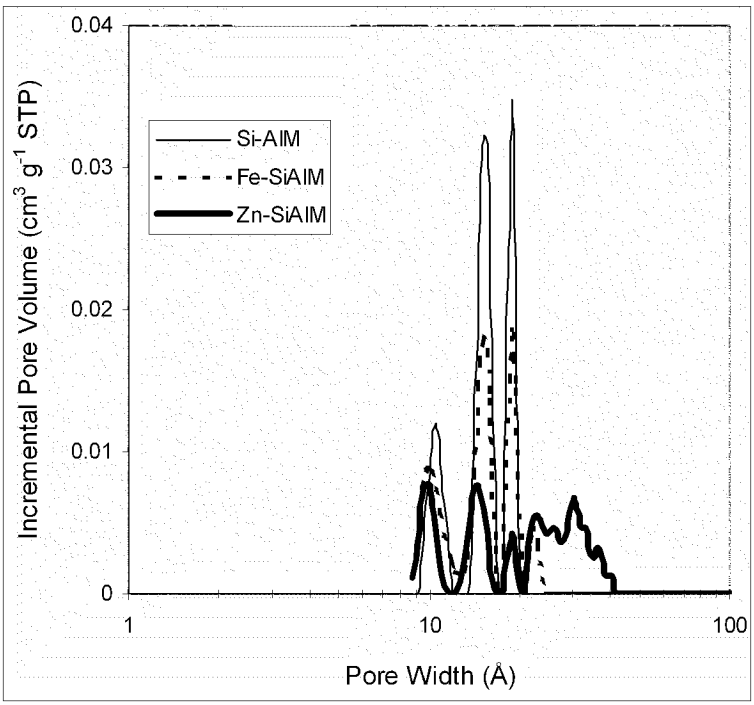

Figure 50: Pore size distributions of Si-AlM, Fe-SiAlM, and Zn-SiAlM

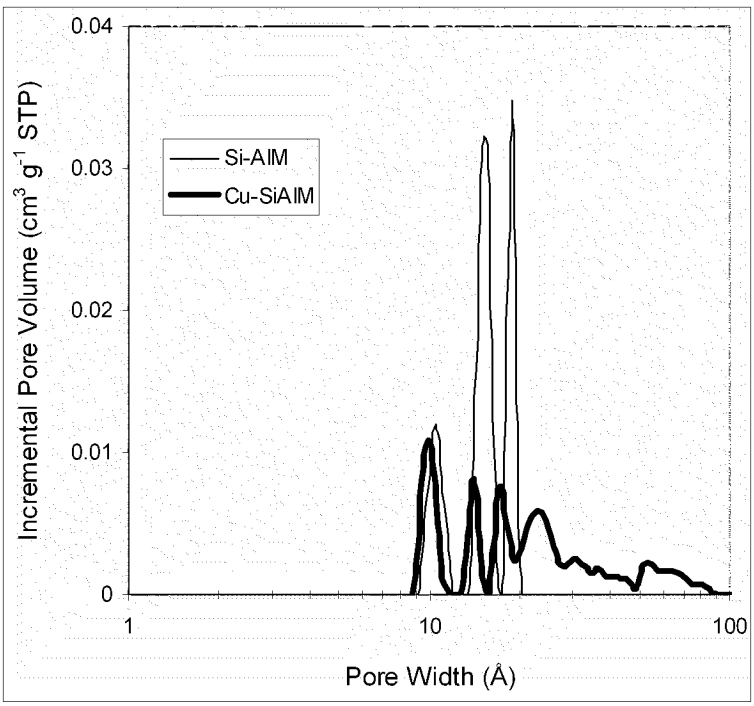

Figure 51: Pore size distributions of Si-AlM and Cu-SiAlM

Of the three metal cations, Fe^{3+} is the one that has the least effects on microporosity. This is probably due to its charge. That charge represents a large mismatch with the clay layers charge deficit of –0.55 and with the dodecyltrimethylammonium cation charge of +1. As a consequence, cation-exchange of Si-AlMH with Fe^{3+} only happens to a limited extent and thus most of the Fe^{3+}, instead of penetrating into the clay gallery, remains on the outer clay surface where it can undergo hydrolysis [38], resulting in deposition on that surface [108]. That would explain why Fe^{3+} induces so few changes in microporosity. The charge differences are less pronounced for Zn^{2+} and Cu^{2+}, so cation-exchange is more extensive with these metals and more pronounced changes in microporosity take place. Indeed, it is recognized that

cations like Zn^{2+} and Cu^{2+} can be exchanged with singly charged ammonium surfactants present in the mesopores of an as-synthesized MCM-41 silica [119].

Alongside microporosity changes, metal cation exchange also entails the generation of mesopores. While for Fe-SiAlM and Zn-SiAlM only mesopores smaller than 40 Å are created, more mesopores and of larger sizes are present in Cu-SiAlM. It is a possibility that as metal cations enter the micelles that serve as templates for the silica tubes, the dodecyltrimethylammonium molecules that are being replaced by the metal cations leave the clay gallery to preserve the clay electroneutrality and migrate toward the outer clay surface. At least part of those dodecyltrimethylammonium molecules could still be bound to some silicate moieties, which would result in the deposition of silica upon calcination on the clay surface. That silica would then be responsible for the observed additional mesoporosity. This process of cation-exchange and silica deposition is more extensive with Cu^{2+} than with Zn^{2+}. This may be due to the formation of the $[Cu(H_2O)_6^{2+}]$ octahedral complex as the presence of water ligands favor copper intercalation in the gallery by slightly diminishing the positive charge of the copper atom and by interacting with the hydrophilic clay layers.

A SEM image of Na-M (Figure 52) shows that the starting clay consists of smooth-surfaced particles that form large agglomerates. Most of these particles do not exceed 4-6 μm in sizes. The clay surface does not seem to significantly change upon addition of TEOS alone to Na-M, giving Si-AlM0. This is a further indication that TEOS does not hydrolyze when no surfactant is present, as the resulting material has neither introduced material (from XRD) nor silica deposited on its outer surface (from SEM).

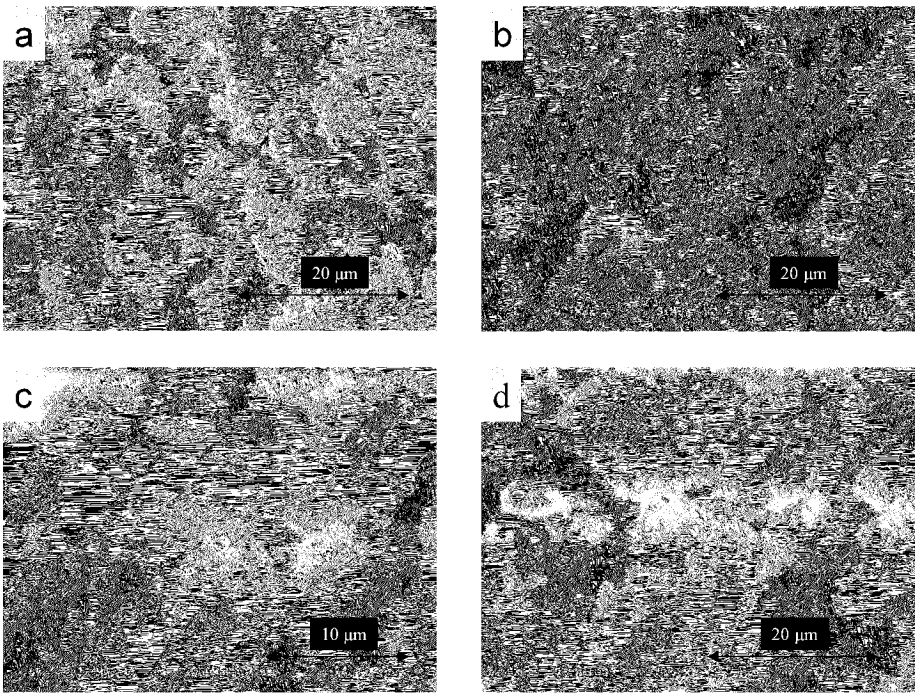

Figure 52: SEM images of (a) Na-M, (b) Si-AlM0, (c) Si-DoBAlM, and (d) Si-OcAlM

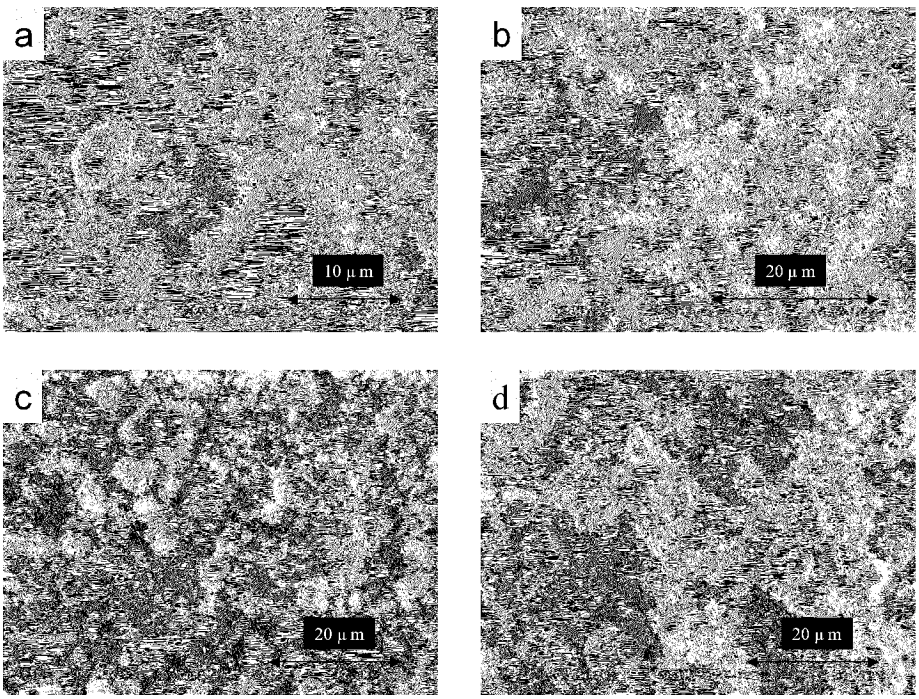

Figure 53: SEM images of (a) Si-AlM, (b) Fe-SiAlM, (c) Zn-SiAlM, and (d) Cu-SiAlM

When DoB is used alongside TEOS, the clay material is covered with a low-density thin layer of a deposit that must be silica, thus confirming that Si-DoBAlM has silica both inside and outside its gallery. When Oc-M and TEOS are combined, a material (Si-OcAlM) with flaky high-density deposits of silica is obtained. From its XRD pattern, this material did not show evidence of introduced silica, so with Si-OcAlM, silica indeed mostly forms on the outer clay surface. When DoB and Oc are used together, Si-AlM turns out to be a material with limited silica deposits, thus confirming that most of the silica formed in that case is present in the clay gallery (Figure 53). These silica deposits are more abundant when cation-exchange has taken place prior to calcination, and Cu-SiAlM is the metal-loaded PCH with apparently the most deposits, which has already been found from N_2 adsorption results.

TEM analysis shows that Na-M consists of plates having different sizes and shapes arranged and stacked in parallel (Figure 54a), as expected for a layered material. When the Si-AlM forms, that arrangement is preserved, but blocks of silica that are 50-100 nm large appear and that silica seems to be embedded in the clay mineral instead of forming a separate phase (Figure 54b). When exchange with iron prior to calcination takes place, bars of iron about 50 nm long are present alongside the silica, located both outside and inside the clay layers (Figure 54c). With the zinc-containing sample, the material's structural organization looks similar to the one for Si-AlM: the presence of zinc is not visible, probably because it did not agglomerate to form larger particles as iron did (Figure 54d). Instead, zinc is likely present in a highly dispersed state. The silica blocks in Cu-SiAlM are darker than the ones for Si-AlM, which is an indication that

those blocks contain metal (Figure 54e). It then seems that copper is indeed loaded inside the introduced silica and that it is present there under the form of large agglomerates.

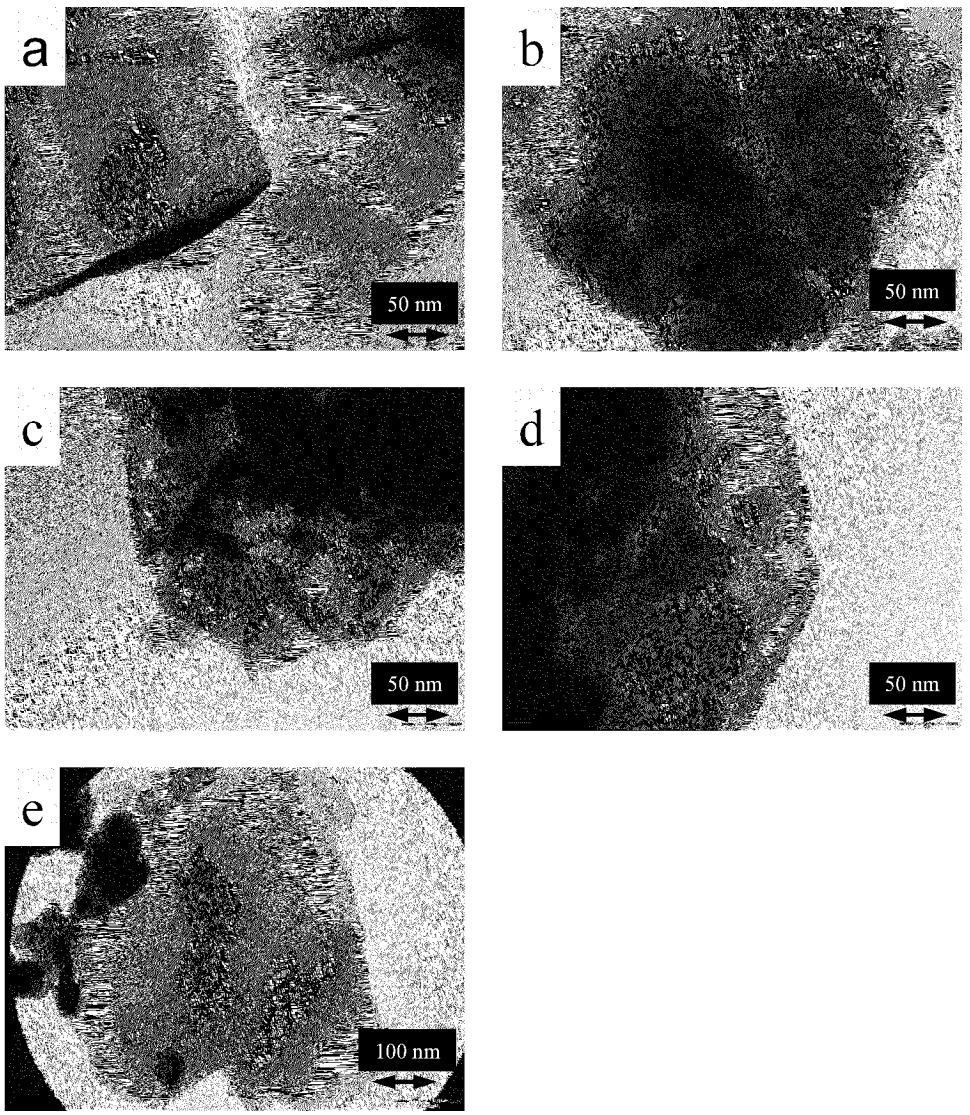

Figure 54: TEM images of (a) Na-M, (b) Si-AlM, (c) Fe-SiAlM, (d) Zn-SiAlM, and (e) Cu-SiAlM

Results from H_2S breakthrough tests on the metal-loaded PCHs (Figure 55 and Table 10) show that even though these materials do adsorb H_2S, their performances are relatively weak.

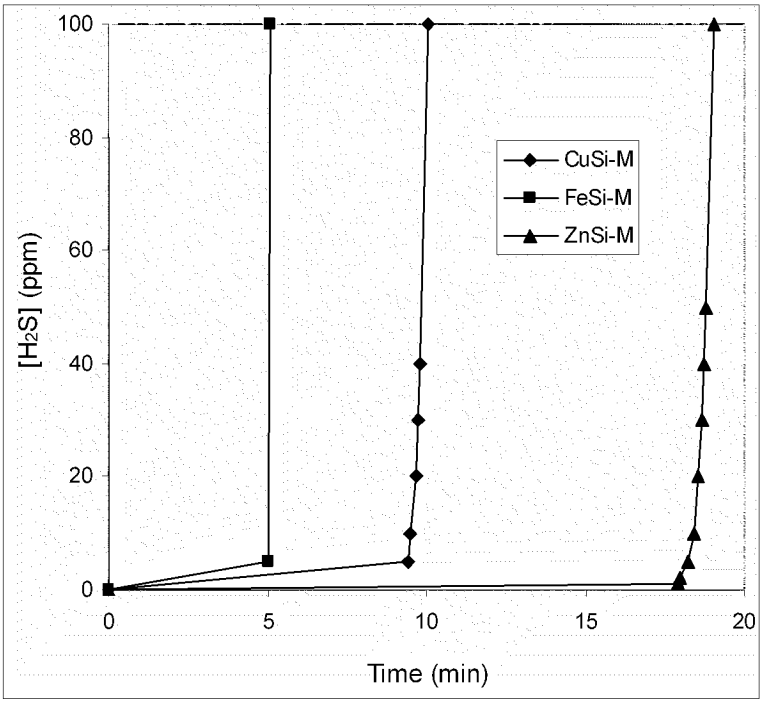

Figure 55: H_2S breakthrough curves of Fe-SiAlM, Zn-SiAlM, and Cu-SiAlM

Table 10: Breakthrough capacities of Fe-SiAlM, Zn-SiAlM, and Cu-SiAlM

	Mass (g)	Breakthrough time (min)	Breakthrough capacity (mg g^{-1})
Fe-SiAlM	2.070	5.0	5.1
Zn-SiAlM	1.914	19.0	20.8
Cu-SiAlM	1.861	10.0	11.3

Even though they have larger micropore volumes than PILCs loaded with the same metals, these PCHs show a lower performance for H_2S adsorption than their PILC counterparts. Several factors may explain this apparent paradox. One of the main reasons could be the size of the pores in the PCHs: as seen from their PSDs, these materials have pore widths in the 10-20 Å range. As mentioned previously, efficient H_2S adsorption requires pores smaller than 10 Å. Another possible explanation may be related to the accessibility of the metal species. As already suggested from the XRD analysis of OD-M and the thermal analysis of Si-AlM, some carbon deposits could be present on the inner walls of the silica tube as a result of the surfactant's thermal degradation. Since for the metal-loaded PCHs calcination takes place after cation exchange, that carbon would cover the metal already present on the silica walls, thus making them unavailable for adsorption.

The presence of carbon in the metal-loaded PCHs is indeed also suggested when comparing the TG and DTG curves (Figures 56-61) of these samples in air and in nitrogen. Differences between TG and DTG curves in air and in nitrogen are similar with the metal-loaded PCHs as with Si-AlM previously. Those differences occur between 500 and 700 ^{o}C for Cu-SiAlM, and between 600 and 800 ^{o}C for Fe-SiAlM and Zn-SiAlM. The percentages of carbon in the PCHs deducted from the differences in mass loss between air and nitrogen analysis in the respective temperature ranges are reported in Table 11.

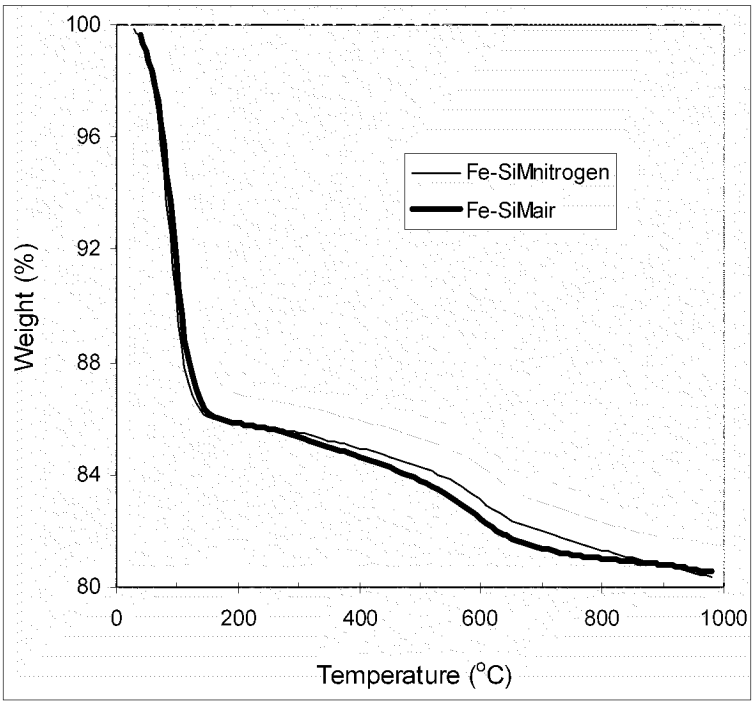

Figure 56: TG curves of Fe-SiAlM in air and in nitrogen

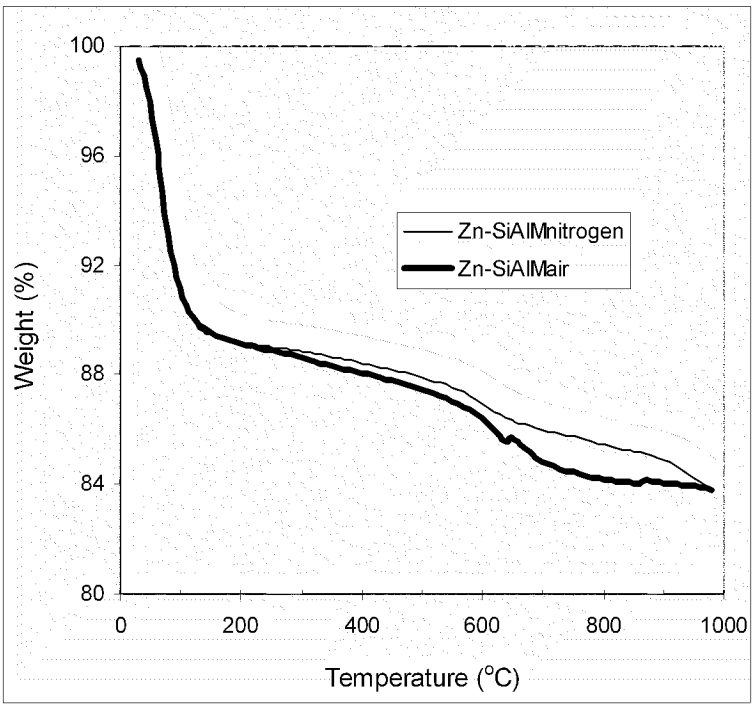

Figure 57: TG curves of Zn-SiAlM in air and in nitrogen

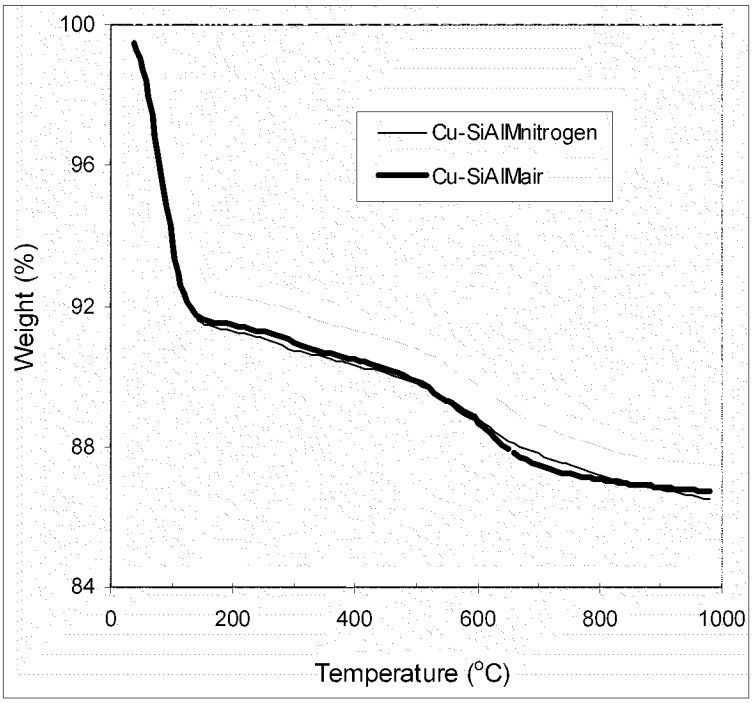

Figure 58: TG curves of Cu-SiAlM in air and in nitrogen

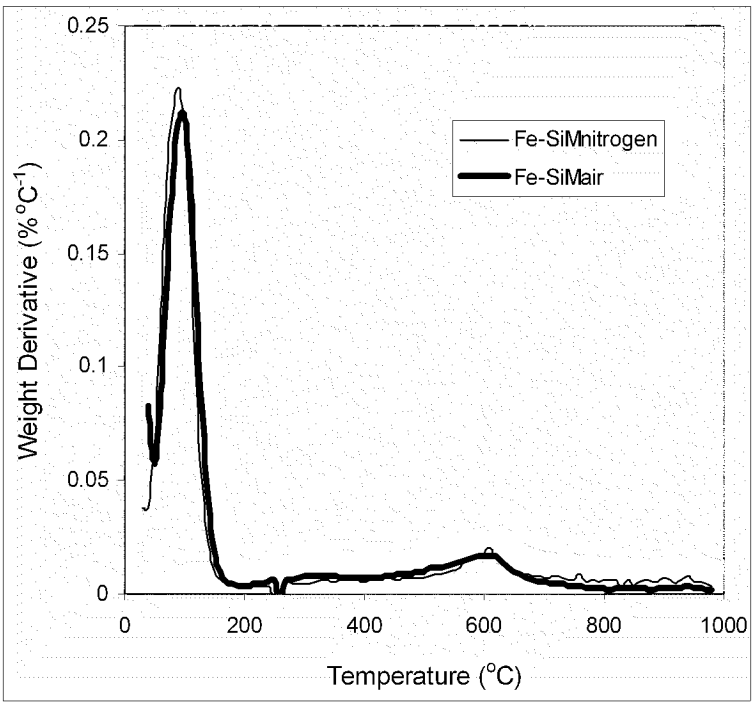

Figure 59: DTG curves of Fe-SiAlM in air and in nitrogen

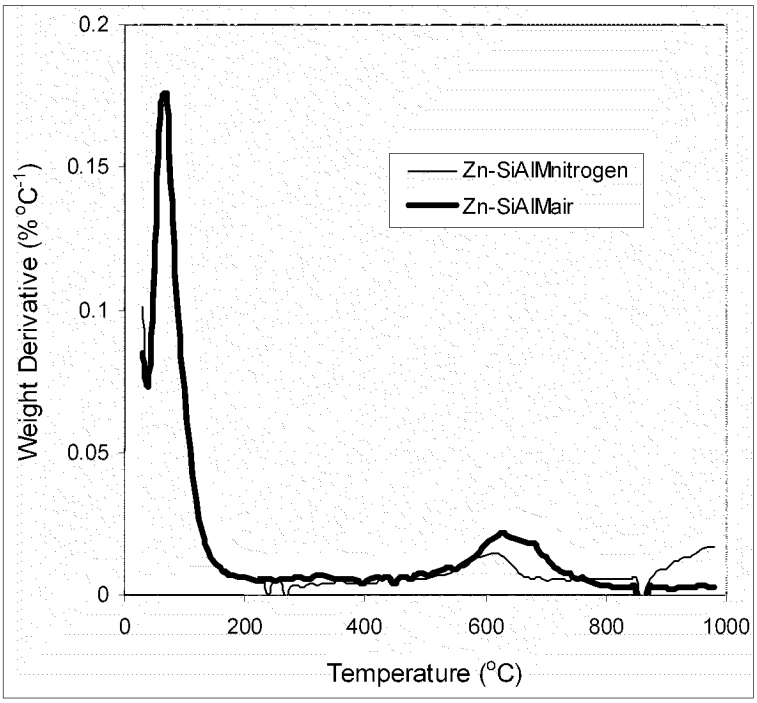

Figure 60: DTG curves of Zn-SiAlM in air and in nitrogen

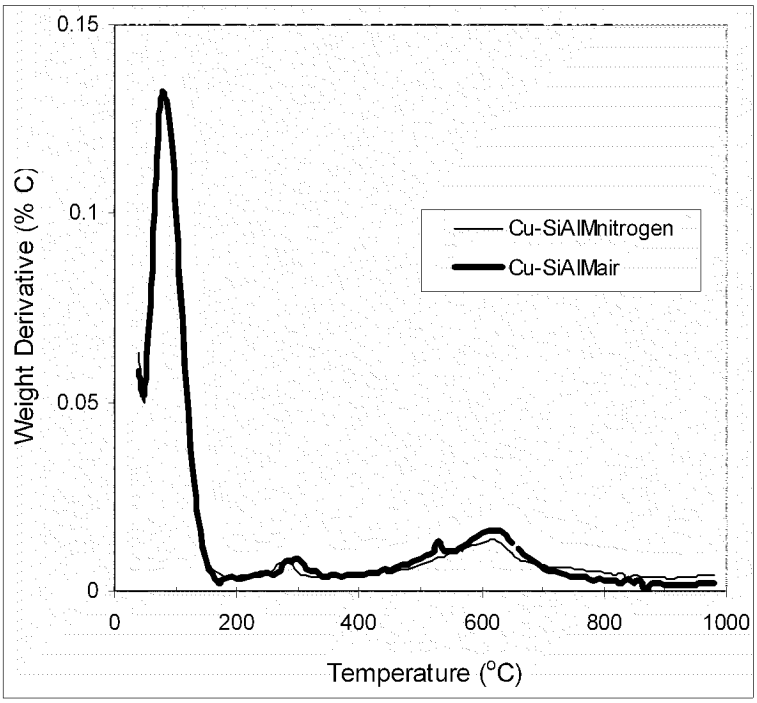

Figure 61: DTG curves of Cu-SiAlM in air and in nitrogen

Table 11: Amount of carbon in the PCHs

	Carbon (%)
Si-AlM	1.01
Fe-SiAlM	0.53
Zn-SiAlM	0.68
Cu-SiAlM	0.33

It can seem quite surprising that the zinc PCH adsorbs H_2S a little better than the copper one, as the copper PILC proved to be a much better material than the zinc one in the same application. But results from N_2 adsorption analysis and SEM analysis suggest that copper is more thoroughly exchanged with dodecyltrimethylammonium than zinc. As a consequence, compared to copper, less zinc should be present in the gallery and more should be located on the outer clay surface. Zn-SiAlM would then have less metal covered with carbon and more active species available for adsorption. Furthermore, TEM analysis showed that unlike iron and copper, zinc in the PCH is present in a non-agglomerated and highly dispersed state, so the fraction of metal in Zn-SiAlM that can play an active role in adsorption should be much higher than that for the other two metal-loaded PCHs.

Consequently, a highly porous material can be obtained from a nonporous natural clay through the hydrolysis of TEOS in the presence of both octylamine and dodecyltrimethylammonium. The resulting PCH is mainly a microporous material, with pore sizes comprised between 10 and 20 Å. The simultaneous presence of two surfactants is necessary for a significant intercalation of silica in the clay gallery, as while dodecyltrimethylammonium allows silica formation there, octylamine provokes the complete introduction of silica between the layers.

When metal cations are loaded by cation-exchange into such PCHs, a loss of microporosity occurs probably as a result of removal of dodecyltrimethylammonium from the clay gallery. That process is likely accompanied by the deposition of silica, also originating from the gallery, on the outer clay surface, which generates additional mesoporosity. That phenomenon is particularly pronounced when Cu^{2+} is used, as cation-exchange is particularly extensive with that cation. Nevertheless, exchanging an as-synthesized PCH with a metal cation before its eventual calcination limits the accessibility of the loaded metal, as carbon deposits resulting from the surfactants thermal degradation cover a large fraction of that metal, as H_2S adsorption tests suggested. However PCHs synthesized in this fashion could serve as inorganic templates for the preparation of mesoporous carbons.

4.4. Metal-Loaded Carbons Templated from Porous Clay Heterostructures

Figure 62 illustrates the evolution of porosity through the different modification steps when a porous carbon (C-M) is synthesized using a porous clay heterostructure Si-AlM as inorganic templates. When sucrose is carbonized following its introduction into the pores of Si-AlM, C-SiAlM, the resulting material, exhibits a porosity that is close to the one for the starting clay, Na-M. This means that the porosity gained from the template synthesis, and particularly microporosity, is almost entirely lost following sucrose carbonization, thus indicating that most of the pores in Si-AlM are filled with carbon. Porosity is partly regained after HF treatment as the isotherm for C-AlM indicates, even though the microporosity of that material remains lower than that for Si-AlM. This

increase in porosity is likely the result of inorganic template removal with silica being mostly removed, which creates pores in the carbon phase. C-M, which results from the treatment of C-AlM with HCl, yields a material that is even more porous, with large nitrogen uptakes. That porosity increase must be due to further removal of the inorganic template, likely some alumina left despite HF washing. Compared to its inorganic template Si-AlM, C-M is less microporous and more mesoporous.

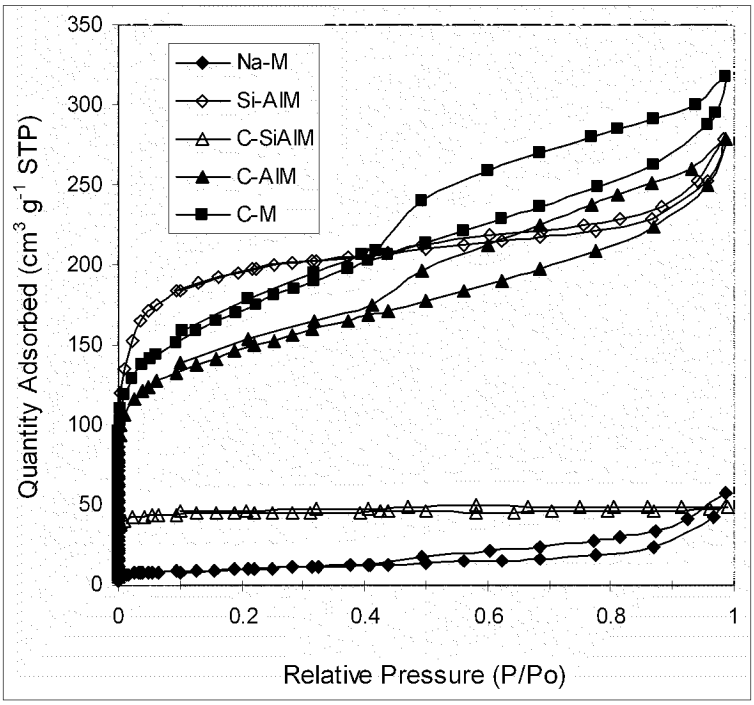

Figure 62: N_2 adsorption-desorption isotherms of Si-AlM, C-SiAlM, C-AlM, and C-M

When metal-loaded PCHs are used as templates, materials having isotherms of comparable shape are obtained (Figure 63). Of all the carbon samples, Cu-CM exhibits the largest microporosity and mesoporosity.

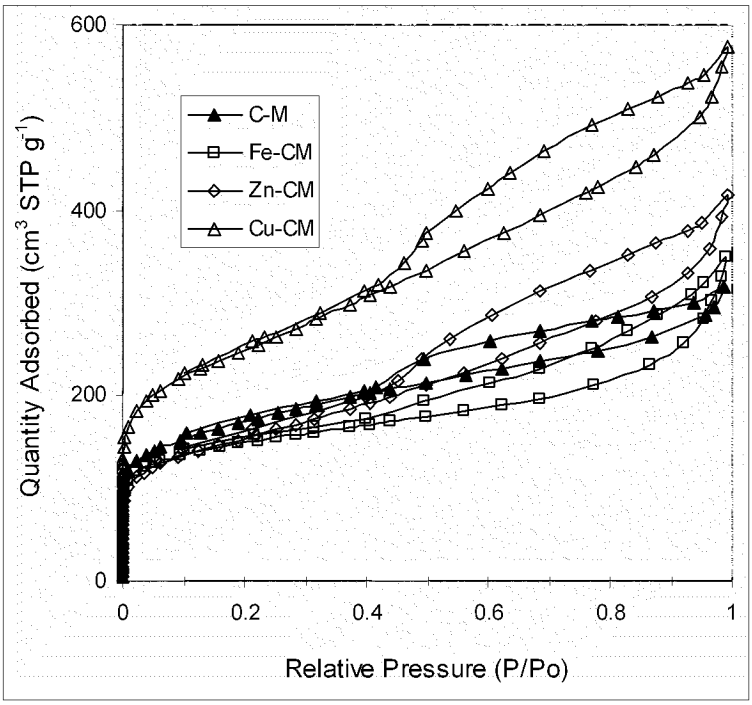

Figure 63: N_2 adsorption-desorption isotherms of C-M, Fe-CM, Zn-CM, and Cu-CM

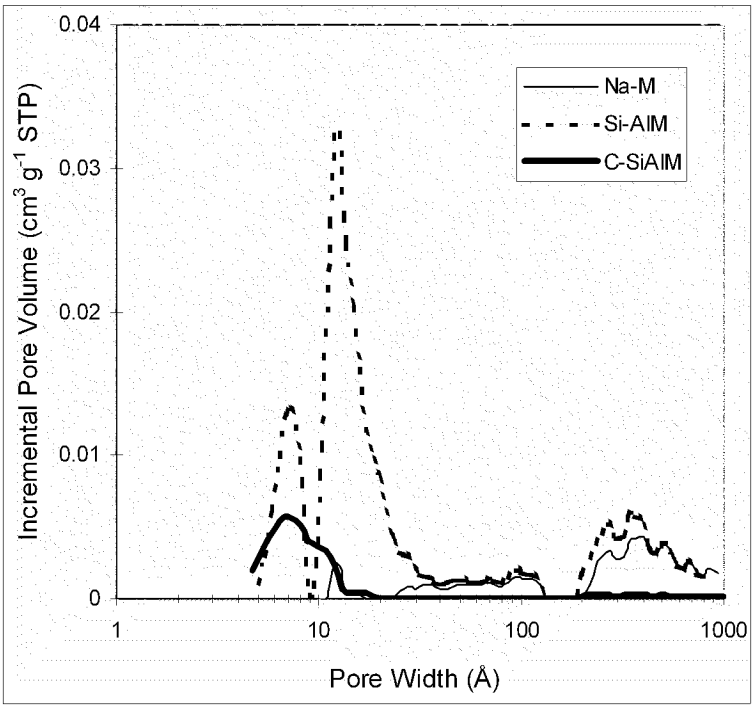

Figure 64: Pore size distributions of Na-M, Si-AlM, and C-SiAlM

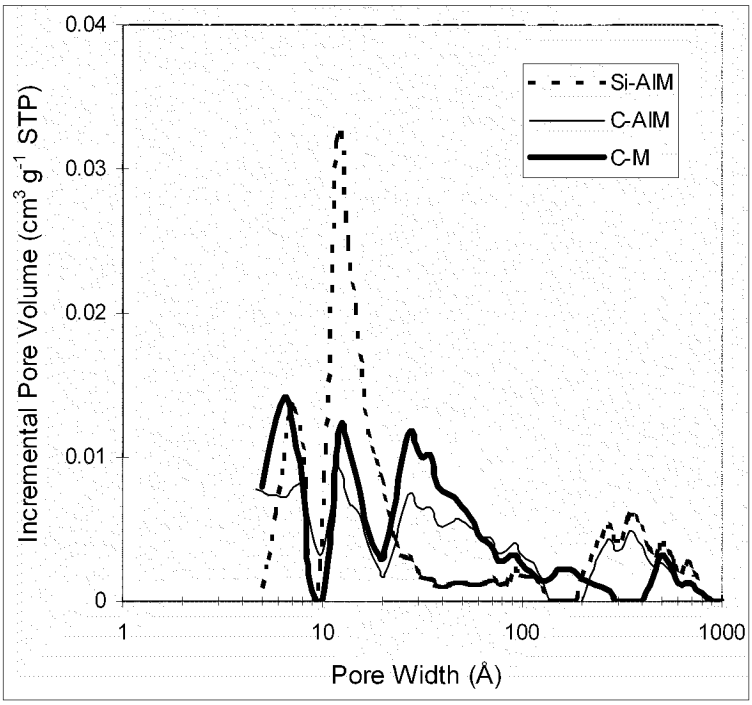

Figure 65: Pore size distributions of C-SiAlM, C-AlM, and C-M

On the other hand, the other carbons show similar micropore volumes, as their N_2 intakes at low relative pressure suggest. It is noteworthy to mention as well that all the metal-containing carbons have a higher mesoporosity than that of C-M.

As already guessed from the N_2 adsorption-desorption isotherms, the PSDs of Si-AlM and C-SiAlM (Figure 64) indicate that most of the pores in the inorganic template are completely filled with carbon after carbonization of sucrose. C-SiAlM thus does not have pores larger than 20 Å and its PSD only consists of a small peak at 7.3 Å that was already present but of higher intensity for Si-AlM.

The PSD of C-AlM (Figure 65) shows that HF treatment yields a highly porous carbonaceous material. It can actually be noticed that C-AlM has micropores of the same size as its template, Si-AlM. Furthermore, the PSDs of these two materials for pores larger than 100 Å are quite identical. All these similarities in porosity tend to show that

C-AlM is, to a certain extent, a replica of Si-AlM. Some additional microporosity is generated following HCl treatment as can be seen on the PSD of C-M. Aside from that, that treatment also seemingly removes mesopores whose sizes are between 200 and 500 Å. These mesopores were originally present in the starting clay, Na-M (Figure 64), so their absence is an indication of the washing out of clay matter.

From the analysis of the PSDs (Figures 66 and 67), C-M, Fe-CM and Zn-CM exhibit similar micropore sizes and volumes. They nevertheless markedly differ in the mesopore region: there, Fe-CM and Zn-CM possess pores that are not present in C-M.

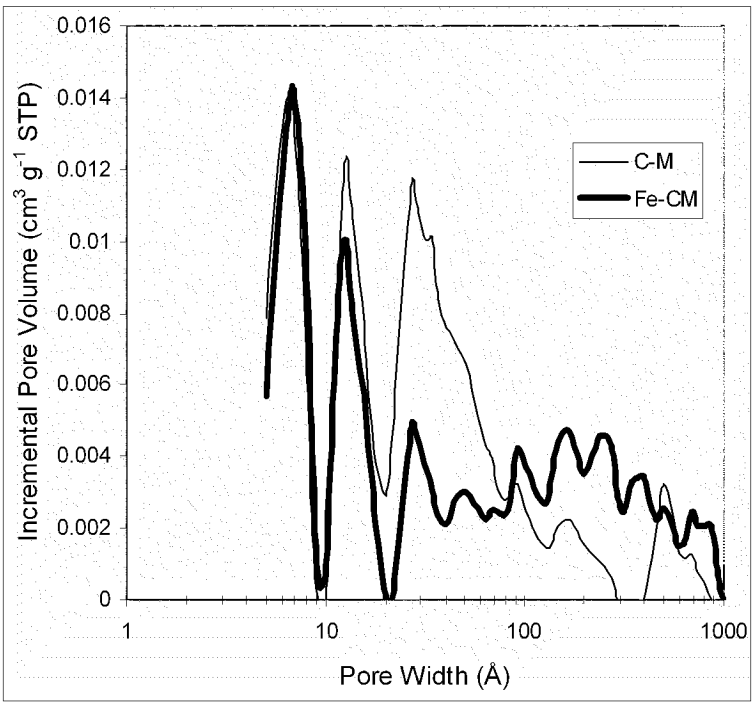

Figure 66: Pore size distributions of C-M and Fe-CM

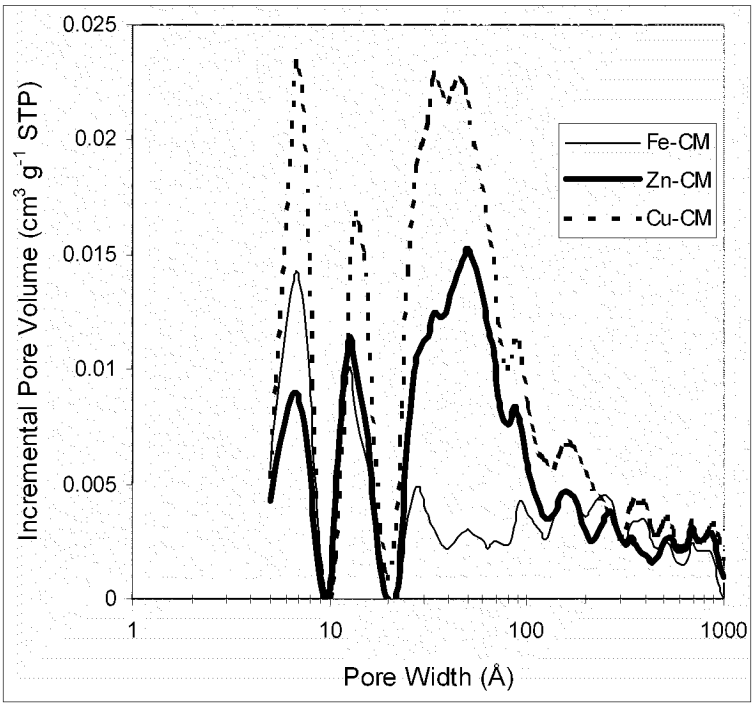

Figure 67: Pore size distributions of Fe-CM, Zn-CM, and Cu-CM

Table 12: Structural parameters of the samples after different modifications

	S_{BET} ($m^2 g^{-1}$)	V_{DR} ($cm^3 g^{-1}$)	V_t ($cm^3 g^{-1}$)
Na-M	33	0.014	0.088
Si-AlM	629	0.301	0.430
C-SiAlM	140	0.072	0.076
C-AlM	490	0.210	0.432
C-M	582	0.234	0.490
Fe-SiAlM	566	0.269	0.390
Fe-CM	492	0.214	0.541
Zn-SiAlM	436	0.171	0.333
Zn-CM	534	0.214	0.644
Cu-SiAlM	489	0.200	0.455
Cu-CM	793	0.310	0.837

The PSD of Cu-CM (Figure 67) confirms that this carbon is much more porous than all the other carbons, with a significant amount of mesopores with sizes between 20 and 100 Å. Overall, all the carbon samples display a developed mesoporosity, a property that has also been found for carbons templated from an unmodified natural clay [41].

When comparing the structural parameters of the carbons to the ones for their inorganic templates (Table 12), it turns out that these materials have comparable surface areas and micropore volumes, which further indicates replication of the clay nanostructures in the final carbons. However, a significant difference between the two types of material exists in the mesopore region, with the carbons being much more porous there. These new mesopores in the carbons are likely the result of the particular arrangement of these materials that are known to adopt a house-of-cards structure formed from stacks of carbon layers [25]. The new mesopores would then be the voids present between those stacks. Despite a lower microporosity and a higher mesoporosity when compared to their templates, these carbons nevertheless still posses a rather high degree of microporosity. It is remarkable that, of all the carbon samples, Cu-CM has the highest surface area and the highest mesopore volume. While the details of the mechanism remain unclear, it is believed that this additional porosity is related to the reduction of Cu^{2+} by carbon during the carbonization process, as this cation has a lower redox potential than Zn^{2+} and Fe^{3+} [116].

Table 13: Metal contents of the carbon samples

	Cu (%)	Fe (%)	Zn (%)
C-M	-	-	-
Fe-CM	0.00	1.24	0.00
Zn-CM	0.00	0.14	0.14
Cu-CM	0.06	0.07	0.00

Results from elemental analysis (Table 13) indicate that only minor amounts of metal are actually present in the carbon samples, with only Fe-CM having a noticeable metal content of 1.24%. This low metal-loading level is likely the result of HF/HCl treatment that washed out the metals originally present in the PCH templates. It then seems that iron proves to be more resistant to HF and HCl washing than zinc and copper. It is possible that part of that iron is present under the form of iron carbide (Fe_3C), which would form during carbonization, as such species have been proven to form under similar conditions as ours [120].

Table 14: Ash contents of the carbon samples

	Ash (%)
C-M	2.33
Fe-CM	1.48
Zn-CM	1.78
Cu-CM	0.12

The ash content in the carbon samples (Table 14) corresponds to the amount of matter left after these samples have been heated from room temperature to 1,000 °C in air. As under those conditions any loss of matter would be the result of the burning of carbon, these materials consist mainly of carbon, as their low ash contents suggest. That ash must either be some inorganic template, silica and/or alumina, left after HF/HCl treatment or metal from the templates. An almost pure sample has thus been obtained with Cu-CM whose ash content is only 0.12%. This percentage actually matches the sum of its iron and copper contents (Table 13), so Cu-CM is completely devoid of template. The ash content of Fe-CM is only slightly superior to its metal content, which also shows a high degree of carbon purity. As for Zn-CM and C-M, even though they are not pure carbons, their ash contents are nevertheless low.

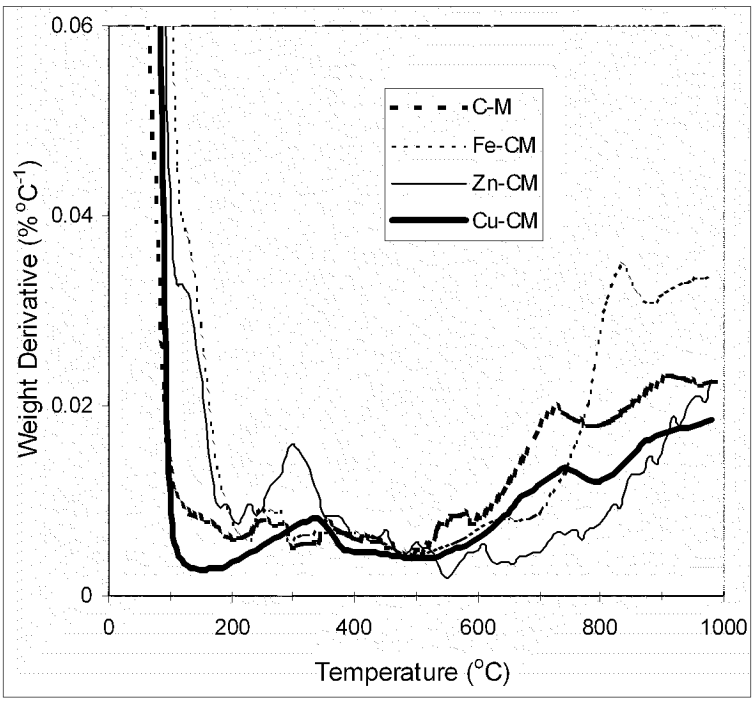

Figure 68: DTG curves of the carbon samples

Thermal analysis in nitrogen reveals differences in the amount of adsorbed water and in surface functionalities [121, 122] between the carbon samples through their DTG curves (Figure 68). Exhibiting the higher peaks for water desorption at around 120 ^{o}C [123], Fe-CM and Zn-CM are the more hydrophilic carbons. Indeed, those two samples possess the highest metal content and that metal favors adsorption of water molecules. Despite having no loaded metal in it, C-M proves to be slightly hydrophilic with a small peak at 150 ^{o}C, which is probably due to some inorganic template (silica and alumina) still present in it. Cu-CM does not show any hydrophilicity, as its DTG curve does not have any peak below 200 ^{o}C accounting for desorption of water. The metal content of Cu-CM is only half the one for Zn-CM that comparatively has a high peak for water desorption. This is another indication of the difference in metal accessibility in Cu-CM compared to Fe-CM and Zn-CM. In the latter two samples, a significant fraction of metal is present on the outer clay surface, thus being exposed to other chemical species. In contrast, it appears that in Cu-CM, since it is hydrophobic, copper is mostly present in the clay gallery where it is covered by carbon resulting from the surfactants calcination. The DTG curves for Fe-CM, Zn-CM, and Cu-CM also feature peaks between 200 and 400 ^{o}C that are likely due to the dehydroxylation of hydrated metal species.

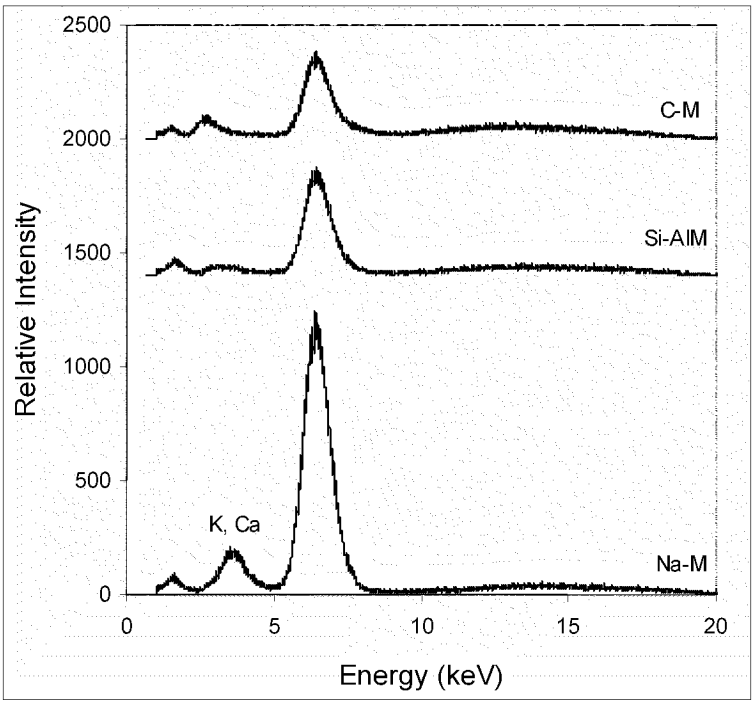

Figure 69: XRF spectra of Na-M, Si-AlM, and C-M

The X-ray Fluorescence (XRF) spectrum of the starting clay Na-M (Figure 69) shows that this material, beside Na^{+}, also contains K^{+}, Ca^{2+}, and iron. That iron is most likely Fe^{3+} that substitutes for Al^{3+} in the octahedral sheets, according to the clay formula. As a consequence, unlike Na^{+}, K^{+}, or Ca^{2+}, that Fe^{3+} cannot take part in cation-exchange processes and should in any case remain embedded inside the clay. This would explain why iron is detected in all the metal-containing carbons (Table 13).

Comparing their XRF spectra, the relative amount of iron is lower in Si-AlM than in Na-M. But since that relative amount decrease cannot be due cation-exchange, this must then be the result of an incorporation of large quantities of silica between the clay layers upon formation of the PCH, which would then lower the fraction of iron. That fraction only slightly decreases from Si-AlM to C-M, so the aluminosilicate template has been replaced by an equivalent amount of carbon.

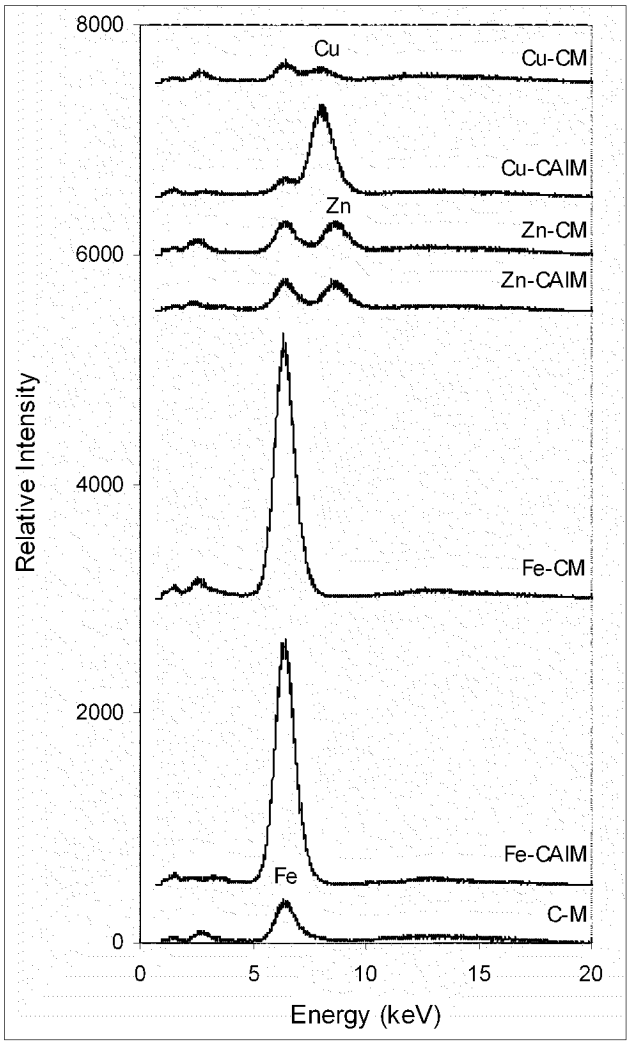

Figure 70: XRF spectra of C-M, Fe-CAlM, Fe-CM, Zn-CAlM, Zn-CM, Cu-CAlM, and Cu-CM

When the XRF spectra of C-M and Fe-CM (Figure 70) are compared, it can be seen that using Fe-SiAlM as template gives a carbon material with significantly more iron. The relative amount of iron in Fe-CM is similar to that for Fe-CAlM, so HCl treatment hardly removes iron from Fe-CAlM. The same can be said about zinc. In contrast, HCl drastically reduces the relative copper content, which explains why Cu-CM turns out to be the carbon with the lowest metal-loading level.

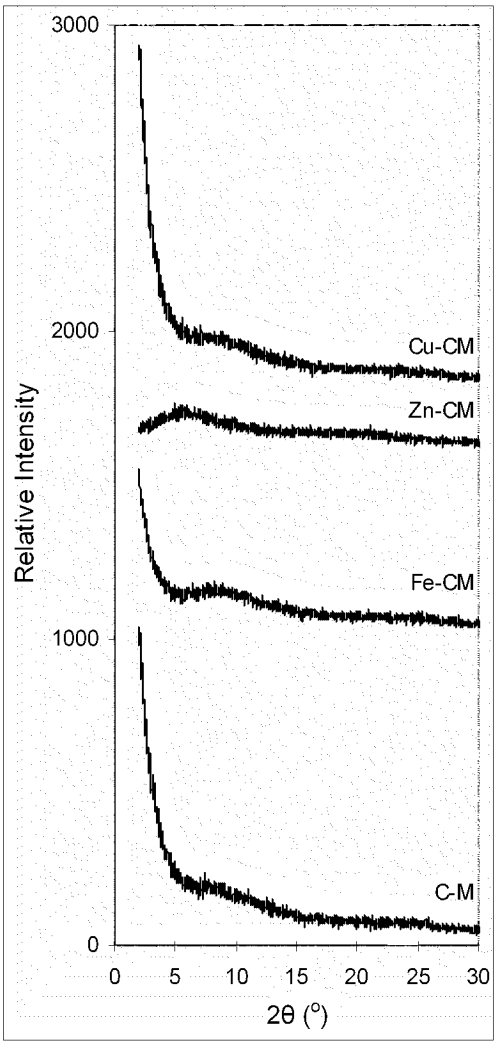

Figure 71: XRD of C-M, Fe-CM, Zn-CM, and Cu-CM

The XRD patterns for C-M, Fe-CM and Cu-CM (Figure 71) show a small peak located around 8.2 °, which corresponds to a d_{001} spacing of 10.8 Å. This indicates that these carbons inherited the layered structure of their clay templates. Such a conclusion was also reached when a natural clay was used as template [25]. Considering that a graphene layer is approximately 3.5 Å thick, those carbons thus consist of the stacking of three graphene layers. On the other hand, Zn-CM has a peak at 5.9 ° corresponding to a

d_{001} spacing of 14.9 Å, which is, as seen previously, a typical value for the pillared clays. That peak could then be the result of some clay template still remaining in Zn-CM. It may seem surprising that a clay would still retain its ordered layered structure after treatment at 900 °C, but the presence of graphene between clay layers has been proven to increase the thermal stability of clay structures, even at so high temperatures [25]. The peak at 5.9 ° in the XRD pattern for Zn-CM would probably overlap with any potential shoulder or peak at 8.2 °. It then seems that all our carbons possess some degree of order, at least on a short scale, with diffraction peaks that are broad and low in intensity.

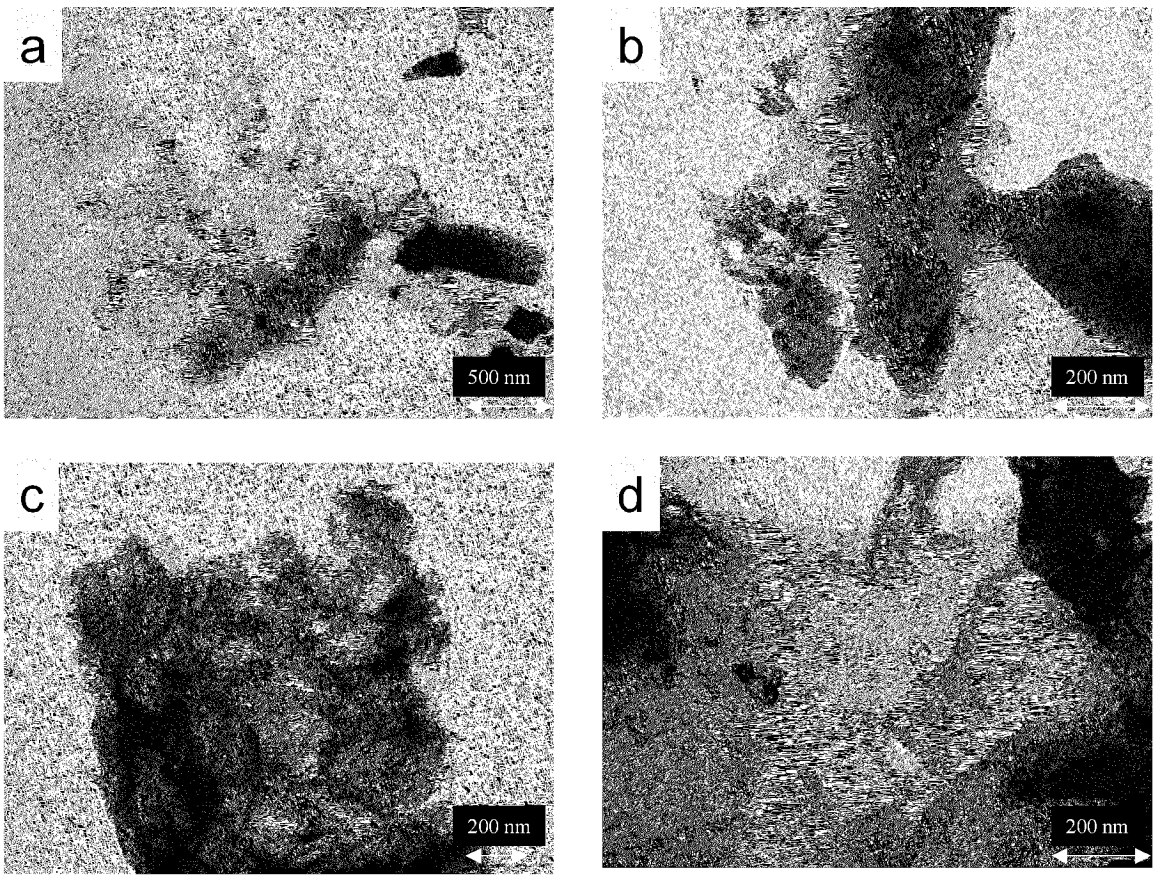

Figure 72: TEM images of C-M (a), Fe-CM (b), Zn-CM (c), and Cu-CM (d)

TEM analysis of the carbon materials (Figure 72) show that they all consist of two carbon phases, one being amorphous with scattered small particles and the other one consisting of large thin layers, whose edges can be distinguished, that are stacked together in a parallel fashion. The former phase is probably the carbon replica of the silica particles flakes previously observed in the SEM pictures of the PCH templates, while the latter phase would correspond to graphene layers that adopt the PCHs layered structure, as already deducted from XRD.

It is likely that this regular parallel stacking of layers only occurs on a short scale and that on a larger scale, as already mentioned, these stacks of carbon form a house-of-cards structure. As a consequence, the porosity of these carbons would consist, on the one hand, of micropores that are located between graphene layers and, on the other hand, of mesopores that are present between stacks of layers or in the amorphous phase. It is noteworthy to mention that the layers in Cu-CM exhibit some holes, which is not the case with the other carbons. This is another indication that some carbon has been consumed by the reduction of copper during the carbonization process. Another interesting feature is the presence of dark particles with a shape of rice grain on the TEM picture for Fe-CM. These particles are most likely the iron species that were detected in that carbon on elemental analysis and XRF. Metal species could only be observed with Fe-CM as it is the only sample with a significant metal content. These iron species were not detected by XRD probably because of their small amount and high degree of dispersion.

When metal-loaded PCHs were used, carbons with only minor amounts of metal form, except in the case of iron. This low metal loading level is due to the strong acid washing that was used for removing the inorganic template. It is possible that a caustic

treatment instead of an acid one would yield carbons with higher metal contents. Iron proved to be particularly resistant to the acid treatment, and it is possible that part of it is present as iron carbide. That iron-loaded carbon could find applications in the adsorption and oxidation of large organic molecules.

4.5. Activated Carbons Bound with Metal-Containing Clays

Fine powders of a wood-based activated carbon WV were shaped into 1-2 mm wide particles by using a natural and untreated bentonite clay BEN whose characteristics are very close to the ones of a montmorillonite clay.

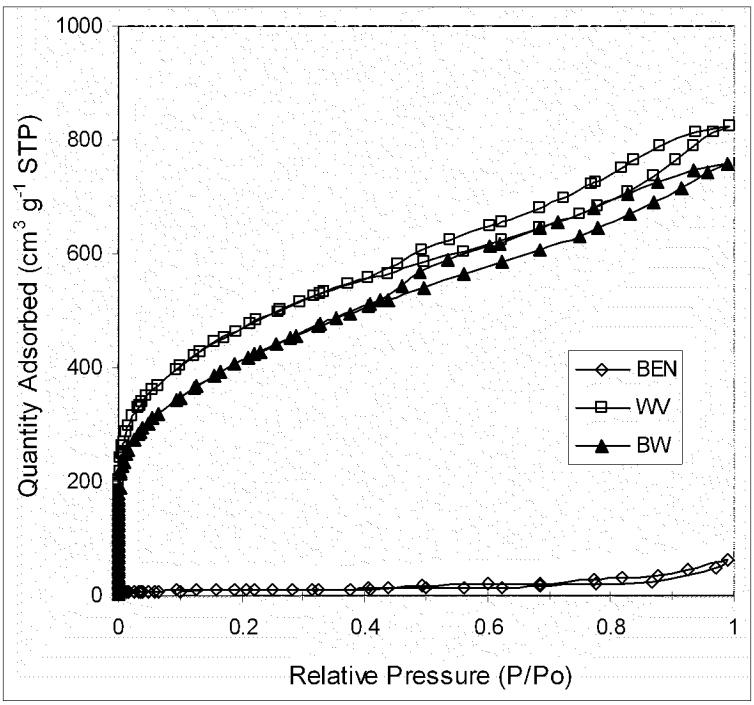

Figure 73: N_2 adsorption-desorption isotherms of BEN, WV, and BW

WV exhibits a type I N_2 adsorption isotherm, which is indicative of a microporous material (Figure 73). Its type H_4 hysteresis loop shows that it also contains mesopores that are open slit-shaped capillaries.

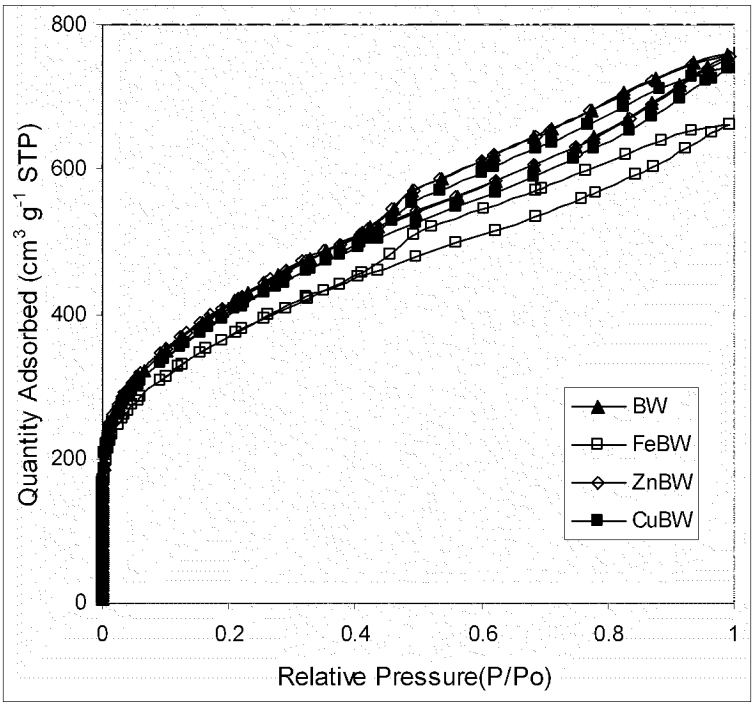

Figure 74: N_2 adsorption-desorption isotherms of BW, FeBW, ZnBW, and CuBW

Table 15: Structural parameters of the materials

	S_{BET} ($m^2 g^{-1}$)	V_{DR} ($cm^3 g^{-1}$)	V_t ($cm^3 g^{-1}$)
BEN	33	0.015	0.095
WV	1623	0.734	1.274
BW	1579	0.567	1.294
FeBW	1293	0.559	1.020
ZnBW	1457	0.620	1.165
CuBW	1413	0.602	1.140

On the contrary, BEN is non-porous. BW, which results from the binding of WV and BEN in a 9:1 ratio, thus it has a lower porosity than WV, as a mass dilution effect of WV by BEN took place. Porosity losses due to that effect are slightly more pronounced when metal-loaded clays, obtained by cation-exchange, serve as binders (Figure 74).

From the structural parameters calculated from the N_2 adsorption-desorption isotherms (Table 15), WV is a highly porous material, with a large micropore volume, while BEN is indeed non-porous. When WV is mixed with BEN, the micropore volume is the most affected parameter: while the surface area only slightly decreases, the micropore volume gets lower by 20%. It then seems that binding WV with BEN blocks the micropores entrances, which may hinder adsorption of molecules into them [114]. Considering the respective sizes of micropores and BEN particles, this pore blocking can only be due to the migration of cations from BEN to the micropores of WV. The porosity loss is slightly more marked with metal-loaded BEN. This may be related to the amount of cations migrating from the clay binder. Indeed, metal cation exchange should result in the presence of some metal cations on the clay outer surface, in addition to the metal cations in the gallery. Thus, more cations can migrate from the clay in the case of metal cation-exchanged BEN than with the unmodified BEN. This would result in more pore blocking in WV when FeB, ZnB, or CuB instead of BEN is used as a binder.

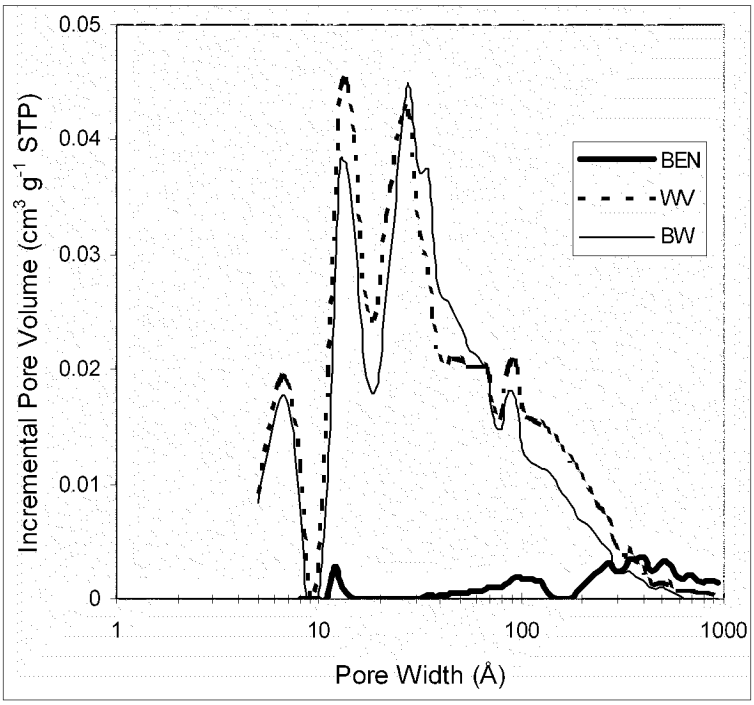

Figure 75: Pore size distributions of BEN, WV, and BW

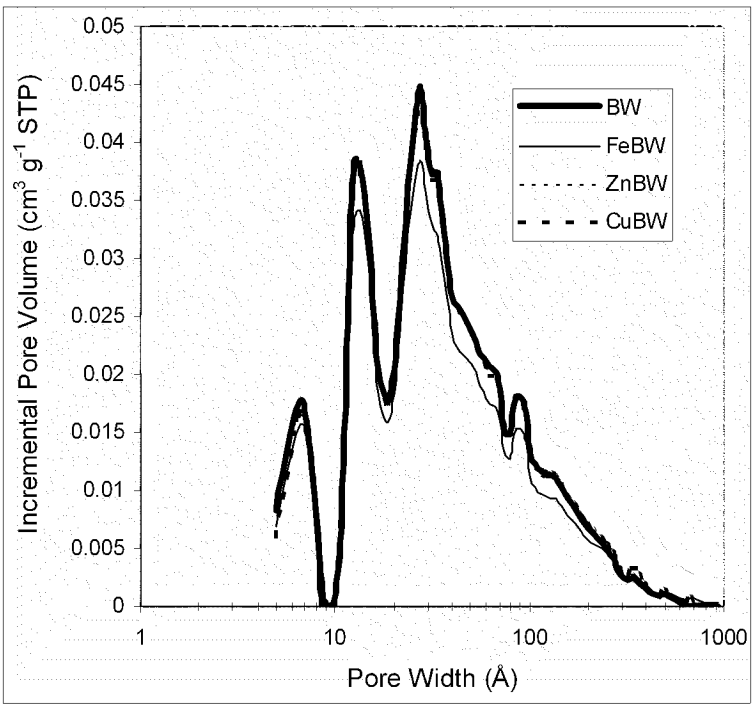

Figure 76: Pore size distributions of BW, FeBW, ZnBW, and CuBW

The pore-blocking phenomenon is most pronounced when iron is used for FeBW: the decrease in structural parameters compared to WV is 50% greater than that for ZnBW and CuBW. That could be due to the probable existence of large iron clusters on the outer surface of FeB.

The PSD of WV (Figure 75) shows that, aside from micropores, this carbon also possesses a significant volume of mesopores, especially in the 20-300 Å range. Its PSD in the micropore region shows two peaks, at 6.8 Å and 13.6 Å. Aside from that, WV has a significant amount of smaller mesopores that are 27.3 Å wide. In comparison, BEN can indeed be considered as nonporous. Mixing those two materials to get BW thus decreases pores of all dimensions.

When BEN is replaced by metal-exchanged clay, materials with similar porosities as WV are obtained (Figure 76), except with iron where one gets a carbon-clay composite with overall lower porosity for reasons previously mentioned.

As porosity is lost upon binding WV with clay, lower capacities for H_2S adsorption are obtained, even when cation-exchanged clays are used, except for the case of copper where the resulting capacity is almost three times the one for WV (Figure 77 and Table 16). This lowering in H_2S adsorption capacities is probably not only to the mass dilution effect, but also to the blocking of carbon pores by species coming from the clay binders. Indeed, these carbon pores contain the chemical species that are active in the process of H_2S adsorption. These active centers are either some basic functions [26, 33] or an inorganic phase such as iron oxide [124].

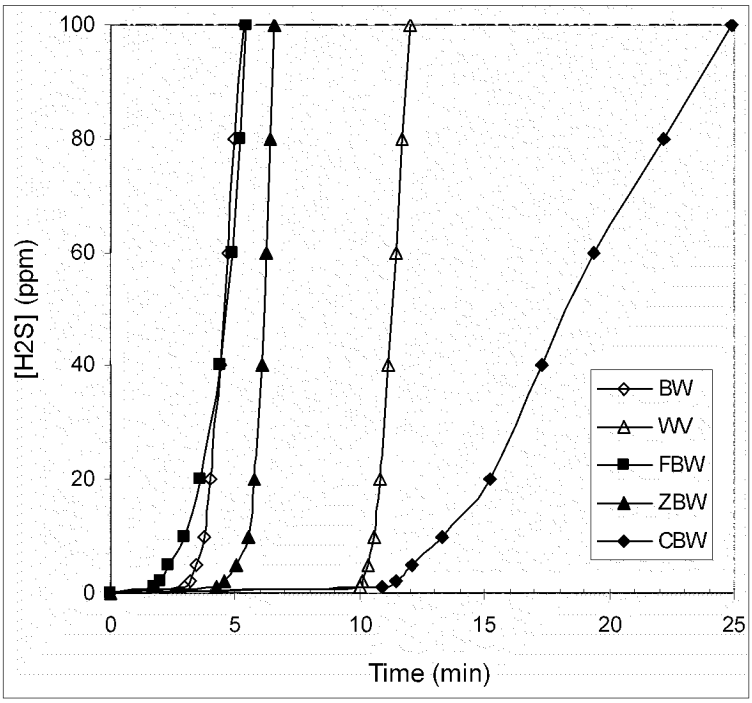

Figure 77: H_2S breakthrough curves of BW, WV, FeBW, ZnBW, and CuBW

Table 16: H_2S capacities and pHs of the (exhausted) carbon samples

	Mass (g)	Breakthrough time (min)	Breakthrough capacity (mg g^{-1})	pH (initial)	pH (exhausted)
WV	1.442	12.0	17.3	6.41	5.58
BW	1.173	5.0	9.4	6.53	6.01
FeBW	1.166	5.0	9.6	3.93	3.74
ZnBW	1.092	6.5	12.5	6.37	5.98
CuBW	1.096	25.0	47.0	6.26	5.80

This would explain why a lower H_2S adsorption capacity than in the case of WV is obtained with FeBW and ZnBW, despite the presence of iron and zinc that have previously been proven to be active for H_2S adsorption.

Nevertheless, the presence of metal in the clay binders gives an improved capacity over BW, even though the actual amount of clay in the final carbon-clay material is low, as only 10% of a binder whose cation-exchange capacity is of around 0.8 mmol/g is used. Only a slight capacity improvement is achieved with iron though. It is possible that in this case, the iron-exchanged clay binder introduces unfavorable conditions for the oxidation of H_2S [26, 33], as its use results in a pH decrease of almost 3 units. Indeed, studies of H_2S adsorption on wood-based carbons suggest that this process is favored in a basic or at least not too acidic environment [32, 33] where dissociation of H_2S and its further oxidation on the carbon surface [114, 125] can take place. That acidity increase for FeBW may be due to the presence of acidic iron species [38, 126] such as $Fe(H_2O)_6^{3+}$ or iron oxides. While a better capacity is reached with zinc, the most improvement happens in the case of copper. This may be due to the high capability of copper to activate oxygen, which further oxidizes hydrogen sulfide [127].

Following H_2S adsorption, the largest decrease in pH of the carbon suspension occurs with WV (Table 16). A decrease in pH after H_2S adsorption/oxidation is usually due to the deposition of H_2S oxidation products such as SO_2 or H_2SO_4 on the surface of the adsorbent [26, 33], the latter being responsible for larger pH drops. Actually, a previous study showed that H_2SO_4 is the main reaction product of H_2S oxidation on non-treated wood-based carbons from Westvaco [114], which is what WV is. With the metal-containing materials, the pH decrease is commensurate with the material's capacity. But even though CuBW has a larger adsorption capacity for H_2S than BW, the pH drop for CuBW is lower than that for BW. This indicates a difference in the nature of the reaction

products between the two materials, with salts and/or elemental sulfur probably forming from CuBW.

Table 17: Structural parameters of the carbons before and after (/E) H_2S adsorption

	S_{BET} ($m^2 g^{-1}$)	V_{DR} ($cm^3 g^{-1}$)	V_t ($cm^3 g^{-1}$)
BW	1579	0.567	1.294
BW/E	1554	0.558	1.283
FeBW	1293	0.559	1.020
FeBW/E	1269	0.559	1.001
ZnBW	1457	0.620	1.165
ZnBW/E	1451	0.604	1.164
CuBW	1413	0.602	1.140
CuBW/E	1282	0.561	1.122

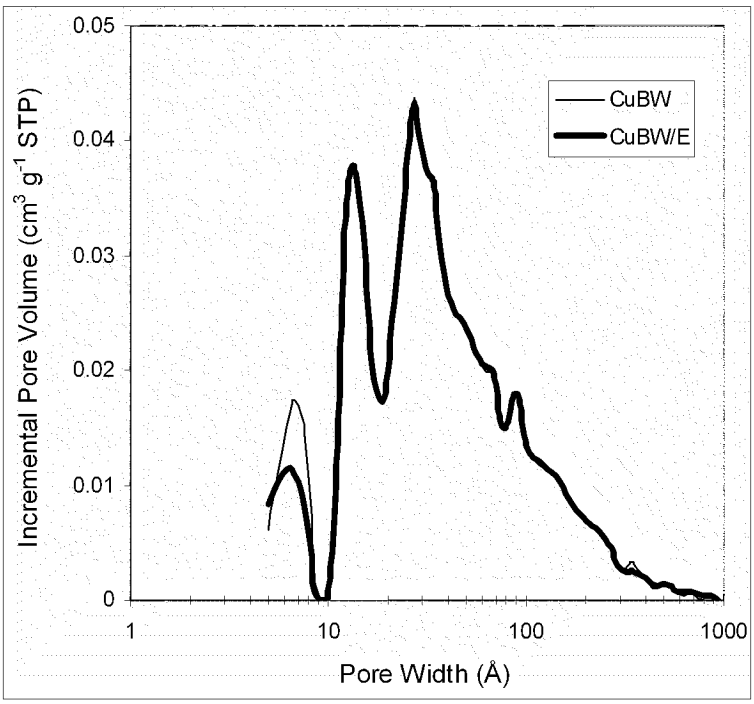

Figure 78: Pore size distributions of CuBW before and after (/E) H_2S adsorption

Despite showing some capacity for the adsorption of H_2S, the porosities of the carbon materials hardly change, except for CuBW that undergoes minute decreases in its surface area (-2%) and micropore volume (-7%) (Table 17). Adsorption and oxidation of H_2S thus takes place in the carbon micropores.

The PSDs of CuBW before and after adsorption (Figure 78) further indicate that those active micropores are the ones smaller than 10Å: these pores are partially filled with reaction products resulting from the adsorption there of H_2S. It is likely that copper cations are present in these small micropores where they can bind to sulfur atoms as a preliminary step to H_2S immobilization and oxidation. The lack of reactivity of zinc toward H_2S can be interpreted through the work of Morse and Luther [128] who showed that the extent of the interaction of a transition metal cation with hydrogen sulfide depends on the rate of the water exchange reaction between the metal cation-water complex and water, which is the first step for sulfide formation (* refers to radiolabeled water):

$$M(H_2O)_6^{2+} + H_2O^* \leftrightarrow M(H_2O)^*(H_2O)_5^{2+} + H_2O \qquad \textbf{(18)}$$

The rate of that reaction with copper is an order of magnitude greater that that for zinc (8×10^8 compared to 3×10^7), that difference being related to d orbitals filling configurations in the metal cation complexes. It was found as well that, in the case of copper, the reaction with hydrogen sulfide is much complex than the one for zinc. With copper, copper (II) is reduced to copper (I) by sulfide, and usually various phases of copper sulfides are formed with Cu/S ratios ranging from 2 to 0.5.

Absence or negligible porosity changes following H_2S adsorption with samples other than CuBW can not only be due to a lack of reactivity but also to the outgassing of the exhausted materials prior to N_2 adsorption. Indeed, if the reaction products on these carbons are weakly adsorbed acidic gases such as SO_2 instead of sulfides and/or sulfur as it seems to be the case with CuBW, then these gases should be desorbed from the materials' surface under the conditions used during the outgassing process (120 ^{o}C, vacuum). Such gases, which are acidic, could also account for the acidity increases observed with these carbons.

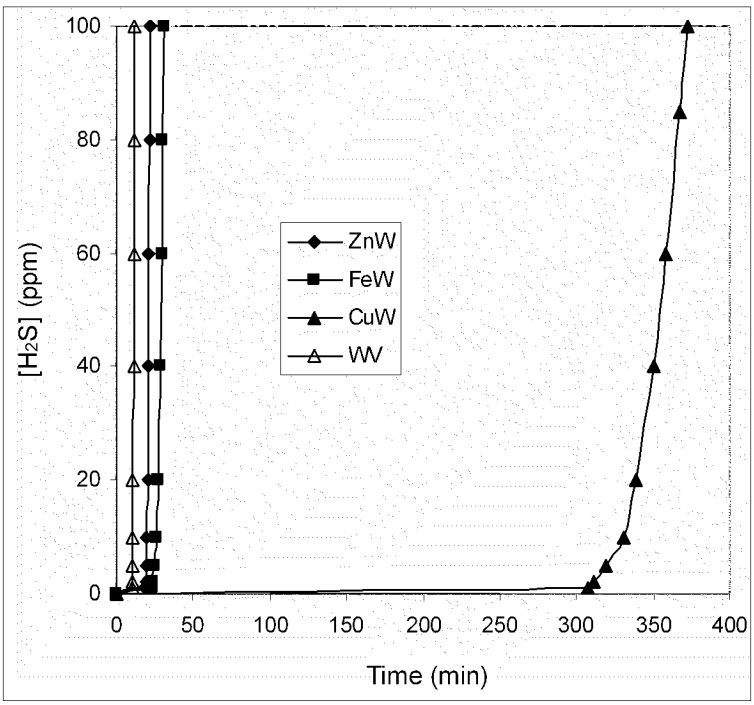

Figure 79: H_2S breakthrough curves of FeW, ZnW, and CuW

Table 18: H_2S capacities and pHs of the (exhausted) impregnated carbons

	Mass (g)	Breakthrough time (min)	Breakthrough capacity (mg g^{-1})	pH (initial)	pH (exhausted)
WV	1.442	12.0	17.3	6.41	5.58
FeW	1.641	31.5	39.6	6.53	6.01
ZnW	1.476	22.0	30.9	5.99	5.45
CuW	1.561	372.5	496.6	3.71	2.76

Table 19: Metal content and amount of H_2S adsorbed of the carbons

	Metal content (%)	Metal content (mmol g^{-1})	H_2S adsorbed (mmol g^{-1})
FeBW	0.06	<0.01	0.28
ZnBW	0.26	0.04	0.37
CuBW	0.57	0.09	1.38
FeW	1.32	0.24	1.16
ZnW	4.32	0.66	0.91
CuW	2.39	0.38	14.61

To better understand the role of metal cations in the adsorption of H_2S, WV was impregnated with the same metal cations and tested for H_2S adsorption, as metal cation impregnation is a common way to improve the adsorptive properties of carbons toward toxic gases [129]. Results of the breakthrough tests are reported in Figure 79 and Table 18, while the materials metal contents (estimated by XRF) and quantities of adsorbed H_2S (determined from the breakthrough tests) are featured in Table 19. Despite a comparable metal content, CuW has a capacity for H_2S adsorption that is more than ten times the ones for FeW and ZnW. Adsorption/immobilization of H_2S should then be radically different on CuW compared to what happens on FeW and ZnW. That difference in the H_2S removal process was already suggested from the changing slope in the breakthrough

curve for CuBW, while the slopes for FeBW and ZnBW remained practically constant. Several different chemical reactions thus seem to take place in the case of CuBW, with probably formation of adsorption products that favor further adsorption of H_2S, as the constantly decreasing slope of the breakthrough curve for CuBW seems to indicate.

Table 20: Structural parameters of the (exhausted) impregnated carbons

	S_{BET} ($m^2\ g^{-1}$)	V_{DR} ($cm^3\ g^{-1}$)	V_t ($cm^3\ g^{-1}$)
WV	1623	0.734	1.276
FeW	1430	0.297	1.170
FeW/E	1350	0.277	1.102
ZnW	1470	0.320	1.189
ZnW/E	1400	0.309	1.125
CuW	1470	0.325	1.169
CuW/E	500	0.060	0.509

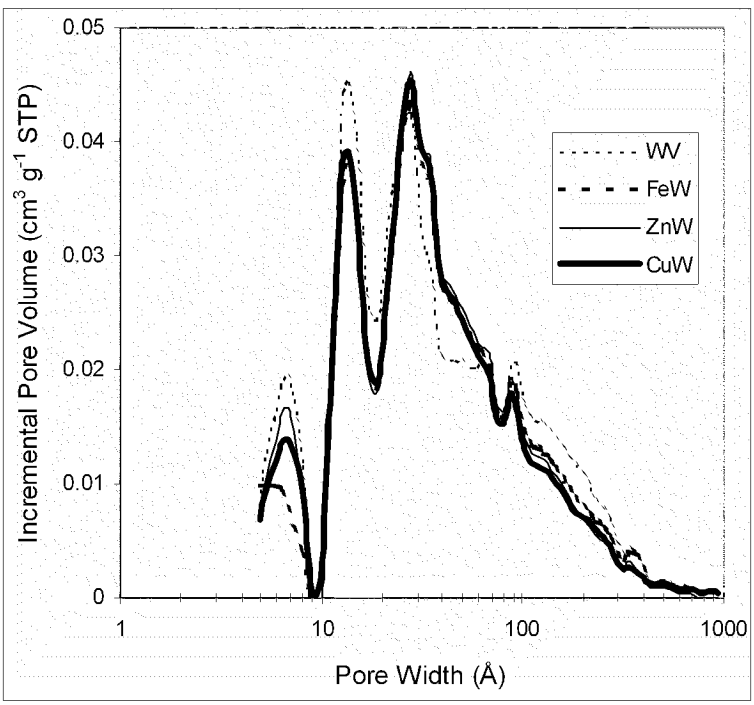

Figure 80: Pore size distributions of WV, FeW, ZnW, and CuW

The metal contents of the carbon-clay materials are an order of magnitude smaller than that for the impregnated carbons. On the other hand, structural parameters (Table 20) and PSDs deducted from N_2 adsorption-desorption isotherms (Figure 80) show that metal cation-impregnation induces porosity changes compared to WV that are similar to the ones when clay binders are used: with impregnation, the surface area decreases by about 10% and the micropore volume gets about 20% smaller. But while the changes with clay binders were the result of the combination of mass dilution effect and cation migration, it is only due to metal cation deposition in the case of impregnation. The PSDs of the impregnated carbons show that the metal cations are deposited in pores of all kinds, so their degree of dispersion in the carbons should be high.

Even when WV is impregnated with metal cations, copper shows far superior catalytic activity towards the adsorption of H_2S compared to iron and zinc. When these three metals are present in equivalent amounts, the efficiency of the copper centers (ratio of number of moles of H_2S adsorbed to the number of metal cations) is 10 and 30 times higher than that for respectively iron and zinc. Nevertheless, the differences in efficiencies between the metal- containing carbon-clay samples are not as drastic as with the impregnated carbons, even though a similar trend is observed. It is possible that when the metal content is particularly low as it is the case with the carbon-clay materials, the role of the carbon surface predominates and the presence of metal cations is much less important for the adsorption of H_2S.

When comparing CuW to CuBW, it turns out that even though the copper content of CuW is only four times higher than that for CuBW, the capacity of CuBW is ten times

smaller than that for CuW. This indicates that in CuBW, only a fraction of the total copper there plays an active role in the adsorption of H_2S. Indeed, when BEN is exchanged with a metal cation, most of the new cations are located between the clay layers, while a small fraction of them are adsorbed on the outer clay surface. It is mainly the latter ones that can migrate from the outer clay surface to the carbon micropores, since the interlayer cations must remain in the clay to insure electrical neutrality. As a consequence, only that small fraction can interact with H_2S. On the contrary, all the copper present in CuW is available for that process, which would explain the difference in performance between CuW and CuBW.

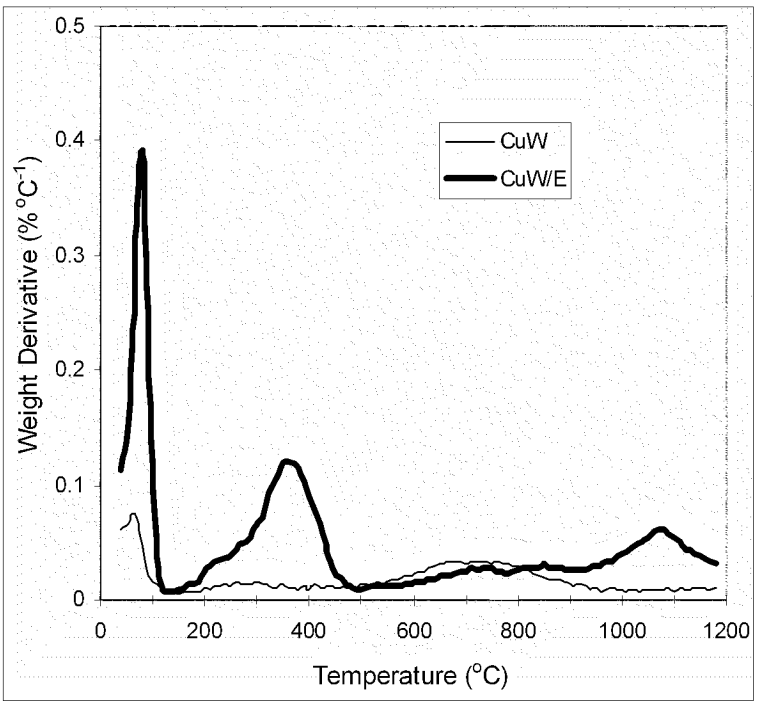

Figure 81: DTG curves of CuW(/E)

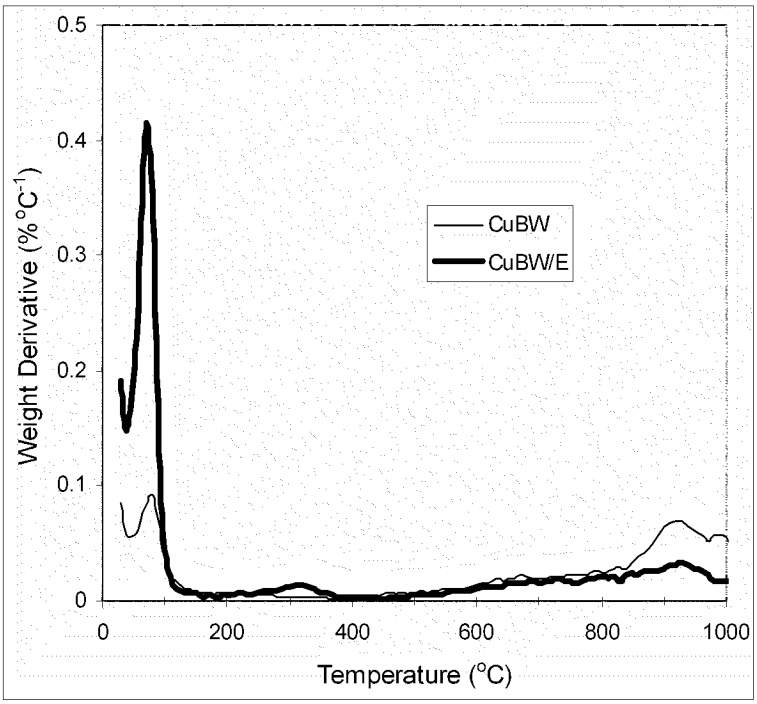

Figure 82: DTG curves of CuBW(/E)

Giving the best performances, the copper samples were the main focus for thermal analysis in nitrogen. CuW/E and CuBW/E have a common peak between 200 °C and 500 °C (Figures 81 and 82). On a closer look, the peak for CuW/E actually consists of two peaks, one smaller at 250 °C and another one larger at 350 °C. The former is attributed to the decomposition of H_2SO_4 or the desorption of strongly adsorbed SO_2 (that gas was detected in the effluent stream from the TA instrument), while the latter is likely due to the presence of elemental sulfur (H_2S was detected in the effluent gas). The weight loss in this temperature range (taking into account the weight loss of the initial material and normalizing for water content) for CuW/E shows that sulfur represents 15% of its mass. According to the breakthrough tests results, that is only one third of the total amount of sulfur adsorbed on CuW. The same discrepancy is found for CuBW. It is possible that part of that "missing" sulfur is in the form of Cu_2S that would be responsible

for the peak at 1,080 °C for CuW/E [116]. But that would still not totally account for all the sulfur that should be present in CuW/E. Another explanation could then be that some elemental sulfur formed by H_2S adsorption was oxidized by oxygen from air to SO_2. That weakly adsorbed SO_2 would leave the surface as the gas stream passes through the column. Indeed, both with CuBW and CuW, SO_2 was found to be present in the outlet stream even before H_2S was detected. Furthermore, it is possible that, in the presence of carbon and nitrogen, CuSCN formed during the heating process of thermal analysis and that carbon reduced copper at around 1,000 °C.

All those results once again underline the particular efficiency of copper in fixing H_2S, forming SO_2 and sulfur in the process. The effect of copper is likely to activate oxygen in the process of H_2S oxidation. As negative charges due to free valences exist at the edges of graphene layers, copper cations are most probably present there, where they could form dicopper-dioxygen adducts [127]. Oxygen would be activated through the splitting of O-O bonds in these adducts. That oxygen could oxidize the sulfide ions present in the material's water film as a result H_2S dissolution and dissociation in it. Afterward, the mechanism would happen according to what has already been proposed for the oxidation of H_2S on activated carbons [26, 33, 114], with formation of elemental sulfur, SO_2/H_2SO_4, and water as oxidation products. Cu^{2+} then activates oxygen through its reduction to Cu^{+} and copper (I) sulfide is formed in the process. The oxidation of H_2S would stop when no more activating agents are present. Another limiting factor in the process of H_2S oxidation would be the stability of the dicopper-dioxygen adducts that sharply decreases with temperature [127]. Indeed, a temperature rise can occur during the immobilization of H_2S as heat resulting from adsorption is evolved. Kobayashi and

Flytzani-Stephanopoulos have also invoked that possibility of copper activating oxygen in their study of the reduction and sulfidation kinetics of copper-modified cerium oxide [130].

Copper-containing clays can thus serve as binders for fine powdered carbons, and the resulting materials, aside from better mechanical properties, exhibit better capacities the adsorption/oxidation of hydrogen sulfide compared to the original carbons. Spent clays, used for the adsorption of copper cations, could then be recycled as binders for carbons adsorbing hydrogen sulfide. This improvement in hydrogen sulfide adsorption capacity is due to the migration of copper cations from the clay to the carbon micropores. The role of that copper is to activate oxygen, which allows the oxidation of hydrogen sulfide into sulfur and sulfur dioxide. As a result, the oxidation products are deposited on the carbon surface, mainly in the micropores. Hydrogen sulfide oxidation happens until all the copper cations are bound to sulfur. Since iron (III) and zinc have lower rates of water exchange than copper and are unable to activate oxygen under the used conditions, clays containing those metals do not improve the hydrogen sulfide capacity of the carbons they bind. The main inconvenience related to the presence of copper in a clay binder is the formation of weakly adsorbed SO_2, which is another pollutant.

5. CONCLUSION

It has been shown that different adsorbents with metals as active species can be obtained from a natural clay, either by chemically modifying it or by using it as a template to prepare carbonaceous carbons. Overall, materials with potential applications for the adsorption of various species have been obtained. Indeed, not only do these materials differ in their nature (inorganic or carbonaceous), but they also have contrasting features in their porosity and in their active metal species. While the synthesized adsorbents are all microporous, their degree of microporosity and mesoporosity vary, along with their micropore sizes. As for the metal species, their identity, accessibility, location, and degree of dispersion, change from one sample to another.

Exchanging sodium in the natural clay with hydrated cations of Fe^{3+}, Zn^{2+}, or Cu^{2+} does not generate new porosity in the material. While metal cations are present both in the clay gallery and on the outer clay surface, only the external cations prove to be accessible, as the narrow clay interlayer spacing prevents the inner cations from participating in any adsorption process. In contrast, when the natural clay is exchanged with an iron oxocation, some porosity is created between the clay layers, as the oxocation penetrates the gallery and deposits on the outer surface. But despite larger porosity, the thus-synthesized clay has much less iron available for adsorption than its iron cation-containing counterpart, as the oxocation is present under the form of large clusters, which limits the amount of surface iron that can be active for adsorption.

Clays exchanged with hydrated metal cations can also serve as binders of powdered porous carbons. Such clays being nonporous, the resulting clay-carbon composite materials exhibit an overall lower porosity compared to the original carbons. However the presence of metal cations in the clay can yield a better adsorbing material. Indeed, during the blending of the two materials, metal cations migrate from the clay to the carbon micropores, which creates sites where adsorption could be favored, as porosity and adsorption affinities toward metal species are combined.

Porosity can be formed within the clay gallery by intercalating the clay with stable metal oxides. When alumina pillars are introduced, significant microporosity is present between the clay layers, with pore widths of around 10 Å. Loading iron, zinc, or copper cations in pillared clays improves the adsorbing properties of these materials, as most of the loaded metal can interact with adsorbate molecules, either in the gallery or on the outer surface. In the case of iron, the amount of cations in the gallery is so large that these cations cause clogging of the pillared clay micropores. As a result, only a small fraction of these iron species clogging the micropores can take part in adsorption processes. In addition, iron apparently damages the pillared and layered structure of the materials. In contrast, copper is present in a highly dispersed state in the material's pores, so most of the copper present in the material is available for adsorption.

Materials with even larger microporosities than those of pillared clays are obtained through the introduction of silica with the help of organic surfactants. The role of the surfactants is to insure the formation of silica in large quantities within the clay gallery. The resulting porous clay heterostructures exhibits micropores whose widths are around 20 Å. When iron, zinc, or copper cations are loaded into these materials, a slight

microporosity loss occurs while additional mesoporosity appears. It is thought to be due to the deposition of silica initially present in the gallery on the outer surface, a process induced by cation-exchange. Nevertheless, the metal species in the porous clay heterostructures have a limited accessibility for potential adsorbate molecules, as carbon deposits resulting from the calcination of the surfactants during the materials' preparation cover them.

These porous clay heterostructures nevertheless served as inorganic templates for the synthesis of carbonaceous materials. The final carbons prove to be partial replicas of their models, with micropores of identical sizes as those in the templates. But overall, the carbons have a lower microporosity and a higher mesoporosity than their inorganic models. This is attributed to the particular structural organization of the carbons that, unlike the porous clay heterostructures, possess no long-range order. However these carbons show some short-range order, with the parallel stacking of a few graphene layers. It is very likely that these graphene stacks form a house-of-cards structure on a larger scale. Thus, in these carbons, while micropores are present between graphene layers, mesopores are located between graphene stacks as voids. The amounts of loaded metal in the carbons are particularly low, as a result of strong acid treatment during the carbons preparation. Of the three metals used, only iron is present in significant quantity as it formed acid-resistant species. Carbons synthesized in such a fashion could find applications in the oxidative adsorption of large organic molecules, as they feature wide metal-containing micropores.

6. REFERENCES

1. Brown T.L., LeMay H.E. Jr., Bursten B.E. *Chemistry: The Central Science (9th ed.)*; Pearson Education: Upper Saddle River, NJ **2003**.
2. Bond G.C. *Heterogeneous Catalysis*; Clarendon Press: Oxford, **1974**.
3. Thomas J.M., Thomas W.J. *Principles and Practice of Heterogeneous Catalysis*; VCH: New York, NY **1996**.
4. Sing K.S.W., Everett D.H., Haul R.A.W., Moscou L., Pierotti R.A., Rouquerol J., Siemieniewska T. *Reporting Physisorption Data for Gas/Solid Systems with Special Reference to the Determination of Surface Area and Porosity (Recommendations 1984)*; Pure Appl. Chem. **1985**, *57*, 603.
5. Lippens B.C., de Boer J.H. *Studies on Pore Systems in Catalysts: V. The t Method*; J. Catal. **1965**, 4, 319.
6. Gregg S.J., Sing K.S.W. *Adsorption, Surface Area and Porosity*; Academic Press: New York, NY **1982**.
7. Yang R.T., Baksh M.S.A. *Pillared Clays as a New Class of Sorbents for Gas Separation*; AIChE J. **1991**, *37*, 679.
8. Gil A., Montes M. *Analysis of the Microporosity in Pillared Clays*; Langmuir **1994**, *10*, 291.
9. Androutsopoulos G.P., Salmas C.E. *A New Model for Capillary Condensation-Evaporation Hysteresis Based on a Random Corrugated Pore Structure Concept: Prediction of Intrinsic Pore Size Distributions. 1. Model Formulation*; Ind. Eng. Chem. Res. **2000**, *39*, 3747.

10. Olivier J.P., Occelli M.L. *Surface Area and Microporosity of a Pillared Interlayered Clay (PILC) from a Hybrid Density Functional Theory (DFT) Method*; J. Phys. Chem. B **2001**, *105*, 623.

11. Horvath G., Kawazoe K. *Method for the Calculation of Effective Pore Size Distribution in Molecular Sieve Carbon*; J. Chem. Engn. Jap. **1983**, *16*, 470.

12. Ohtsuka K. *Preparation and Properties of Two-Dimensional Microporous Pillared Interlayered Solids*; Chem. Mater. **1997**, *9*, 2039.

13. Zhu H.Y., Ding Z., Barry J.C. *Porous Solids from Layered Clays by Combined Pillaring and Templating Approaches*; J. Phys. Chem. B **2002**, *106*, 11420.

14. Hutson N.D., Gualdoni D.J., Yang, R.T. *Synthesis and Characterization of the Microporosity of Ion-Exchanged Al_2O_3-Pillared Clays*; Chem. Mater. **1998**, *10*, 3707.

15. Gil A., Montes M. *Metathesis of Propene on Molybdenum-Alumina-Pillared Montmorillonite*; Ind. Eng. Chem. Res. **1997**, *36*, 1431.

16. *DFT Plus Models Library: User's Guide V2.02*; Micromeritics Instrument Corporation: Norcross, GA **2003**.

17. Tarazona P. *Free-Energy Density Functional for Hard Spheres*; Phys. Rev. A **1985**, *31*, 2672.

18. Tarazona P. *Erratum: Free-Energy Density Functional for Hard Spheres*; Phys. Rev. A **1985**, *32*, 3148.

19. Olivier J.P., Occelli M.L. *Surface Area and Microporosity of a Pillared Interlayered Clay (PILC) from a Hybrid Density Functional Theory (DFT) Method*; J. Phys. Chem. B **2001**, *105*, 5358.

20. Jaroniec M., Kruk M., Olivier J.P. *Standard Nitrogen Adsorption Data for Characterization of Nanoporous Silicas*; Langmuir **1999**, *15*, 5410.

21. Clifford D., Subramonian S., Sorg T.J. *Water Treatment Processes. III. Removing Dissolved Inorganic Contaminants from Water*; Environ. Sci. Technol. **1986**, *20*, 1072.

22. Bandosz T.J. *Fundamentals of Adsorption 6*; Elsevier: Paris, **1998.**

23. Cheremisinoff P.N., Ellerbusch F. *Carbon Adsorption Handbook*; Ann Arbor Science: Ann Arbor, MI **1978**.

24. *Kirk-Othmer Encyclopedia of Chemical Technology (2^{nd} ed.), vol. 4*; Wiley: New York, NY **1964**.

25. Bakandritsos A., Steriotis Th., Petridis D. *High Surface Area Montmorillonite-Carbon Composites and Derived Carbons*; Chem. Mater. **2004**, *16*, 1551.

26. Adib F., Bagreev A., Bandosz T.J. *Analysis of the Relationship between H_2S Removal Capacity and Surface Properties of Unimpregnated Activated Carbons*; Environ. Sci. Technol. **2000**, *34*, 686.

27. Dahn J.R., Zheng T., Liu Y., Xue J.S. *Mechanisms for Lithium Insertion in Carbonaceous Materials*; Science **1995**, *270*, 590.

28. Xiao B., Thomas K.M. *Competitive Adsorption of Aqueous Metal Ions on an Oxidized Nanoporous Activated Carbon*; Langmuir **2004**, *20*, 4566.

29. Xiao B., Thomas K.M. *Adsorption of Aqueous Metal Ions on Oxygen and Nitrogen Functionalized Nanoporous Activated Carbons*; Langmuir **2005**, *21*, 3892.

30. Jia Y.F., Xiao B., Thomas K.M. *Adsorption of Metal Ions on Nitrogen Surface Functional Groups in Activated Carbons*; Langmuir **2002**, *18*, 470.

31. Yantasee W., Lin Y., Fryxell G.E., Alford K.L., Busche B.J., Johnson C.D. *Selective Removal of Copper(II) from Aqueous Solutions Using Fine-Grained Activated Carbon Functionalized with Amine*; Ind. Eng. Chem. Res. **2004**, *43*, 2759.

32. Adib F., Bagreev A., Bandosz T.J. *Effect of Surface Characteristics of Wood-Based Activated Carbons on Adsorption of Hydrogen Sulfide*; J. Colloid Interface Sci. **1999**, *214*, 407.

33. Adib F., Bagreev A., Bandosz T.J. *Effect of pH and Surface Chemistry on the Mechanism of H_2S Removal by Activated Carbons*; J. Colloid Interface Sci. **1999**, *216*, 360.

34. Bagreev A., Rahman H., Bandosz T. *Study of H_2S Adsorption and Water Regeneration of Spent Coconut-Based Activated Carbon*; J. Environ. Sci. Technol. **2000**, *34*, 4587.

35. Bagreev A., Locke D.C., Bandosz T. *H_2S Adsorption/Oxidation on Adsorbents Obtained from Pyrolysis of Sewage-Sludge-Derived Fertilizer Using Zinc Chloride Activation*; J. Ind. Eng. Chem. Res. **2001**, *40*, 3502.

36. Bagreev A., Bandosz T.J. *H_2S Adsorption/Oxidation on Materials Obtained Using Sulfuric Acid Activation of Sewage Sludge-Derived Fertilizer*; J. Colloid Interface Sci. **2002**, *252*, 188.

37. Bandosz T.J., Jagiello J., Putyera K., Schwarz J.A. *Pore Structure of Carbon-Mineral Nanocomposites and Derived Carbons Obtained by Template Carbonization*; Chem. Mater. **1996**, *8*, 2023.

38. Baes Jr. C.F., Mesmer R.E. *The Hydrolysis of Cations*; Wiley: New York, NY **1976**.

39. Ryoo R., Joo S.H., Jun S. *Synthesis of Highly Ordered Carbon Molecular Sieves via Template-Mediated Structural Transformation*; J. Phys. Chem. B **1999**, *103*, 7743.

40. Meyers C.J., Shah S.D., Patel S.C., Sneeringer R.M., Bessel C.A., Dollahon N.R., Leising R.A., Takeuchi E.S. *Templated Synthesis of Carbon Materials from Zeolites (Y, Beta, and ZSM-5) and a Montmorillonite Clay (K10): Physical and Electrochemical Characterization*; J. Phys. Chem. B **2001**, *105*, 2143.

41. Bakandritsos A., Kouvelos E., Steriotis Th., Petridis D. *Aqueous and Gaseous Adsorption from Montmorillonite-Carbon Composites and from Derived Carbons*; Langmuir **2005**, *21*, 2349.

42. Kim Y., Kim C., Choi I., Rengaraj S., Yi J. *Arsenic Removal Using Mesoporous Alumina Prepared via a Templating Method*; Environ. Sci. Technol. **2004**, *38*, 924.

43. Velu S., Song C., Engelhard M.H., Chin Y.-H. *Adsorptive Removal of Organic Sulfur Compounds from Jet Fuel over K-Exchanged NiY Zeolites Prepared by Impregnation and Ion Exchange*; Ind. Eng. Chem. Res. **2005**, *44*, 5740.

44. Hernandez-Maldonado A.J., Yang R.T. *Desulfurization of Commercial Liquid Fuels by Selective Adsorption via π-Complexation with Cu(I)-Y Zeolite*; Ind. Eng. Chem. Res. **2003**, *42*, 123.

45. Szostak R. *Molecular Sieves Principles of Synthesis and Identification*; Van Nostrand Reinhold: New York, NY **1989**.

46. Cheng L.S., Yang R.T. *A New Class of Non-Zeolitic Sorbents for Air Separation: Lithium Ion Exchanged Pillared Clays*; Ind. Eng. Chem. Res. **1995**, *34*, 2021.

47. Yang R.T., Baksh M.S.A. *Pillared Clays as a New Class of Sorbents for Gas Separation*; AIChE J. **1991**, *37*, 679.

48. Guan Y., Liu Y., Wu W., Sun K., Li Y., Ying P., Feng Z., Li C. *Dibenzodioxin Adsorption on Inorganic Materials*; Langmuir **2005**, *21*, 3877.

49. Iretskaya S., Mitchell M.B. *Promoting Effect of Chloride on the SO_2 Adsorption Capacity and Adsorption Rate of Alumina-Supported Copper Oxide Adsorbents: Thermogravimetric and Infrared Studies*; J. Phys. Chem. B **2003**, *107*, 4955.

50. Kresge C.T., Leonowicz M.E., Roth W.J., Vartuli J.C., Beck J.S. *Ordered Mesoporous Molecular Sieves Synthesized by a Liquid-Crystal Template Mechanism*; Nature **1992**, *359*, 710.

51. Polverejan M., Pauly T.R., Pinnavaia T.J. *Acidic Porous Clay Heterostructures (PCH): Intragallery Assembly of Mesoporous Silica in Synthetic Saponite Clays*; Chem. Mater. **2000**, *12*, 2698.

52. Sayari A., Hamoudi S., Yang Y. *Applications of Pore-Expanded Mesoporous Silica. 1. Removal of Heavy Metal Cations and Organic Pollutants from Wastewater*; Chem. Mater. **2005**, *17*, 212.

53. Mercier L., Detellier C. *Preparation, Characterization, and Applications as Heavy Metals Sorbents of Covalently Grafted Thiol Functionalities on the Interlamellar Surface of Montmorillonite*; Environ. Sci. Technol. **1995**, *29*, 1318.

54. Ravindran V., Stevens M.R., Badriya B.N., Pirbazari M. *Modeling the Sorption of Toxic Metals on Chelant-Impregnated Adsorbent*; AIChE J. **1999**, *45*, 1135.

55. Hernando M.J., Pesquera C., Blanco C., González F. *Synthesis, Characterization, and Catalytic Properties of Pillared Montmorillonite with Aluminum/Cerium Polyoxocations*; Chem. Mater. **2001**, *13*, 2154.

56. Sayari A. *Catalysis by Crystalline Mesoporous Molecular Sieves*; Chem. Mater. **1996**, *8*, 1840.

57. Hernando M.J., Pesquera C., Blanco C., González F. *Comparative Study of the Texture of Montmorillonites Pillared with Aluminum and Aluminum/Cerium*; Langmuir **2001**, *17*, 5156.

58. Moore D.M., Reynolds R.C., Jr. *X-Ray Dif fraction and the Identification and Analysis of Clay Minerals (2nd ed.)*; Oxford University Press: New York, NY **1997**.

59. Zhu H.Y., Zhu Z.H., Lu G.Q. *Controlled Doping of Transition Metal Cations in Alumina Pillared Clays*; J. Phys. Chem. B **2000**, *104*, 5674.

60. Grim R.E. *Clay Mineralogy (2nd ed.)*; Mc Graw-Hill: New York, NY **1968**.

61. Pusch R. *Use of Bentonite for Isolation of Radioactive Waste Products*; Clay Minerals **1992**, *27*, 353.

62. Schoonheydt R.A., Leeman H., Scorpion A., Lenotte I., Grobet P. *The Al Pillaring of Clays. Part II. Pillaring with* $[Al_{13}O_4(OH)_{24}(H_2O)_{12}]^{7+}$*;* Clays Clay Miner. **1994**, *42*, 518.

63. Chen J.P., Hausladen M.C., Yang R.T. *Delaminated* Fe_2O_3*-Pillared Clay: Its preparation, Characterization, and Activities for Selective Catalytic Reduction of NO by* NH_3; J. Catal. **1995**, *151*, 135.

64. Barrer R.M., MacLeod D.M. *Activation of Montmorillonite by Ion Exchange and Sorption Complexes of Tetra-Alkylammonium Montmorillonites*; Trans. Faraday Soc. **1955**, *51*, 1290.

65. Brindley G.W., Sempels R.E. *Preparation and Properties of Some Hydroxy-aluminum Beidellites*; Clay Miner. **1977**, *12*, 229.

66. Lahav N., Shani U., Shabtai J. *Cross-linked smectites. I. Synthesis and properties of hydroxy-aluminum-montmorillonite*; Clays Clay Miner. **1978**, *26*, 107.

67. Yamanaka S., Brindley G.W. *High Surface Area Solids Obtained by Reaction of Montmorillonite with Zirconyl Chloride*; Clays Clay Miner. **1979**, *27*, 119.

68. Plee D., Borg F., Gatineau L., Fripiat J.J. *High-Resolution Solid-State* ^{27}Al *and* ^{29}Si *Nuclear Magnetic Resonance Study of Pillared Clays*; J. Am. Chem. Soc. **1985**, *107*, 2362.

69. Gil A., Grange P. *Comparison of the Microporous Properties of an Alumina Pillared Montmorillonite and an Activated Carbon from Nitrogen Adsorption at 77 K*; Langmuir **1997**, *13*, 4483.

70. Jamis J., Drljaca A., Spiccia L., Smith T.D. *Infrared Spectroscopic Study of the Occupation of Hydrogen Cyanide Receptor Sites of Metal-Oxide Pillared Clays by Hydrocarbons*; Chem. Mater. **1995**, *7*, 2078.

71. Sterte J.P. *Synthesis and Properties of Titanium Oxide Cross-Linked Montmorillonite*; Clays Clay Miner. **1986**, *34*, 658.

72. Govea L.V., Steinfink H. *Thermal Stability and Magnetic Properties of Fe-Polyoxocation Intercalated Montmorillonite*; Chem. Mater. **1997**, *9*, 849.

73. Occelli M.L., Lester J.E. *Nature of Active Sites and Coking Reactions in a Pillared Clay Mineral*; Ind. Eng. Chem. Prod. Res. Dev. **1985**, *24*, 27.

74. Baksh M.S., Kikkinides E.S., Yang R.T. *Characterization by Physisorption of a New Class of Microporous Adsorbents: Pillared Clays*; Ind. Eng. Chem. Res. **1992**, *31*, 2181.

75. Choy J.H., Jung H., Han Y.S., Yoon J.B., Shul Y.G., Kim H.J. *New CoO-SiO_2-Sol Pillared Clays as Catalysts for NO_x Conversion*; Chem. Mater. **2002**, 14, 3823.

76. Baksh M.S.A., Yang R.T. *Unique Adsorption Properties and Potential Energy Profiles of Microporous Pillared Clays*; AIChE J. **1992**, *38*, 1357.

77. Cheng L.S., Yang R.T. *Improved Horvath-Kawazoe Equations Including Spherical Pore Models for Calculating Micropore Size Distribution*; Chem. Eng. Sci. **1994**, *49*, 2599.

78. Saito A., Foley H.C. *Curvature and Parametric Sensitivity in Models for Adsorption in Micropores*; AIChE J. **1991**, *37*, 429.

79. Thomas S.M., Bertrand J.A., Occelli M.L., Huggins F., Gould S.A.C. *Microporous Montmorillonites Expanded with Alumina Clusters and M[(μ-*

OH)Cu(μ-OCH$_2$CH$_2$NEt$_2$)]$_6$(ClO$_4$)$_3$, (M = Al ,Ga, and Fe), or Cr[(μ-OCH$_3$)(μ-OCH$_2$CH$_2$NEt$_2$)CuCl]$_3$ Complexes; Inorg. Chem. **1999**, *38*, 2098.

80. Thomas S., Bertrand J.A., Occelli M.L. *Incorporation of Chelated Cobalt Complexes and Polyoxocations of Aluminum in Montmorillonite*; Chem. Mater. **1999**, *11*, 184.
81. Mitchell I.V. *Pillared Layered Structures, Current Trends and Applications*; Elsevier Applied Science: London, **1990**.
82. Johansson G. *On the Crystal Structures of some Basic Aluminium Salts*; Acta Chem. Scand. **1960**, *14*, 771.
83. McBride M.B. *Minerals in the Soil Environment (2nd ed.)*; Soil Science Society of America: Madison, WI **1989.**
84. He M.-Y., Liu Z., Min E. *Acidic and Hydrocarbon Catalytic Properties of Pillared Clay*; Catal. Today **1988**, *2*, 321.
85. Han S., Kim M., Hyeon T. *Direct Fabrication of Mesoporous Carbons Using In-Situ Polymerized Silica Gel Networks as a Template*; Carbon **2003**, *41*, 1525.
86. Gil A., Guiu G., Grange P., Montes M. *Preparation and Characterization of Microporosity and Acidity of Silica-Alumina Pillared Clays*; J. Phys. Chem. **1995**, *99*, 301.
87. Pinnavaia T.J., Tzou M.S., Landau S.D. *New Chromia Pillared Clay Catalysts*; J. Am. Chem. Soc. **1985**, *107*, 4783.
88. Han Y.-S., Matsumoto H., Yamanaka S. *Preparation of New Silica Sol-Based Pillared Clays with High Surface Area and High Thermal Stability*; Chem. Mater. **1997**, *9*, 2013.

89. Choy J.-H., Park J.-H., Yoon J.-B. *Multilayered SiO_2/TiO_2 Nanosol Particles in Two-Dimensional Aluminosilicate Catalyst-Support*; J. Phys. Chem. B **1998**, *102*, 5991.

90. Galarneau A., Barodawalla A., Pinnavaia T.J. *Porous Clay Heterostuctures Formed by Gallery-Templated Synthesis*; Nature **1995**, *374*, 529.

91. Galarneau A., Barodawalla A., Pinnavaia T.J. *Porous Clay Heterostructures (PCH) as Acid Catalysts*; Chem. Commun. **1997**, 1661.

92. Zhu H.Y., Lu G.Q. *Engineering the Structures of Nanoporous Clays with Micelles of Alkyl Polyether Surfactants*; Langmuir **2001**, *17*, 588.

93. Polverejan M., Liu Y., Pinnavaia T.J. *Aluminated Derivatives of Porous Clay Heterostructures (PCH) Assembled from Synthetic Saponite Clay: Properties as Supermicroporous to Small Mesoporous Acid Catalysts*; Chem. Mater. **2002**, *14*, 2283.

94. Beck J.S., Vartuli J.C., Kennedy G.J., Kresge C.T., Roth W.J., Schramm S.E. *Molecular or Supramolecular Templating: Defining the Role of Surfactant Chemistry in the Formation of Microporous and Mesoporous Molecular Sieves*; Chem. Mater. **1994**, *6*, 1816.

95. Monnier A., Schüth F., Huo Q., Kumar D., Margolese D., Maxwell R.S., Stucky G.D., Krishnamurty M., Petroff P., Firouzi A., Janicke M., Chmelka B.F. *Cooperative Formation of Inorganic-Organic Interfaces in the Synthesis of Silicate Mesostructures*; Science **1993**, *261*, 1299.

96. Zhang W., Pauly T.R., Pinnavaia T.J. *Tailoring the Framework and Textural Mesopores of HMS Molecular Sieves through an Electrically Neutral (S^oI^o) Assembly Pathway*; Chem. Mater. **1997**, *9*, 2491.

97. Jagtoyen M., Derbyshire F. *Some Considerations of the Origins of Porosity in Carbons from Chemically Activated Wood*; Carbon **1993**, *31*, 1185.

98. Jamis J., Drljaca A., Spiccia L., Smith T.D. *FTIR Spectroscopic Study of the Adsorption of Hydrogen Cyanide by Metal-Oxide Pillared Clays*; Chem. Mater. **1995**, *7*, 2078.

99. Bandosz T.J., Cheng K. *Changes in Acidity of Fe-Pillared/Delaminated Smectites on Heat Treatment*; J. Colloid Interface Sci. **1997**, *191*, 456.

100. Yu J.-S., Yoon S.B., Chai G.S. *Ordered Uniform Porous Carbon by Carbonization of Sugars*; Carbon **2001**, *39*, 1421.

101. Xing W., Xue J.S., Dahn J.R. *Optimizing Pyrolysis of Sugar Carbons for Use as Anode Materials in Lithium-Ion Batteries*; J. Electrochem. Soc. **1996**, *143*, 3046.

102. Sonobe N., Kyotani T., Tomita A. *Carbonization of Polyfurfuryl Alcohol and Polyvinyl Acetate between the Lamellae of Montmorillonite*; Carbon **1990**, *28*, 483.

103. Barrett E.P., Joyner L.G., Halenda P.H. *The Determination of Pore Volume and Area Distributions in Porous Substances. I. Computations from Nitrogen Isotherms*; J. Am. Chem. Soc. **1951**, *73*, 373.

104. Shriver D., Atkins P. *Inorganic Chemistry (3^{rd} ed.)*; Freeman: New York, NY **1999**.

105. Dardenne K., Schäfer T., Lindqvist-Reis P., Denecke M.A., Plaschke M., Rothe J., Kim J.I. *Low Temperature XAFS Investigation on the Lutetium Binding Changes during the 2-Line Ferrihydrite Alteration Process*; Environ. Sci. Technol. **2002**, *36*, 5092.

106. Cornell R.M., Schwertmann U. *The Iron Oxides: Structure, Properties, Reactions, Occurrence, and Uses*; VCH: Weinheim, **1996**.

107. IUPAC Recommendations *Pure Appl. Chem.* **1994**, *66*, 1739.

108. Oades J.M. *Interaction of Polycations of Aluminum and Iron with Clays*; Clays Clay Miner. **1984**, *32*, 49.

109. Matsuda S., Kamo T., Imahashi J., Nakajima F. *Adsorption and Oxidative Desorption of Hydrogen Sulfide by MoO_3-TiO_2*; Ind. Eng. Chem. Fund. **1982**, *21*, 18.

110. Mishra T., Parida K.M., Rao S.B. *Transition Metal Oxide Pillared Clay: 1. A Comparative Study of Textural and Acidic Properties of Fe(III) Pillared Montmorillonite and Pillared Acid Activated Montmorillonite*; J. Colloid Interface Sci. **1996**, *183*, 176.

111. Bandosz T.J., Jagiello J., Schwarz J. A. *Characterization of the Structure and Surface Acidity of Hydroxychromium Taeniolites*; J. Phys. Chem. **1996**, *100*, 15569.

112. Occelli M.L., Drake B., Gould S.A.C. *Characterization of Pillared Montmorillonites with the Atomic Force Microscope (AFM)*; J. Catal. **1993**, *142*, 337.

113. Pinnavaia T.J. *Intercalated Clay Catalysts*; Science **1983**, *220*, 365.

114. Bandosz T.J. *On the Adsorption/Oxidation of Hydrogen Sulfide on Activated Carbons at Ambient temperatures*; J. Colloid Interface Sci. **2002**, *246*, 1.

115. Bashkova S., Bagreev A., Locke D.C., Bandosz T.J. *Adsorption of SO_2 on Sewage Sludge-Derived Materials*; Envir. Sci. Technol. **2001**, *35*, 3263.

116. *Handbook of Chemistry and Physics (67^{th} ed.)*; CRC Press: Boca Raton, FL **1986**.

117. Finston H.L., Rychtman A.C. *A New View of Current Acid-Base Theories*; Wiley: New York, NY **1982**.

118. Ho T.L. *Hard and Soft Acids and Bases Principle in Organic Chemistry*; Academic Press: New York, NY **1977**.

119. Zhang Z., Dai S., Fan X., Blom D.A., Pennycook S.J., Wei Y. *Controlled Synthesis of CdS Nanoparticles inside Ordered Mesoporous Silica Using Ion-Exchange Reaction*; J. Phys. Chem. B **2001**, *105*, 6755.

120. Bakandritsos A., Simopoulos A., Petridis D. *Carbon Nanotube Growth on a Swellable Clay Matrix*; Chem. Mater. **2005**, *17*, 3468.

121. Salame I.I., Bandosz T.J. *Comparison of the Surface Features of Two Wood-Based Activated Carbons*; Ind. Eng. Chem. Res. **2000**, *39*, 301.

122. Papirer E., Bantzer J., Sheng L., Donnet J.B. *Surface Groups on Nitric Acid Oxidized Carbon Black Samples Determined by Chemical and Thermodesorption Analyses*; Carbon **1991**, *29*, 69.

123. Kyotani T., Kawashima H., Tomita A. *High-temperature Desulfurization with Copper-containing Sorbents*; Envir. Sci. Technol. **1989**, *23*, 218.

124. Bagreev A., Bashkova S., Locke D.C., Bandosz T.J. *Sewage Sludge-Derived Materials as Efficient Adsorbents for Removal of Hydrogen Sulfide*; Environ. Sci. Technol. **2001**, *35*, 1537.

125. Bagreev A., Adib F., Bandosz T.J. *pH of Activated Carbon Surface as an Indication of its Suitability for H_2S Removal from Moist Air Streams*; Carbon **2001**, *39*, 1897.

126. Blesa M.A., Maroto A.J.G., Regazzoni A.E. *Surface Acidity of Metal Oxides Immersed in Water: A Critical Analysis of Thermodynamic Data*; J. Colloid Interface Sci. **1990**, *140*, 287.

127. Hu Z., Williams R.D., Tran D., Spiro T.G., Gorun S.M. *Re-engineering Enzyme-Model Active Sites: Reversible Binding of Dioxygen at Ambient Conditions by a Bioinspired Copper Complex*; J. Am. Chem. Soc. **2000**, *122*, 3556.

128. Morse J.W., Luther III G.W. *Chemical Influences on Trace Metal-Sulfide Interactions in Anoxic Sediments*; Geochimica Cosmochimica Acta **1999**, *63*, 3373.

129. Alder J.F., Fielden P.R., Smith S.J. *The Adsorption of Hydrogen Cyanide by Impregnated Activated Carbon Cloth. Part II: Reactivity of Impregnated Metal Carboxylates towards Hydrogen Cyanide*; Carbon **1988**, *26*, 713.

130. Kobayashi M, Flytzani-Stephanopoulos M. *Reduction and Sulfidation Kinetics of Cerium Oxide and Cu-Modified Cerium Oxide*; Ind. Eng. Chem. Res. **2002**, 41, 3115.